Doctoral Thesis

Meridional distribution of the Earth's plasmasphere derived from extreme ultraviolet images

Go Murakami

Space and Planetary Science Group

Department of Earth & Planetary Science

Graduate School of Science, The University of Tokyo

December 2010

Abstract

The plasmasphere plays a central role in many of the complex processes in Earth's inner magnetosphere. Four decades of studies by a variety of in-situ techniques revealed the dynamical aspect of the plasmasphere changing depending on geomagnetic conditions. However, the in-situ measurements are local observations with which it is difficult to separate the temporal development and the spatial structure of the plasmasphere. Recent advances in satellite-based imaging techniques have overcome this difficulty and made it possible to routinely obtain full global images of the plasmasphere. The Extreme Ultraviolet Imager (EUV) on the IMAGE satellite produced consecutive images of the plasmasphere from the high-latitude view with a time resolution of 10 min and a spatial resolution of 0.1 Re.

The EUV images have revealed the details of a highly structured and dynamic entity of the plasmasphere, and demonstrated that the remote sensing with EUV techniques is a promising means to explore the plasmasphere. On the other hand, their remains some unsolved problems which are difficult to be clarified by the imaging from a limited perspective, i.e. only from the high-latitude view. For example, a radial structure of enhanced brightness called a "finger" was found by the EUV instrument but the cause of this structure is still not understood. Furthermore, the gap between the results of the EUV measurements and the conventional theories for the plasmapause formation has been pointed out. In order to solve these problems, the imaging of the plasmasphere from a different perspective has been emphasized.

We have developed the Telescope of Extreme Ultraviolet (TEX) onboard the lunar orbiter KAGUYA launched in September 2007. Data available from the TEX instrument allow us for the first time to study the plasmasphere from a meridian perspective. The TEX instrument images the He^{+} distribution in the plasmasphere by detecting the resonantly scattered solar 30.4-nm radiation and produces images encompassing the entire plasmasphere. The author has participated intensively in the laboratory and in-orbit calibrations and data evaluation for the onboard instrument.

The performance of the TEX instrument after launch was verified using the in-orbit data obtained from February 2008 to May 2009. The result of this in-orbit calibration is presented in Chapter 2. From March to June 2008, the TEX instrument had produced the first sequential images of the plasmasphere viewed from the meridian perspective. The analysis and evaluation of these first images are demonstrated in Chapter 3. The corotation and the erosion of the plasmasphere were identified in the sequential images during the geomagnetically quiet (Kp < 3) and disturbed period (Kp = 5), respectively. The angular rotation rate for the corotation and the inward velocity of the nightside plasmapause for the erosion are estimated by analyzing these images, and the results are consistent with those derived from IMAGE/EUV observations. This confirms that the TEX instrument successfully detected the spatial distribution and temporal development of the plasmasphere.

Furthermore, a new striking feature of enhanced brightness in the plasmasphere, called as a plasmaspheric “filament”, was found in the TEX image during a prolonged quiet period (Kp < 2). The shape of the filament was closely aligned to the dipole magnetic field line, and this suggests that the filaments are caused by isolated magnetic flux tubes filled with denser plasmas than their neighbors. The nature of the filament agrees with that of the finger structure observed by IMAGE/EUV. Consequently, the result indicates that the finger structure seen in the EUV images should be the equatorial projection of isolated flux tubes filled with denser plasmas than its neighbors.

The formation mechanism of the plasmapause was studied in Chapter 4. The sequential TEX images during the geomagnetic disturbance (Kp = 5) on 1-2 May 2008 were analyzed. The plasmapause positions at the post-midnight observed from the meridian perspective clearly agreed with those predicted by the dynamic simulations based on the interchange mechanism. Furthermore, after the convection enhancement, the He^+ column density in the nightside plasmasphere decreased by ~30% only at the low latitudes (< 20 deg). This suggests that the formation of the new plasmapause occurs first near the equatorial region during a geomagnetically disturbed period. These results agree with the formation mechanism of the plasmapause based on the quasi-interchange instability.

For the next plasmaspheric imaging from the International Space Station (ISS), new multilayer coatings having high reflectivity at 30.4 nm and low reflectivity at 58.4 nm were developed. Chapter 5 deals with this topic. For the He II imaging from ISS, the contamination from geocoronal He I (58.4 nm) emission should be eliminated more effectively than the TEX instrument because ISS orbits at a low altitude of ~350 km, inside the geocorona. The newly developed Y_2O_3/Al multilayer coating designed for normal incidence reflection had higher reflectivity (24.9%) at 30.4 nm and significantly lower reflectivity (1.3%) at 58.4 nm than the conventional coatings such as Mo/Si. The temporal stability of the Y_2O_3/Al multilayer coating was also evaluated and found to be highly stable under vacuum, dry N_2 purge, and normal atmosphere. Then, based on these results, the Y_2O_3/Al multilayer coating was selected to apply for the flight mirror of the Extreme Ultraviole Imager (EUVI) onboard ISS. The calibration of the flight mirror was performed, and it was confirmed that EUVI can produce the plasmaspheric images from ISS with a high SNR of 16.

Contents

Acknowledgements

I wish to express my sincere appreciation to associate Prof. Ichiro Yoshikawa of the University of Tokyo for giving me the wonderful opportunity to enter scientific research. His suggestion and guidance always led me to the right way and bring enthusiasm to me. I deeply keep in mind what I have learned from him during this five-year course.

I am grateful to Dr. Kazuo Yoshioka, Mr. Fukuhiro Ezawa, Mr. Gentaro Ogawa, Mr. Hiromi Watanabe, Mr. Kouichi Sakai, Mr. Tatsuro Homma, and all of the colleagues who are (and were) concerned with Ichiro Yoshikawa's Laboratory in The University of Tokyo for their continuing interest and encouragement. Especially Dr. Kazuo Yoshioka gave me valuable suggestions and supports throughout all of my study. I am proud to be a member of Yoshikawa Laboratory with them.

I would like to thank Dr. Atsushi Yamazaki, Prof. Makoto Taguchi, Dr. Masayuki Kikuchi, Prof. Wataru Miyake, Prof. Shoichi Okano, and all of the members of the UPI team and the SELENE project team for their effort in achieving a successful mission. Thanks are also due to Dr. Yuki Obana and Dr. Masato Kagitani for their helpful advices about the analysis of the TEX data.

I am grateful to associate Prof. Naomoto Iwagami, Professor Masahiro Hoshino, Professor Masafumi Hirahara, associate Prof. Yoshifumi Saito, and Professor Masato Nakamura for providing sincere and constructive comments.

I would like to express my deep appreciation to Dr. Shingo Kameda, Dr. Shoko Ohtsuki, and Dr. Yasuyuki Tanaka for providing useful comments and technical advices.

I wish to thank Mr. Satoshi Ichimaru and Mr. Hisataka Takenaka in NTT Advanced Technology for manufacturing the multilayer coatings and giving me significant suggestions.

I also wish to all the members of Naomoto Iwagami Laboratory and Space and Planetary Science Group at The University of Tokyo for their emotional assistance

and friendship.

The acknowledgements would not be completed without giving thanks to my parents, Kazuhide and Keiko Murakami. They have supported me both financially and mentally during all my life. I am also grateful to my brother and sister-in-law, Naozumi and Chie Murakami, for their encouragement.

Finally, I would like to express my heartfelt thanks to my soon-to-be wife, Hazuki. She has always been with me and been the best partner. This work would not be done without her sincere support and continuous encouragement for these long years.

1 General introduction

1.1 Early observations of the plasmasphere

The magnetosphere is a region around the Earth in which the Earth's magnetic field is the dominant influence and controls the motions of charged particles. Figure 1.1 shows the results of a synthesis of *in-situ* and ground-based observations over 40 years and represents today's generally accepted global view of the Earth's magnetosphere. In the inner magnetosphere, the magnetic field configuration is dipolar like with perturbation at its outer edge caused by the external pressure change of the solar wind. At ionospheric altitude below 1000km in the mid and high latitude, the dipole field is nearly vertical. The charged particles in the ionosphere are free to move upward along magnetic field lines and populate the higher-altitude regions of the Earth's magnetosphere. The charged particles, which are predominantly electrons and protons with energies not exceeding several electron volts [eV], form a region of cold dense plasma (shown in Figure 1.1) and is called the plasmasphere.

The existence of a sharp outer boundary of the plasmasphere, corresponding to the plasmapause, was first discovered in the early 1960s [*Carpenter*, 1963]. Analysis of whistler waves recorded at ground stations established the plasmapause as a permanent feature within the magnetosphere. After the establishment of the definition of the plasmasphere, satellite *in-situ* measurements were used to investigate the inner magnetosphere, particularly the plasmasphere in the 1970s. Figure 1.2 shows the dominance of H^+, He^+, and O^+ measured by a mass spectrometer onboard the OGO 5 satellite, showing density profiles plotted versus the *L*-shell parameter (the distance of the equatorial crossing point of the field line from the Earth's center, measured in Earth's radii). The density profile of He^+ is very similar in shape to that of H^+. The density distribution of those ions sharply decreases by a factor of 100 or more. In Figure 1.2, the position of the outer boundary, the plasmapause, at L=4.9 is evident in both H^+ and He^+. The outer plasmasphere consists of about 90% H^+ and about 10% He^+ with only a trace of O^+.

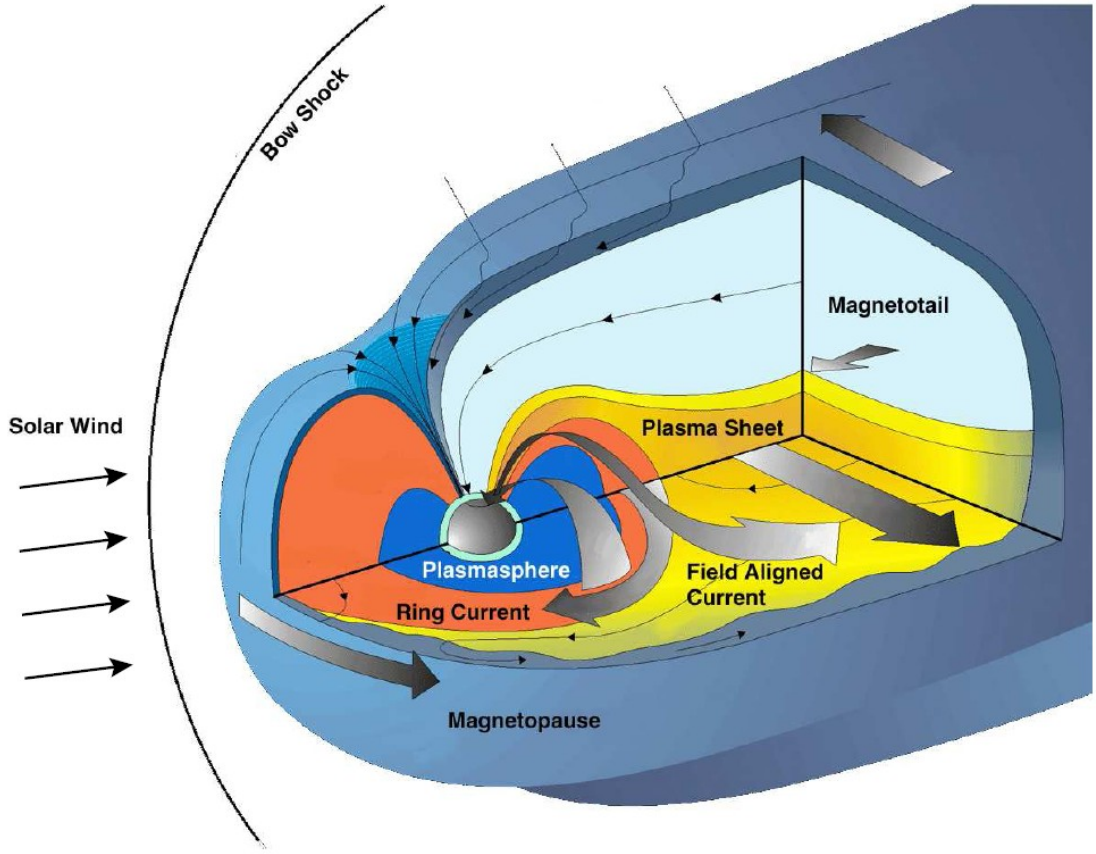

Figure 1.1: A schematic diagram of a generally accepted global representation of the Earth's magnetosphere. This picture has been synthesized from a vast number of localized observations made over the past four decades throughout many of the regions [*Williams et al.*, 1992].

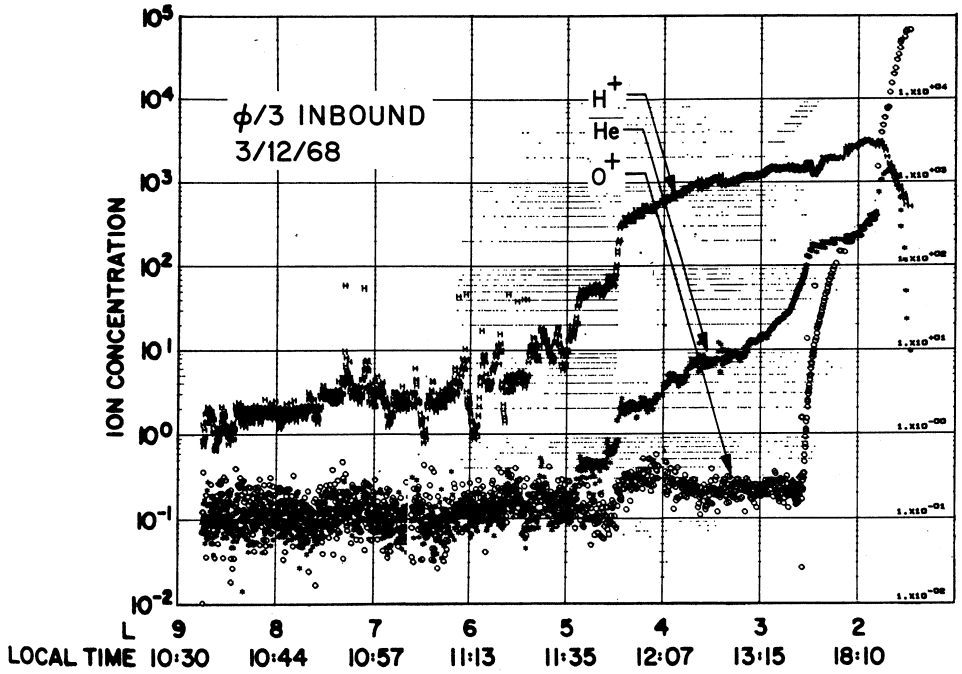

Figure 1.2: A typical inbound plasmapause crossing observed by OGO 5 showing the H^+, He^+, and O^+ ion concentrations as a function of *L* and local time [*Chappell et al.*, 1970].

Intensive observation using spacecraft followed and revealed the dynamical aspect of the plasmasphere changing depending on geomagnetic conditions. It became clear that the plasmapause position is closely correlated with average magnetic activity over a 2 to 6-hour period, e.g., the K_p index [*Chappell*, 1970]. The plasmasphere shrinks with the magnetic activity in a very well-behaved, predictable manner. This variation in the radius of the plasmasphere depending on the magnetic activity is shown in Figure 1.3. This figure represents the superposed results over more than 40 passes of the satellite. The decrease in the radius of the plasmapause is accompanied by an increased steepness in the density gradient at the plasmapause, while the total concentration levels inside and outside the plasmapause remain approximately ~10^3 ions/cm^3 and ~1 ions/cm^3, respectively.

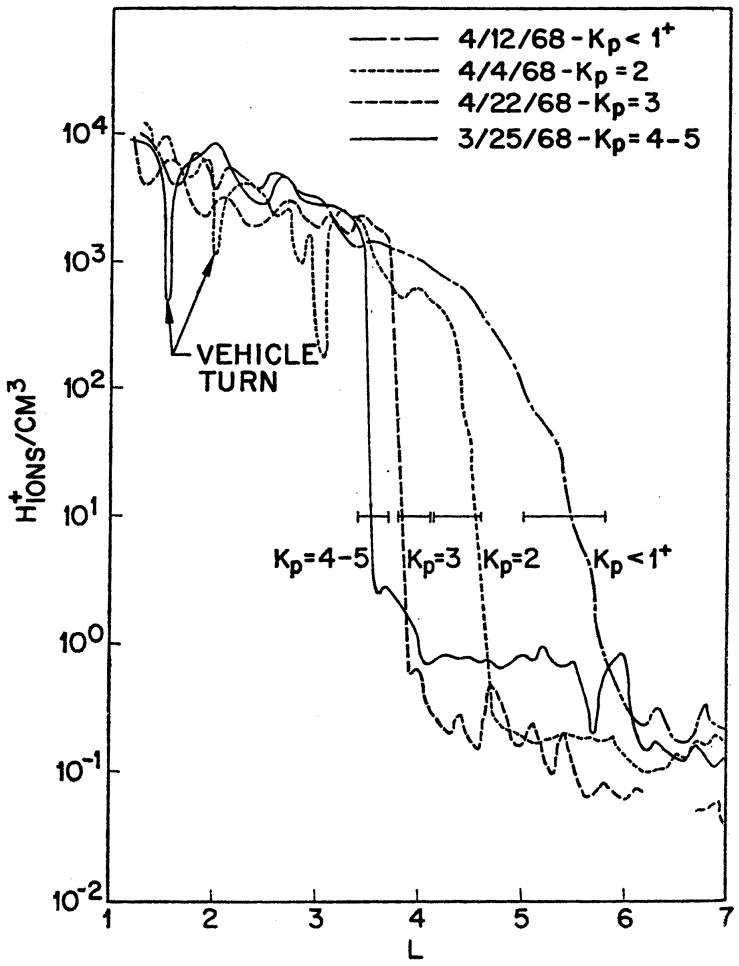

Figure 1.3: A composite graph of H^+ concentration measured by OGO 5 showing the reaction of the plasmasphere in the nightside region to changes in the level of magnetic activity. The plasmapause is found to be steep and move to lower *L* values with increasing activity [*Chappell et al.*, 1970].

Another study on relation of the plasmapause position with the geomagnetic condition was examined. *Carpenter and Anderson* [1992] statistically investigated the location of the plasmapause using the long-term in-situ observations by the Sweep Frequency Receiver (SFR) instrument onboard the ISEE-1 satellite that orbits the Earth on the equatorial plane. Figure 1.4 shows a plot of the plasmapause locations (Lpp: L-value of the plasmapause) versus the value of Kp in the preceding 24 hours. A least squares linear fit to the data is also indicated in Figure 1.4. It represent the relation Lpp

= 5.6 – 0.46Kp_{max}. It was found from ISEE-1/SFR data that this relationship did not change significantly when the data were separated according to night, day and dawn sector values. This indicates that the equatorial plasmapause corotates nearly along a circular trajectory between the midnight sector where it is formed until at least 15 MLT in the afternoon sector.

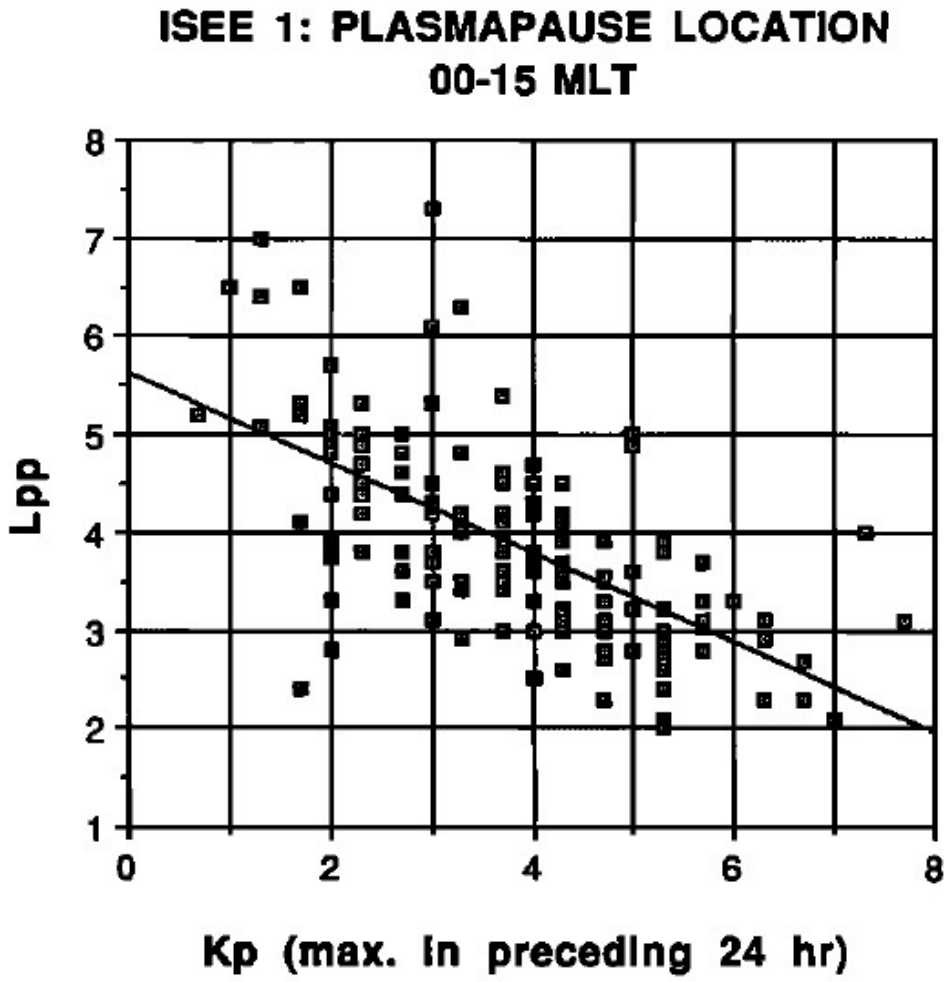

Figure 1.4: Locations of the plasmapause (Lpp) as a function of the maximum Kp value in the preceding 24 hours deduced from the ISEE-1/SFR data during 1977-1983. The profile observed in the local time sector of 00-15 MLT is represented. A least squares linear fit to the data is indicated by the solid line. [*Carpenter and Anderson*, 1992].

Based on the ISEE-1/SFR data, *Carpenter and Anderson* [1992] also investigated the equatorial density distribution in the plasmasphere. Figure 1.5 shows a plot of 11 dayside equatorial density profiles obtained along the near-equatorial ISEE-1 orbits. These profiles tended to be representative of very quiet magnetic conditions. They appear to be well approximated by a linear relation between $\log_{10}N_{eq}$ and L. The least squares linear fit to the profiles shown in Figure 1.5 is given by

$$\log_{10} N_{eq} = -0.3145L + 3.9043 \tag{1.1}$$

where N_{eq} is expressed in electrons/cm^3. This result suggested that even after prolonged periods of quiet, a saturated plasmaspheric flux tube contains fewer particles than it would in the case of isothermal hydrostatic equilibrium [e.g., *Pierrard and Lemaire*, 2001].

Numerous large-scale density irregularities in the plasmasphere were found by the in-situ measurements. One of such irregularities was a deep density trough inside the plasmasphere called as an "inner-trough" or a "donkey-ear" [e.g., *Horwitz et al*., 1990; *Oya*, 1997; *Carpenter et al*., 2000; *Fu et al*., 2010]. Figure 1.6 shows an example of the equatorial density profile with an inner-trough obtained from the ISEE-1/SFR data along an inbound orbit in the dusk sector. The density increased steeply at L ~ 4.2 to plasmasphere levels from values typical of the main plasma trough. Then at L ~ 3.5 a steep outer wall of another trough was encountered. Within this inner-trough the density was a factor of ~5 below nearby plasmaspheric levels. A relative steep interior wall of the trough was detected at L ~ 2.8 as the density returned to plasmaspheric levels. *Carpenter et al.* [2000] conducted a statistical study of inner troughs using the data from the CRESS satellite that encircled the Earth in near-equatorial orbits. The properties of the inner density trough have been described by the occurrence rate (~13% of total passes), L shell range (L < 4 and ΔL = 0.5-1.5), occurrence in MLT (most in the nighttime), duration (up to 10 hours or more), and extent in longitude (at least 20 deg).

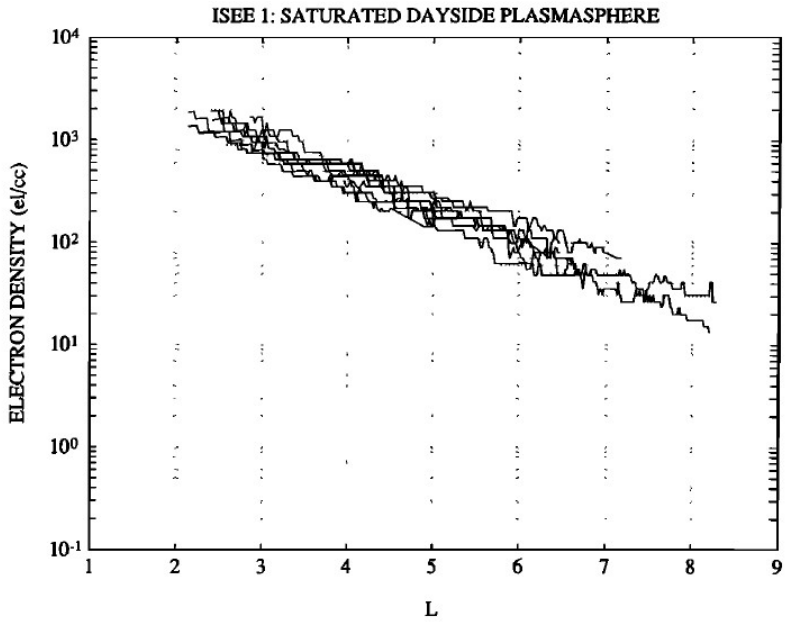

Figure 1.5: Equatorial electron density in the saturated plasmasphere obtained from ISEE-1 observations during the dayside sectors of 09-15 MLT. In each of the 11 cases, the plasmapause was beyond L = 5 (if identifiable). Only the profile interior to the plasmapause are shown [*Carpenter and Anderson*, 1992].

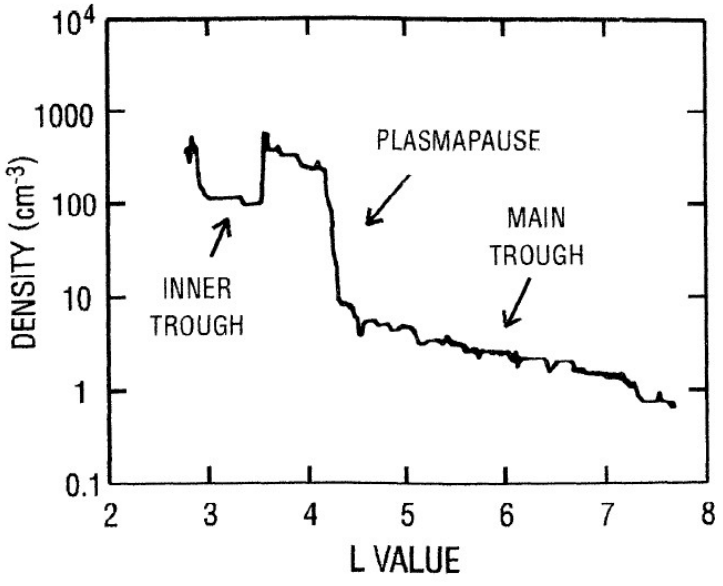

Figure 1.6: A near-equatorial electron density profile observed by ISEE-1/SFR. This profile shows an example of a plasmaspheric cavity in the dusk sector at 17-19 MLT on 17 September 1983 [*Carpenter et al.*, 2000].

The thermal structure of the plasmasphere was also evaluated by the early in-situ observations. The plasma composition experiment on ISEE-1 measured the H^+ temperature [*Comfort*, 1986]. Figure 1.7 shows the mean H^+ temperature as a function of L observed by ISEE-1. Statistical studies revealed that the mean temperature increases with L, both on the dayside and the night side. On the dayside, however, there is a negative temperature gradient for L < 3, an effect that remains unexplained. For L > 4, the temperatures are higher at night.

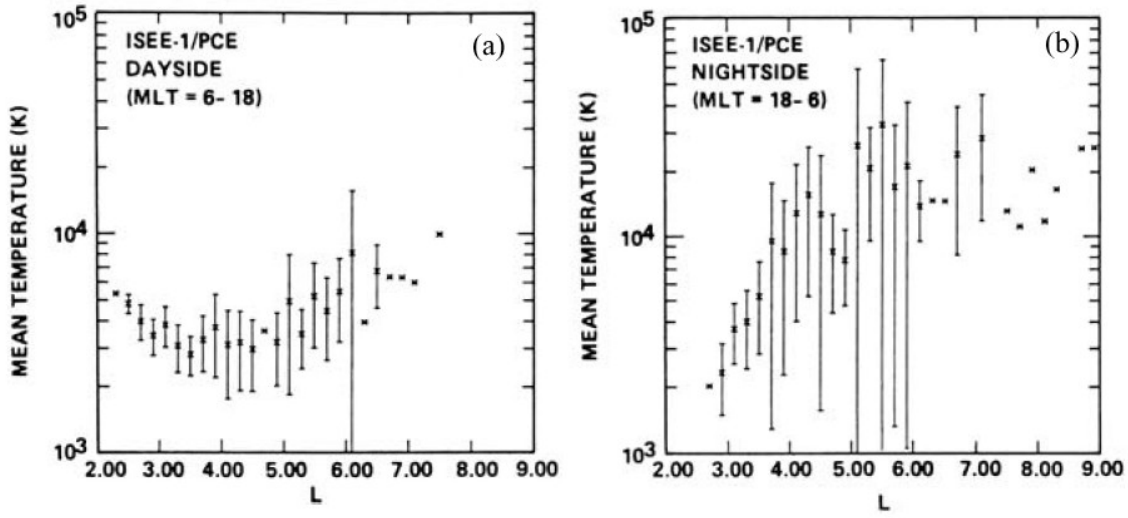

Figure 1.7: Mean H^+ temperature as a function of L for (a) the dayside and (b) the nightside plasmasphere obtained by ISEE-1 [*Comfort*, 1986].

1.2 Theoretical approach for the plasmasphere

On the other hand, there have been theoretical approaches for the comprehension of the plasmasphere [*Nishida*, 1966]. *Nishida* [1966] first represented a clear explanation of the formation of the plasmapause. There is a large-scale electric field directed from dawn to dusk. This electric field originated from the solar wind magnetic field and penetrates into the magnetosphere. The plasma in the magnetosphere drifts to $E \times B$ direction due to this electric field (E is the convection electric field, and B is the Earth's magnetic field). When the corotation with the Earth

is superposed on a large-scale convection, a convection profile shown in Figure 1.8 is obtained. The motions of cold plasmas, such as those in the plasmasphere, are explained by the $E \times B$ drift convection, since their gradient and curvature drifts are very small. In Figure 1.8, it can be seen that the streamlines of the plasma convections can be categorized into two distinctly different flow regimes by a separatrix between open and closed drift paths: those which pass through the magnetosphere, and those which circulate around the Earth. The latter closed region inside the separatrix continues to be filled up to high densities with ionospheric plasmas. Outside this separatrix, cold plasmas on an open drift trajectory generally drift sunward from the tail, and flux tubes are filled up to relatively lower densities of cold plasmas due to their shorter lifetimes in the magnetosphere. As a result, the separatrix can be recognized as the outer boundary of dense plasma, i.e., the plasmapause.

When the geomagnetic activity level increases, the convection electric field increases and the region where corotation is enforced shrinks. The last closed equipotential, as well as the plasmapause, then shifts closer to the Earth. On the contrary, when the convection electric field diminishes, the corotation region expands to include some depleted flux tubes, which can then refill by diffusion from the ionosphere and by other possible mechanisms.

Another mechanism based on quasi-interchange instability has been proposed to explain the plasmapause formation [e.g., *Lemaire*, 1974; 1985; 2001]. *Gold* [1959] first introduced the concept of interchange of the magnetic flux tubes in the magnetospheric context. Its so-called pure interchange model assumes a one to one interchange between magnetic flux tubes enclosing the same magnetic flux and thus leaving the shape of the magnetic field lines unchanged as well as the magnetic energy of the system unperturbed. *Newcomb* [1961] studied the influence of the gravitational field and of stratification on the three modes of the ideal magnetohydrodynamic (the Alfvén mode, the fast and slow modes). He considered a plasma confined in a horizontal magnetic field distribution by a uniform vertical gravitational field. *Newcomb* [1961] identified two convective wave modes whose dispersion relation $\omega = \omega(\mathbf{k})$ is influenced by the stratification of the plasma in the vertical direction, for nearly

perpendicular wave vector. These two modes can be distinguished by their behavior in the limit of zero parallel wave vector: $k_{\parallel} \rightarrow 0$. In this limit the convective wave modes fall into two types and were given the name of quasi-interchange modes. Figure 1.9 shows the schematic diagrams of two quasi-interchange modes. In the limit $k_{\parallel} \rightarrow 0$, the type-1 mode corresponds to Gold's pure interchange mode, while the type-2 mode corresponds to a pure translational mode, i.e., the plasma motion is mainly along the unperturbed magnetic field lines.

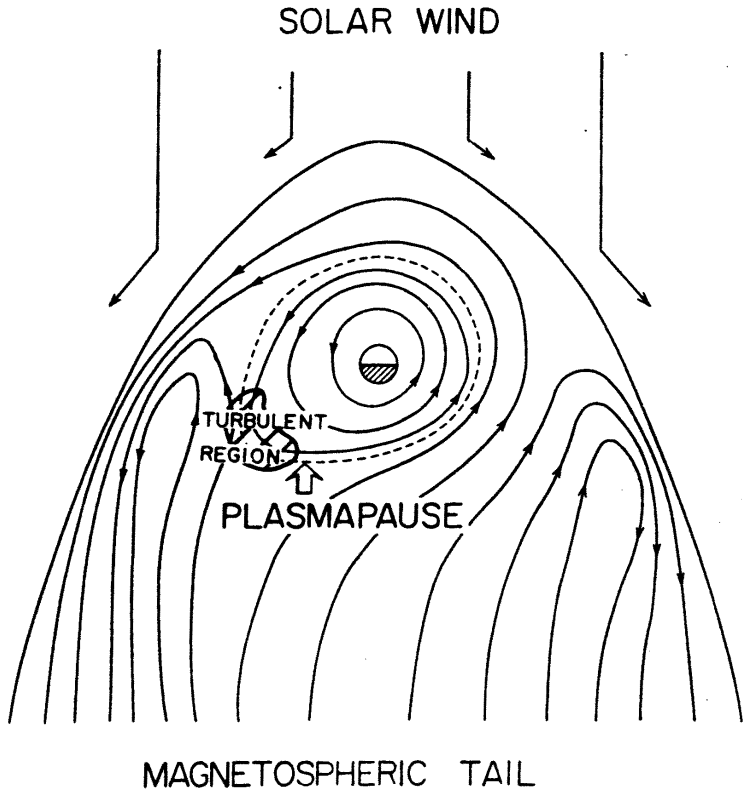

Figure 1.8: Streamlines of the magnetospheric plasma motion obtained by superposing the motion due to the Earth's rotation on the flow of the solar-wind-induced convection. The boundary between two groups of streamlines, i.e., those that pass the tail and those that do not, is suggested to be the plasmapause (dotted curve). The region of turbulence is also indicated [*Nishida*, 1966].

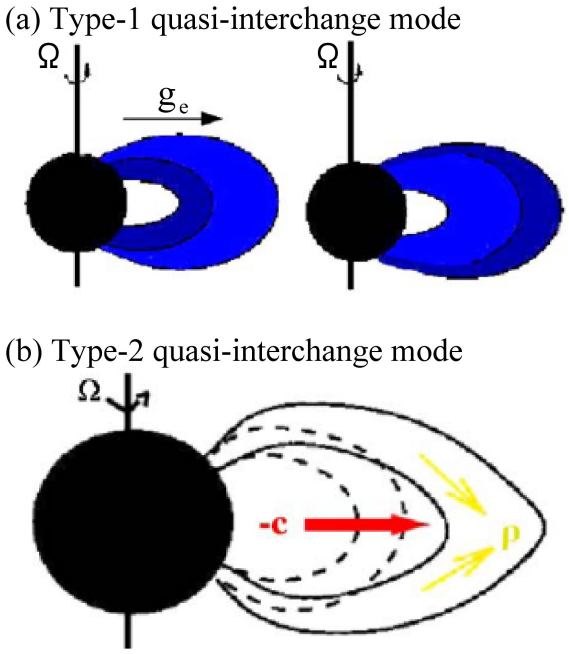

Figure 1.9: Schematic diagrams of the quasi-interchange modes. (a) Type-1 mode: a plasma element with an excess density (dark blue part) exchanges its position with an element of lower density (pale blue part) under the action of the effective gravity $\vec{g}_e$ including the effect of the centrifugal forces due to the planetary rotation Ω. (b) Type-2 mode: an outward displacement (opposed to the direction of the magnetic curvature vector $\vec{c}$) of a flux tube is accompanied by a parallel convergence of plasma along field lines (as indicated by yellow arrows) [from *Andre and Lemaire*, 2006].

Andre and Lemaire [2006] tested the local stability of quasi-interchange modes for various diffusive and exospheric hydrostatic field-aligned density distributions and concluded that the density distribution in the plasmasphere cannot stay in hydrostatic equilibrium. According to this study, the type-2 quasi-interchange mode appears to play an important role than the type-1 mode. As a matter of consequence, unstable field aligned flow tends to be set up in the equatorial region.

The enhanced azimuthal convection velocity leads to increased centrifugal acceleration in the outermost layers of the plasmasphere and a reduction of the total field-aligned potential barrier that ions have to overcome to reach the equatorial plane.

This prompts the uplift of ions out of the underlying ionosphere. As a result of the enhanced outward flow and expansion of the plasma, the field-aligned density is reduced along all geomagnetic field lines traversing the zero-parallel force surface (ZPFS). Along this surface the components of the gravitational and centrifugal acceleration balance each other in the direction parallel to the geomagnetic field lines. As a consequence of the plasma density depletion at high altitude along the field lines traversing the ZPFS, a steep density gradient is formed in the plasmaspheric equatorial density profile. This steep plasma density gradient corresponds to a new plasmapause [*Lemaire*, 2001]. Figure 1.10 shows the schematic diagram of the plasmapause formation based on the quasi-interchange mechanism. In this scenario of the plasmapause formation, the sharp density gradient develops first in the equatorial region, where the transverse cross-L velocity becomes most prominent due to the maximum centrifugal acceleration and curvature of geomagnetic field lines.

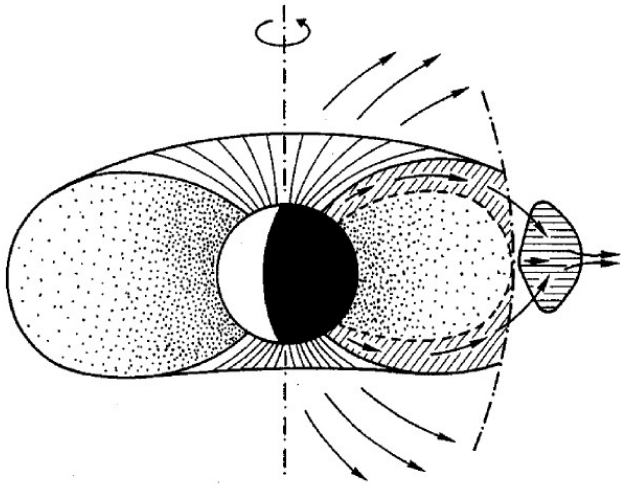

Figure 1.10: A schematic diagram of the plasmapause formation based on the interchange mechanism. Upward ionization flow and detachment of a plasma element from the plasmasphere are occurred as a consequence of enhanced magnetospheric convection. The dashed-dotted line represents the zero-parallel force surface (ZPFS), where the field-aligned components of the gravitational and centrifugal acceleration balance each other [*Lemaire*, 2001].

1.3 Imaging the Plasmasphere

In-situ measurements along the spacecraft's path were intensively performed in the early 1970s, and revealed dynamic aspects of the plasmasphere. However, the *in-situ* measurements are local observations with which it is difficult to separate the temporal development and the spatial structure of the plasmasphere. To overcome this difficulty, various efforts have sought to understand the global distribution of the plasmasphere by visualization.

Helium and oxygen ions are the second and third major components in the plasmasphere, as shown in Figure 1.2, and resonantly scatter the solar extreme ultraviolet (EUV) emission at 30.4 nm (He II) and 83.4 nm (O II), respectively. For this reason, detecting these emissions leads us to the global imaging of the plasmasphere. The fundamental technology to detect the EUV emission began with the He II emission (30.4 nm), which was first detected on a sounding rocket experiment [*Johnson et al.*, 1971]. After this discovery, proof-of-concept observations to give inside-out views of the plasmasphere have been performed by both sounding rockets (e.g. *Ogawa and Tohmatsu*, 1971; *Paresce et al.*, 1974; *Yoshikawa et al.*, 1997) and the spacecraft (e.g. *Weller and Meier*, 1974: *Chakrabarti et al.*, 1982; *Meier et al*., 1998). However, it is difficult to extract the geophysical information on the outer plasmasphere from its inside.

The two-dimensional He II imaging of the Earth's plasmasphere from its outside was first done by the Planet-B (Nozomi) spacecraft [*Nakamura et al.*, 2000]. *Yoshikawa et al.* [2000a, 200b, 2001] first presented static EUV images of the plasmasphere and the inner magnetosphere. Figure 1.11 represents the 2-D image observed by the XUV scanner onboard the Planet-B spacecraft. The image shows the shape of the plasmasphere averaged over the noon-duskside sector. The dipole magnetic field lines of L = 4 and 5 are also shown. While the inner magnetic field line corresponds to the plasmapause, the outer magnetic field line corresponds to the outer boundary of the dusk bulge [*Yoshikawa et al.*, 2000a].

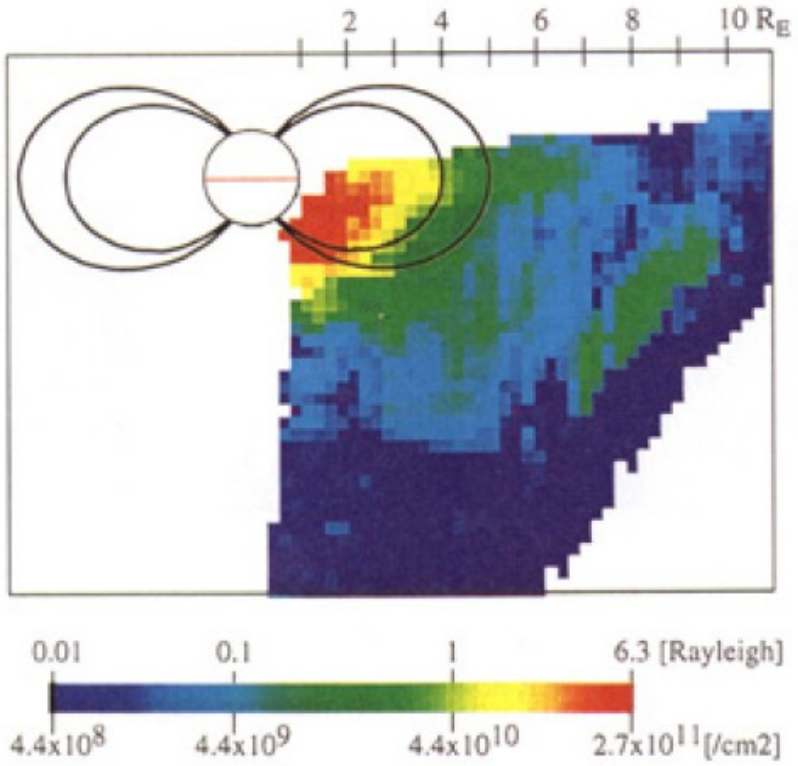

Figure 1.11: Two-dimensional imagery assuming the symmetrical shape of the plasmasphere observed by NOZOMI. The dipole magnetic field lines of L = 4 and 5 are also shown. While the inner magnetic field line corresponds to the plasmapause, the outer magnetic field line corresponds to the outer boundary of the dusk bulge [*Yoshikawa et al.*, 2000a].

Recent advances in satellite-based imaging techniques have made it possible to routinely obtain full global images of the plasmasphere. The Extreme Ultraviolet Imager (EUV) on the Imager for Magnetopause-to-Aurora Global Exploration (IMAGE) satellite gave us complete sequential pictures [*Burch et al.*, 2001a, 2001b; *Sandel et al.*, 2000, 2001]. The EUV instrument detects the distribution of He^+ in the plasmasphere with a time resolution of 10 min and a spatial resolution of 0.1 R_E at the apogee (~8 R_E). The EUV instrument consists of three sensor heads and their fields of view are joined to create a single image.

The EUV images of the plasmasphere reveal a host of distinct features and

behaviors [*Sandel et al.*, 2001, 2003]. The resulting global view provided a new context for more than 40 years of in situ and ground observations. One of the first results led to a refinement in our descriptive language for plasmaspheric structures, which is presented in Figure 1.12. The six EUV image panels provide examples of plumes, notches, shoulders, fingers, channels and crenulations. The direction of the sun is indicated by the yellow dot in each panel. The shadows and aurora are not features of the plasmasphere, but are routinely present in the images. The brightness in these images is proportional to the line integral of the He^+ abundance along each pixel's line of sight. The sharp drop of intensity corresponds to the plasmapause.

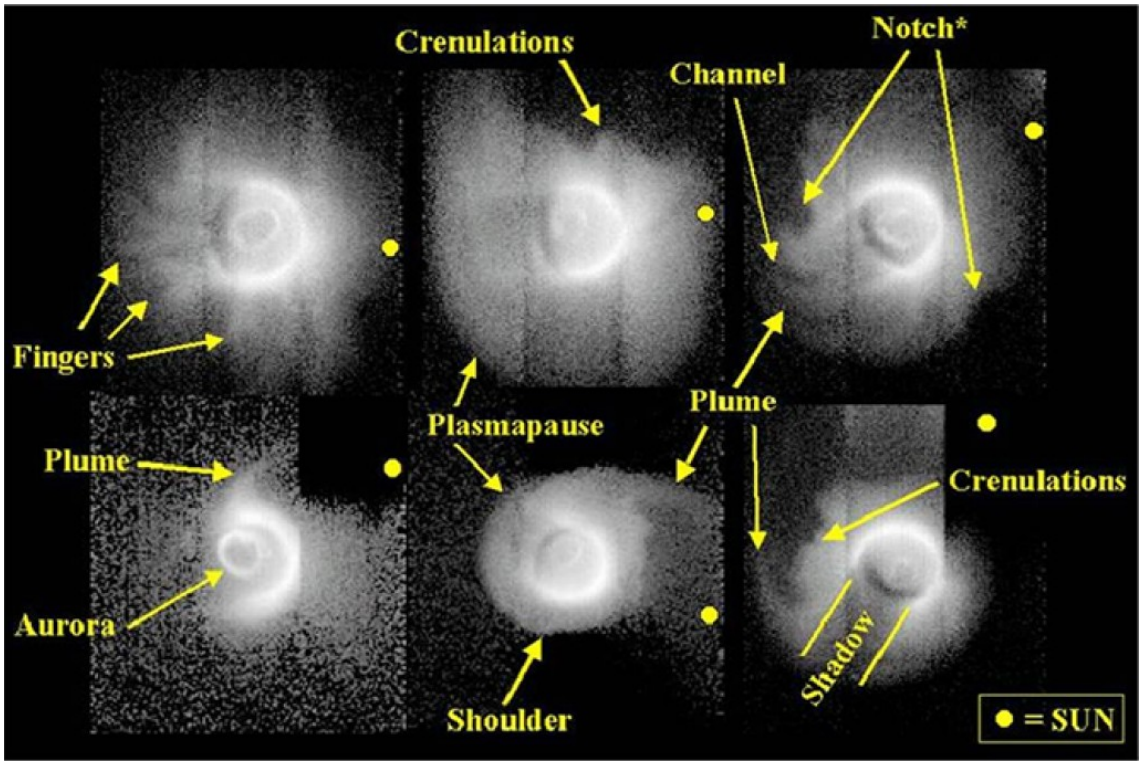

Figure 1.12: Structures observed by the EUV instrument onboard the IMAGE satellite. Various local structures, e.g. shoulders, plumes, fingers, channels, crenulations and notches are identified in the EUV images. The direction to the Sun is shown as a yellow dot for each image. (Adopted from http://image.gsfc.nasa.gov/poetry/discoveries/N47big.jpg)

Global images have also revealed the morphology of the plasmaspheric response to changes in convection, i.e. inward motion of the nightside plasmapause (or erosion) and corotation of the plasmaspheric structure. The typical pattern of erosion and corotation of the plasmaspheric structure (plume) is illustrated using EUV observations in Figure 1.13. The inward motion of the nightside plasmapause (a-d) associated with the enhanced convection and the corotation of a drainage plume (e-i) during the quiet period are identified in the sequential images.

IMAGE observations show that the overall erosion process starts with a formation of the sharp plasmapause near midnight [*Spasojevic et al.* 2003; *Goldstein et al.* 2003a; *Goldstein and Sandel* 2005; *Gallagher and Adrian* 2007]. The onset of the erosion and the plasmapause formation requires only 10-30 minutes after the southward turning of the IMF Bz [*Goldstein et al.* 2003a; *Murakami et al.* 2007]. As for the corotation, the EUV images provide the first evidence that the main body of the plasmasphere does not always corotate with the Earth [*Sandel et al.*, 2003]. The corotation rate of the plasmasphere to the Earth's rotation was studied by tracking the localized density structures, such as notches, plumes, shoulders, and fingers, and was estimated to be about 0.9 [e.g., *Sandel et al.*, 2003; *Burch et al.*, 2004; *Gallagher et al.*, 2005; *Galvan et al.*, 2010].

New global images of the plasmasphere viewed from different perspective have been available. The KAGUYA (SELENE) spacecraft was launched by the H-IIA rocket in September of 2007 and then put into the orbit around the Moon. The Telescope of Extreme Ultraviolet (TEX) mounted in the Upper atmosphere and Plasma Imager (UPI) on KAGUYA detects the resonance scattering emissions of oxygen ions (O II: 83.4 nm) and helium ions (He II: 30.4 nm) to take images of near-Earth plasmas. It is the first time to take the sequential images of the plasmasphere from the meridian perspective, and they provide new aspects of plasmaspheric dynamics. The design, in-orbit performance, and results of the observations are described in Chapters 2, 3, and 4.

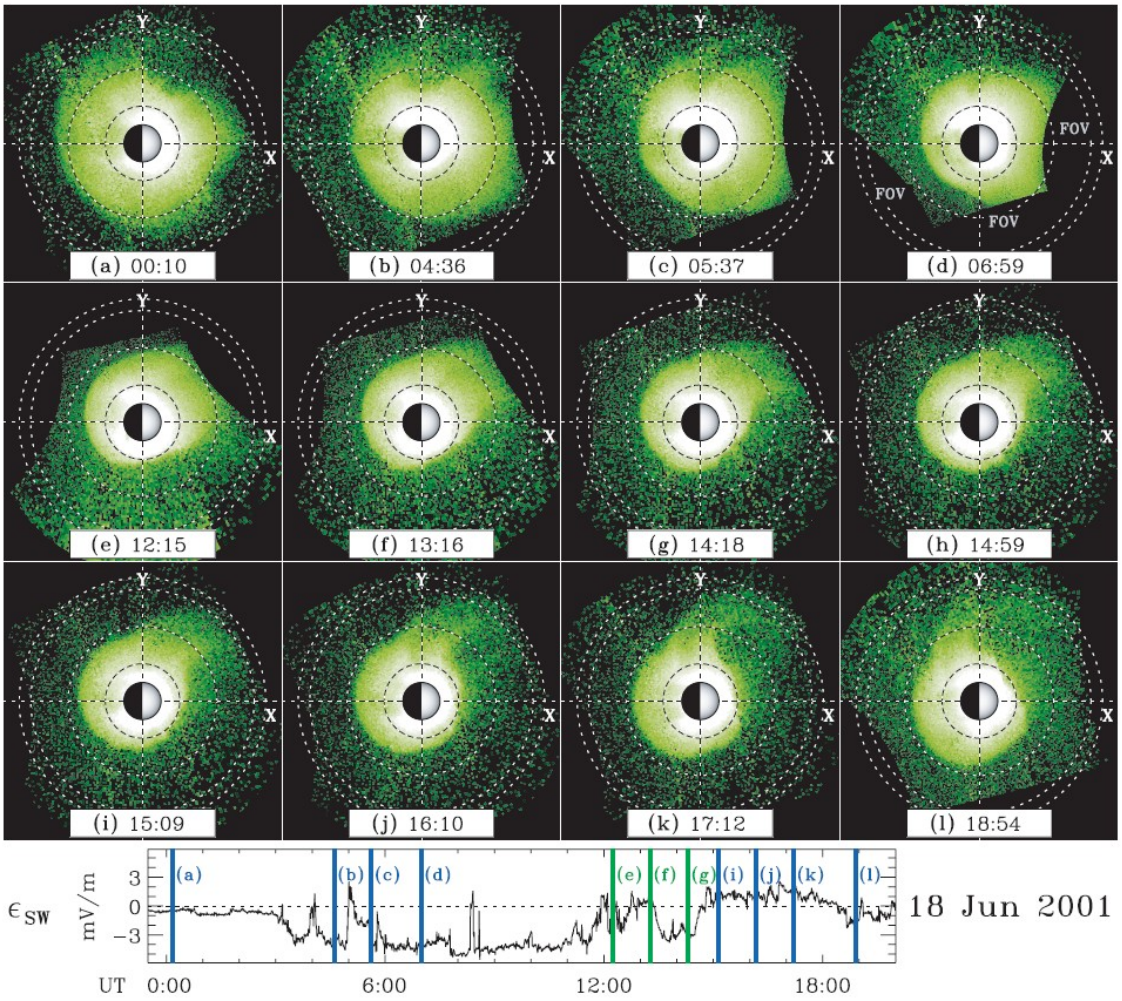

Figure 1.13: (Top panels) Global plasmasphere images observed by IMAGE/EUV on 18 June 2001, mapped to the magnetic equatorial plane (in SM coordinates). The solar direction is to the right and dashed circles are drawn at L = (2, 4, 6, 6.6). Color contour indicates the column abundance of He^+ (in arbitrary units). The inward motion of the nightside plasmapause (a-d) and formation/corotation of a drainage plume (e-i) are identified. (Bottom panel) The solar wind electric field (E_{SW}), defined as product between the solar wind speed and the IMF Bz observed by the ACE satellite. After 03:14 UT E_{SW} was negative, indicating a dawn-to-dusk global electric field. Vertical lines labeled (a) through (l) indicate times of EUV snapshots above. [*Goldstein and Sandel*, 2005]

1.4 Instruments for the plasmasphere imaging

The recent imaging instruments in the EUV region mentioned above have similar types of optics. Figure 1.14 shows schematic cross-sectional drawings of (a) the XUV scanner onboard the Planet-B spacecraft and (b) one of the EUV sensor heads onboard the IMAGE satellite. Each instrument is designed as a normal-incidence telescope. Their optics consists of a multilayer coated mirror to focus EUV photons, a metal thin filter to eliminate unwanted longer wavelength emissions, and microchannel plates to pick up photon events.

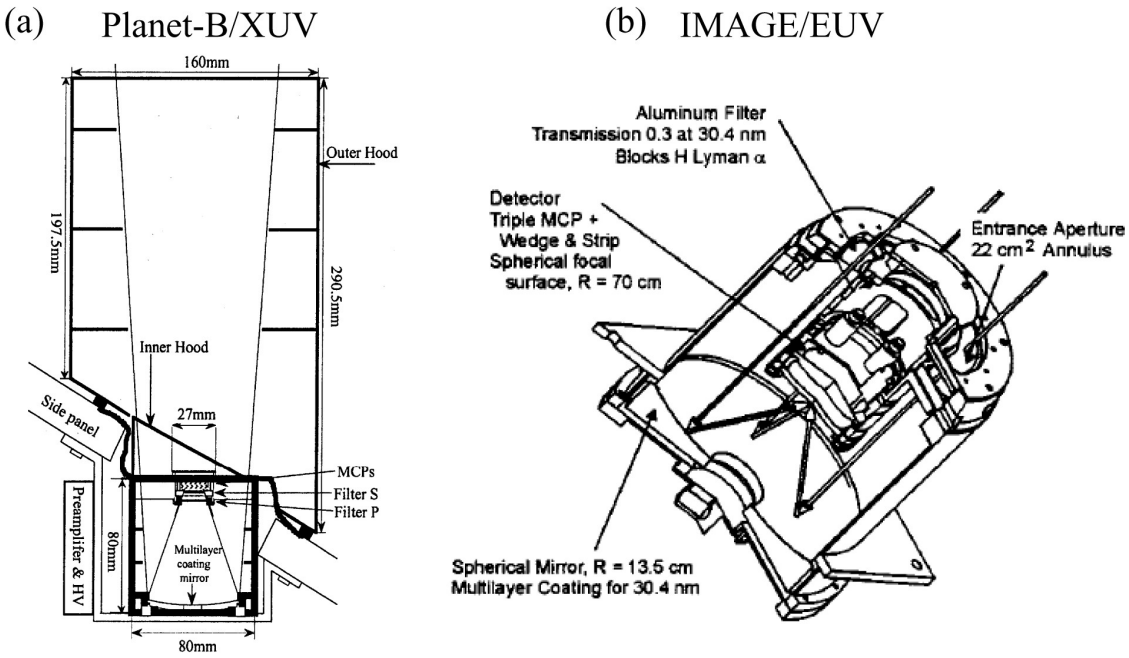

Figure 1.14: (a) A schematic cross-sectional drawing of the XUV scanner onboard the Planet-B (Nozomi) spacecraft [*Nakamura et al.*, 2000]. The optics consists of a multilayer-coated mirror, a thin metal filter, and microchannel plates. (b) A cutaway drawing of the EUV sensor onboard the IMAGE satellite [*Sandel et al.*, 2000].

The majority of effort for developing EUV instrument has been devoted to make high reflective mirrors. It is difficult to build optics to collect EUV photons effectively, because the reflectivities of any materials for normal incidence are quite low in the EUV range (e.g. at most 5% at 30.4 nm). A newly developed multilayer coated mirror provided a technical breakthrough in EUV optics [*Yamashita et al.*, 1992; *Kunieda et al.*, 1996]. This technical achievement have made it possible to build extreme ultraviolet telescopes for the imaging of the plasmasphere. The multilayer coated mirrors having high reflectivity at 30.4 nm have been developed and installed on the instruments mentioned above [*Nakamura et al.*, 2000; *Sandel et al.*, 2000]. Figure 1.15 shows the calculated and measured reflectivities of the Mo/Si multilayer mirror installed in the TEX instrument onboard the KAGUYA spacecraft as a function of wavelength [*Yoshikawa et al.*, 2008]. The high reflectivity of 18.8% for the normal incidence was achieved at 30.4 nm.

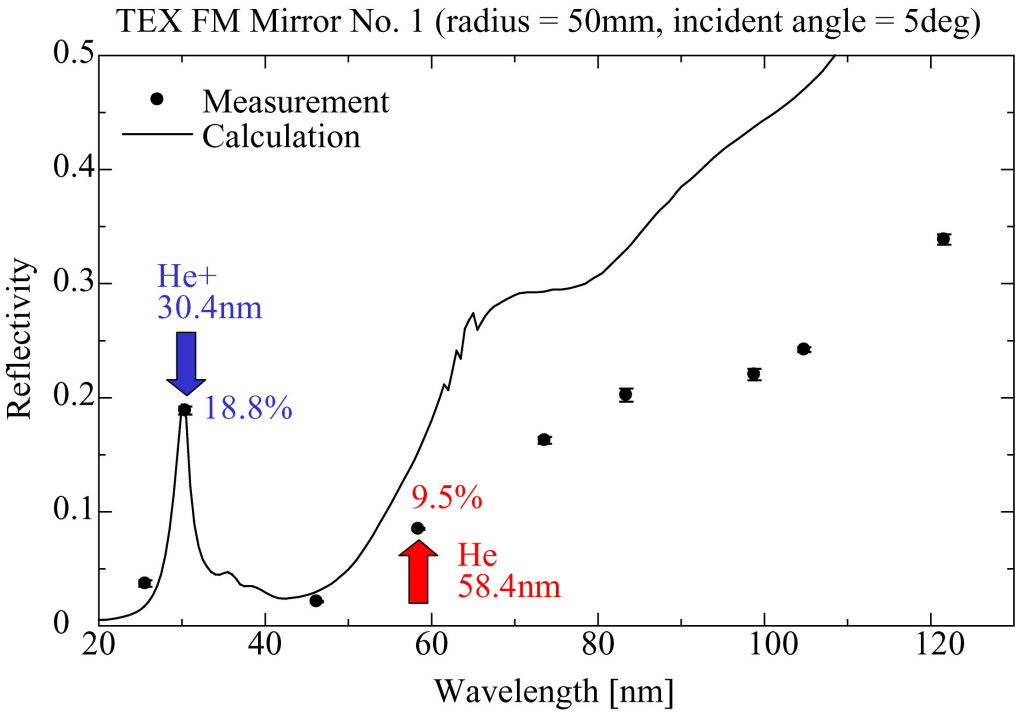

Figure 1.15: Reflectivity of a Mo/Si multilayer coated mirror used in the TEX instrument onboard the KAGUYA spacecraft. The reflectivity of 18.8% is achieved at 30.4 nm (He II).

1.5 Construction of this Thesis

The main purpose of this thesis is to examine the plasmasphere distribution and dynamics from the meridian perspective by means of a global imaging technique in the extreme ultraviolet (EUV) spectral range. This thesis consists of 6 chapters. Chapter 2 presents the in-orbit calibration of the Telescope of Extreme Ultraviolet (TEX) onboard the KAGUYA spacecraft. Chapter 3 details the first meridian images of the plasmasphere obtained by the TEX instrument. It is necessary to emphasize that the TEX instrument observed not only known phenomena such as erosion and corotation but also a new feature of the plasmasphere. In Chapter 4, the plasmapause formation viewed from the meridian perspective by the TEX instrument is discussed. Chapter 5 is devoted to the development of new multilayer mirrors for the next plasmaspheric imaging from the International Space Station (ISS). Concluding remarks are given in Chapter 6.

2 In-orbit calibration of the Telescope of Extreme Ultraviolet onboard KAGUYA

2.1 Introduction

The Japanese lunar orbiter KAGUYA (SELENE) was launched by the H-IIA rocket on 14 September 2007 and put into a polar orbit at an altitude of about 100 km. The KAGUYA project had carried out the scientific observations of the Moon, at the Moon, and from the Moon. A major purpose of this mission was to obtain comprehensive data that can be used to study the origin and evolution of the Moon and moon utilization in the future [*Sasaki et al.*, 2003; *Kato et al.*, 2008]. KAGUYA observed the surface composition, topography, underground structure, magnetic field anomaly, and gravity all over the Moon using remote sensing. Also, in situ measurement of plasma density, electric and magnetic fields, and high-energy particles were performed. Two satellites, OKINA and OUNA, which orbit in elliptic orbits, provided support for communication between KAGUYA and the ground and gravity measurements.

The Upper Atmosphere and Plasma Imager (UPI) onboard KAGUYA is composed of two telescopes (Telescope of Visible Light: TVIS and Telescope of Extreme Ultraviolet: TEX) and an equatorial mounting gimbal that points the telescopes in the desired direction. Unlike the other instruments onboard KAGUYA, UPI looks at the Earth from the lunar orbit in order to visualize the Earth's upper atmosphere and plasmasphere. TVIS takes pictures of the Earth's airglow and aurora at 4 wavelengths [*Taguchi et al*., 2009] and lunar sodium exosphere [*Kagitani et al*., 2009]. TEX images the plasmasphere and polar wind using the resonance scattering emissions of oxygen ion at 83.4 nm (O II) and helium ion at 30.4 nm (He II) [*Yoshikawa et al*., 2008].

After running primary function checks on the instrument, the TEX observation was carried out in mainly two phases. The Earth-tracking phase lasted from March to

June 2008 and provided us first sequential images of the Earth's plasmasphere from the meridian perspective. The analysis of these images and the studies of the plasmasphere are performed in the following chapters (Chapter 3 and 4). The second phase was devoted to the all-sky survey and lasted 6 months from December 2008 to May 2009. During this phase several hundreds of EUV sources were identified by the TEX instrument. The detailed study of such stellar EUV radiations is beyond the scope of this thesis.

In this study, the in-orbit data obtained by the TEX instrument were analyzed to evaluate the instrument performance after launch. The image scale of the field of view (FOV) and the point spread function (PSF) at the detector were calibrated by analyzing the images of bright EUV sources. The long-term variation of the detector performance was also verified.

2.2 Instrument overview

The KAGUYA spacecraft was launched in September 2007, and entered into the lunar polar orbit at an altitude of 100 km. KAGUYA is a three-axial stabilized polar orbiter, with one of the axes of the spacecraft always oriented towards the Moon surface. The TEX instrument is mounted on 2-rotational-axis gimbal system together with TVIS, as show in Figure 2.1. The rotation around the azimuthal (AZ) axis cancels the apparent drift motion of the Earth in the image due to the orbital motion of the spacecraft. The other rotation (EL: elevation axis) cancels the orbital inclination of the Moon. During the Earth-tracking phase, the Earth was always kept in the center of FOV thanks to both rotations. On the other hand, during the all-sky survey the AZ angle was always fixed and the EL angle was moved by ~3 deg everyday. Therefore, the FOV coverage of the sky was a sector strip with an angular width of 8.3 deg during a revolution of the spacecraft, and TEX surveyed an entire great circle on the sky in the period from December 2008 to May 2009.

The TEX instrument is a type of normal-incidence telescope consisting of a multilayer-coated mirror, a split metallic thin filter, and a microchannel plate (MCP)

detector. Figure 2.2 shows a schematic diagram of the TEX instrument, and Table 1 summarizes its main features (including the results of in-orbit calibrations). The detailed design and the ground calibration result [*Yoshikawa et al.*, 2008] of each component are described below.

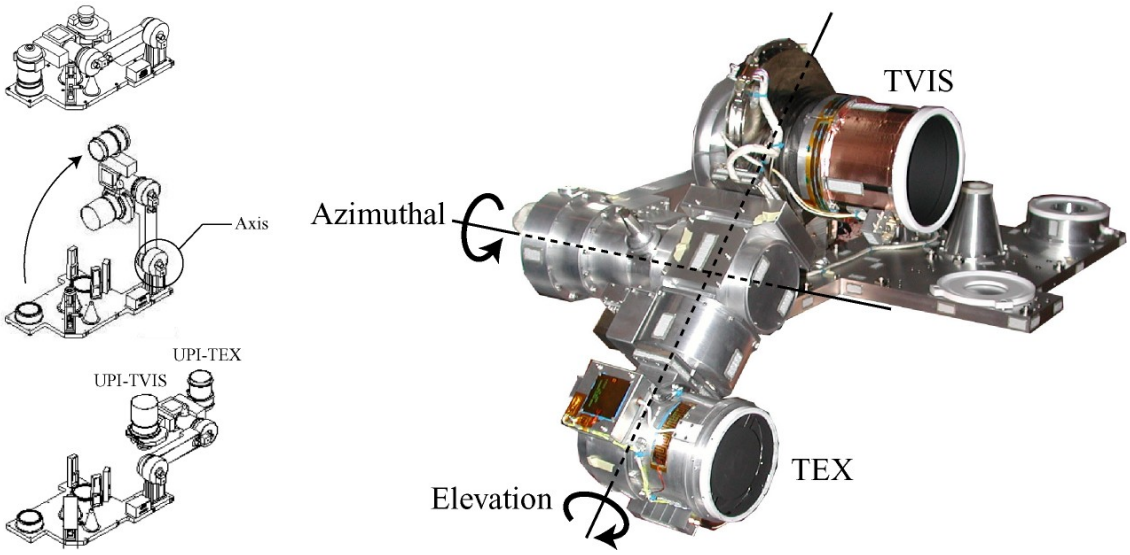

Figure 2.1: Upper atmosphere and Plasma Imager (UPI) onboard the KAGUYA spacecraft. Two telescopes are installed on the equatorial mounting (motor-controlled azimuthal and elevation axes) gimbal. After the insertion to the lunar orbit, the system is open (left panels) in order to make the two telescopes ready to point to the Earth. Pointing accuracy of the equatorial mounting is 3.24" around Azimuthal and 2.68" around Elevation axis.

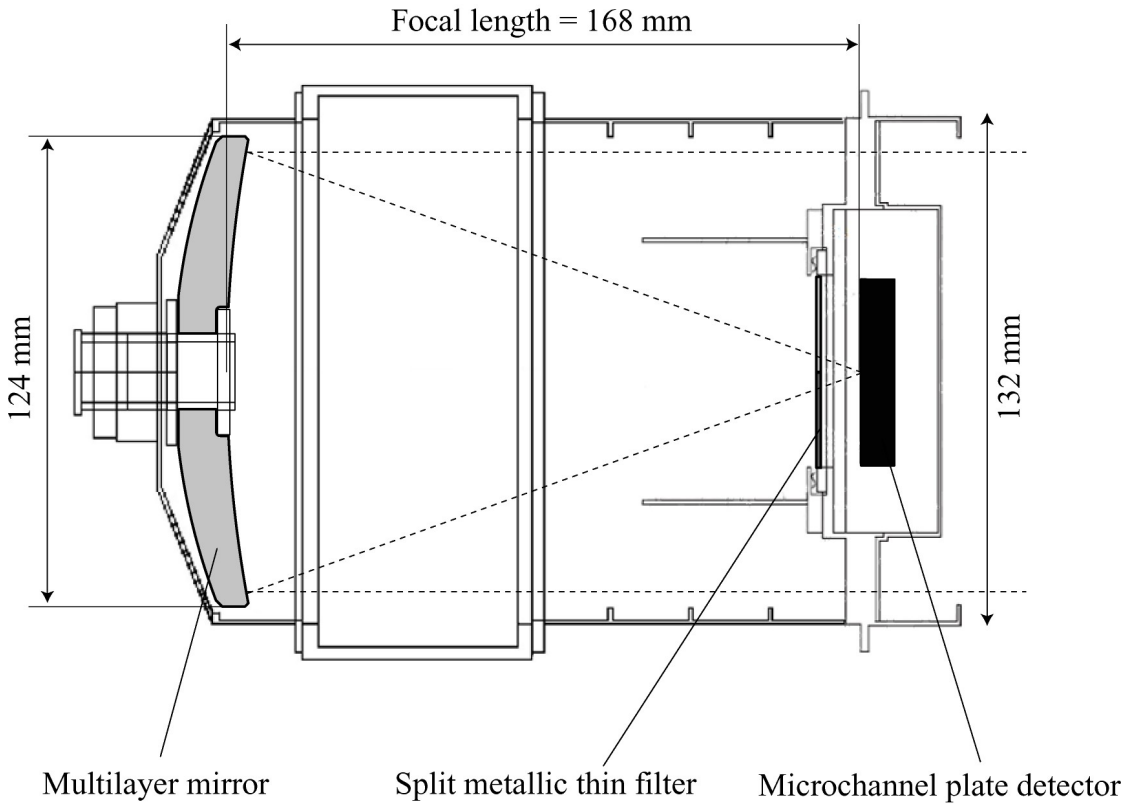

Figure 2.2: A schematic diagram of the Telescope of Extreme Ultraviolet (TEX) instrument onboard the KAGUYA spacecraft. Main optical components are a multilayer mirror, a split metallic thin filter, and a microchannel plate (MCP) detector. The field of view is separated to two regions by the filter; one region is for He II (30.4 nm) radiation and the other is for O II (83.4 nm) radiation.

2.2.1 Multilayer mirror

The multilayer mirror is designed for normal incidence reflection with a peak reflectivity at 30.4 nm, because most materials have much higher single-layer reflectivities at 83.4 nm. For example, the normal incidence reflectance of silicon at 83.4 nm is about 37%. The TEX mirror is coated by 20 alternating Mo/Si layers (period of 16.49 nm, Mo thickness of 4.1 nm, and Si thickness of 12.39 nm). The mirror substrate is made of Zerodur, and the mirror has a focal length of 168 mm, a diameter of 120 mm, and a parabolic shape to reduce aberration. The reflectivities of the flight mirror at 30.4 nm and 83.4 nm are 18.8% and 20.2%, respectively. Although the results

of ground calibrations showed that the Mo/Si multilayer coating was not particularly subject to degradation by oxidation, we protected the coating using normal procedures for handling. We stored the mirror in boxes purged by N_2, and when the mirror had been installed in the telescope, we kept the overall instrument under dry N_2 purge.

2.2.2 Metallic thin filter

The filter material was chosen to provide high transmittance at the target wavelengths of 30.4 nm and 83.4 nm, while attenuating the unwanted Ly-α (121.6 nm) emission from the Earth's geocorona and the interplanetary medium. The filter is set at 12.3 mm off from the focal plane and is divided to two parts. One part has a carbon coating of 31.2 nm on an Al film (162.8 nm), which attenuates emissions whose wavelengths are longer than 40 nm; it allows the passage of He II (30.4 nm) with a small transmittance of He I (58.4 nm). The other part consists of a 292.9-nm thick layer of In and transmits O II (83.4 nm). The filter is supported by a stainless steel mesh having a wire spacing of 0.36 mm and an open area of 75%. The Al material was permitted to oxidize in air on one side, and In was oxidized on both sides. The oxidized coatings stabilize the material and provides the additional benefit of reducing the transmission of Ly-α (121.6 nm).

From the ground calibration, the Al/C part has transmittances of 13.3% at 30.4 nm and 0.27% at 58.4 nm, and the transmittance above 120 nm is below 10^{-9}. The photon rejection at longer wavelengths is good enough to eliminate strong contamination from Earh's Ly-α geocorona. The In filter is used as band-pass filter to prevent He I, He II, and Ly-α emissions from contaminating O II emission. In particular, the Ly-α is so strong that the In filter is designed to be as thick as 292.9 nm despite low transmittance of 2.5% at 83.4 nm. The transmittance at Ly-α is 10^6-fold lower than that at 83.4 nm, and it is sufficient to reduce the contamination of Ly-α.

2.2.3 Microchannel plate (MCP) detector

The microchannel plate (MCP) detector is located at the focus of the telescope mirror. The detector consists of "Z" stack of three MCPs and each MCP has a circular

shape with an active area of 42 mm in diameter, a bias angle of 8 deg, a 12-μm pore size, an L/D (a ratio of length to pore diameter) of 40 and a total resistance of 125 MOhm. Behind the MCPs, the resistive anode encoder (RAE) is placed to analyze the positions of photon injections. The electron cloud emitted from the MCPs consists of an order of ~10^7 electrons. The electron cloud is drifted from the MCP output to the RAE, and its centroid position can be determined. Each photon location is transmitted to an (X, Y) precision of 128 × 128. The dark count of the MCP detector in the ground calibration was ~0.4 cps/cm^2.

2.3 In-orbit performance

The in-orbit data obtained from February 2008 to May 2009 were analyzed to evaluate the performance of the TEX instrument after launch. In this section, the results of the in-orbit calibrations are presented.

2.3.1 Image scale of the field of view (FOV)

The image scale of the TEX instrument was calibrated using the images of some bright stars observed during the all-sky survey. This value is important to convert the dimension of the image from pixel to angle. During the all-sky survey the equatorial mounting gimbal was fixed and the exposure time of each image was 1 min. The FOV of the TEX instrument moved due to the orbital motion of the spacecraft. Therefore the image scale can be estimated comparing the displacement of an EUV star in the image and the rotation angle of the FOV for the exposure time of 1 min. Figure 2.3 shows an example image of a star obtained by the TEX instrument during the all-sky survey. The track of the bright star is detected at the upper left of the image (in the region for O-II radiation). In this case the displacement of the star was 26 pixels and the rotation angle of the FOV was 1.66 deg, which corresponds to the image scale of 0.064 deg/pix. In this way the dependence of the image scale on the position on the detector was investigated. The images of bright EUV stars (> 10 count/min) observed from 25 April to 5 May 2009 (EL angle ranged from 30 to 60 deg) were used. Figure 2.4 represents the result.

The image scales are shown as a function of the distance from the center of the image. It is clear that the image scale is constant and independent of its position. Thus, this result indicates that there are no distortions in the TEX images. In average the image scale was 0.065 ± 0.004 deg/pix, corresponding to 0.068 ± 0.004 Re/pix at the distance of the Earth. The total FOV (128 pix × 128 pix) equals to 8.3 deg × 8.3 deg or 8.7 Re × 8.7 Re.

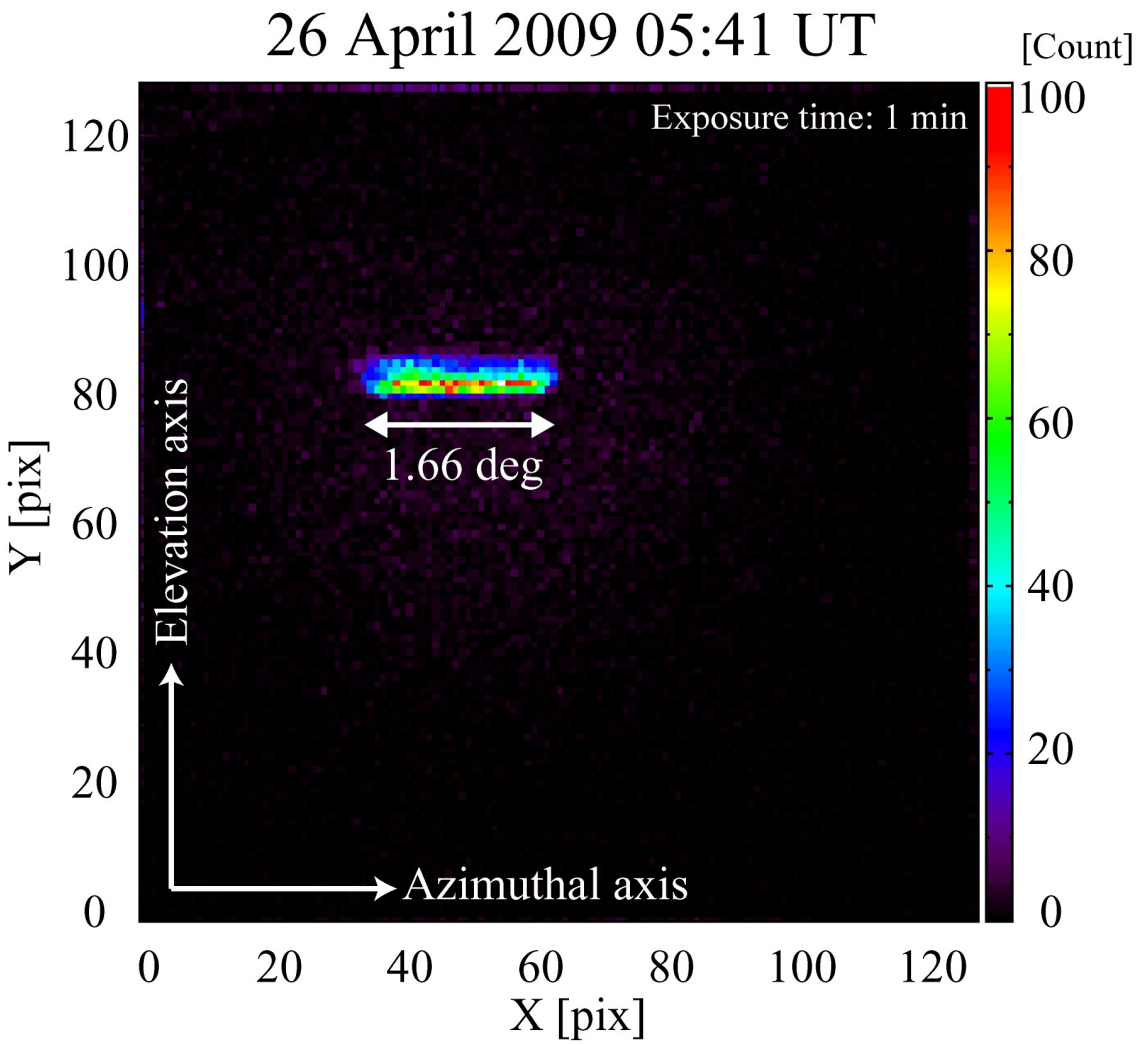

Figure 2.3: An example image of a star obtained by the TEX instrument during the all-sky survey. During this observation phase the equatorial mounting gimbal was fixed, so the FOV of the TEX instrument moved due to the orbital motion of the spacecraft. In this case the movement of the FOV for 1 min was 1.66 deg, which corresponds to 26 pixels in the TEX image.

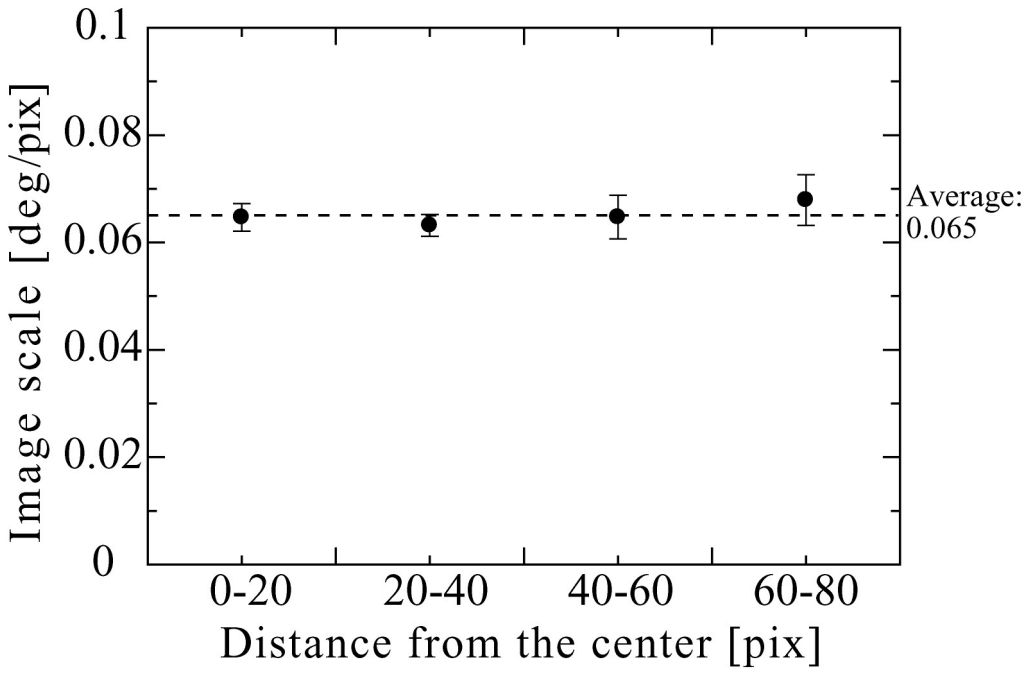

Figure 2.4: Dependence of the image scale on the position at the detector. The dot shows the average of the image scale at each distance from the center of the detector.

2.3.2 Point-spread function (PSF)

To verify the spatial resolution of the TEX instrument from in-orbit data, images of some bright stars were analyzed individually. The spatial resolution of the telescope can be estimated by the width of the point-spread function (PSF). During the Earth-tracking phase, some bright stars were detected in the FOV (mostly in the region for O II radiation). Figure 2.5 shows an example image of a bright star obtained by the TEX instrument. The white circle represents the Earth, and the white square encircles the star. The star is brighter than the dayside of the Earth by a factor of ~3. A two-dimensional Gaussian fitting was used to estimate the width of the PSF. In this case shown in Figure 2.5 the full-width at half-maximum (FWHM) of the PSF is 1.8 pix. In this way, the images of bright EUV stars observed from March to June 2008 were analyzed. As a result, the average FWHM of all PSFs was 3.7 ± 1.1 pix, corresponding

to 0.24 ± 0.07 Re. Based on this result, the 2 × 2 pixel binning should be used in the analysis of the plasmaspheric images, described in Section 3 and 4, to improve the signal-to-noise ratio (SNR).

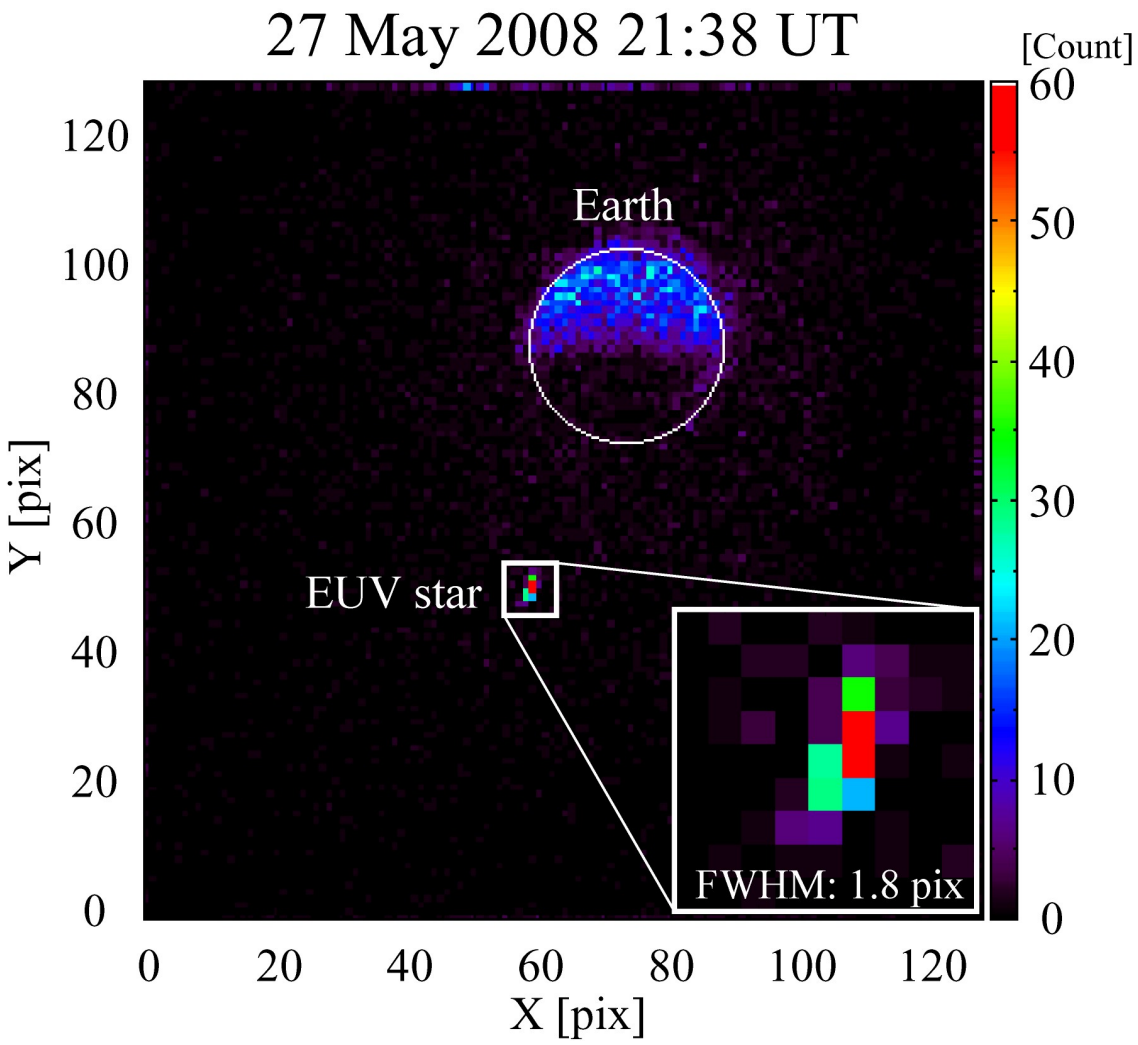

Figure 2.5: An example image of a star obtained by the TEX instrument. In this period the TEX instrument was pointed to the Earth using the equatorial mounting gimabl. The Earth is indicated by the white circle. A bright star is seen near the center of the image as indicated by the white square. In this image the FWHM of the point-spread function (PSF) is 1.8 pix.

2.3.3 Background

The temporal variation of the background in the region for He II radiation throughout the KAGUYA mission was investigated. Figure 2.6 shows the background counts as a function of time since the MCP detector initially turned on. The backgrounds were estimated using the images of the interplanetary space without any bright objects (the Earth or stars) in the FOV. The average value of the background throughout the mission was 1.8 cps/cm^2. This value is larger than the MCP dark counts of ~0.4 cps/cm^2 measured in the laboratory. The background is caused by dark counts from MCPs in the detector, bombardments of cosmic rays and/or high energy particles, and emissions from the interplanetary space. For the lunar environment, this increase was mainly due to the contamination from He I (58.4 nm) emission from the interplanetary space. *Yamazaki et al*. [2006] reported that the intensity of He I emission from the interplanetary space observed by the Extreme Ultraviolet (XUV) scanner onboard the Planet-B spacecraft is 1.5-7.5 Rayleigh. Using this value and the sensitivity of the TEX instrument (2.0×10^{-4} cps/Rayleigh/pix), the background caused by the He I emission from the interplanetary space can be estimated to 0.8-4.2 cps/cm^2. The result shown in Figure 2.6 is consistent with this value. Nevertheless, the backgrounds were constantly low (1.8 cps/cm^2) compared to typical signal levels from the plasmasphere (~30 cps/cm^2) and there were no significant changes. This result suggests that the MCP detector had worked throughout the mission without any problems, e.g., some hot spots on the MCPs.

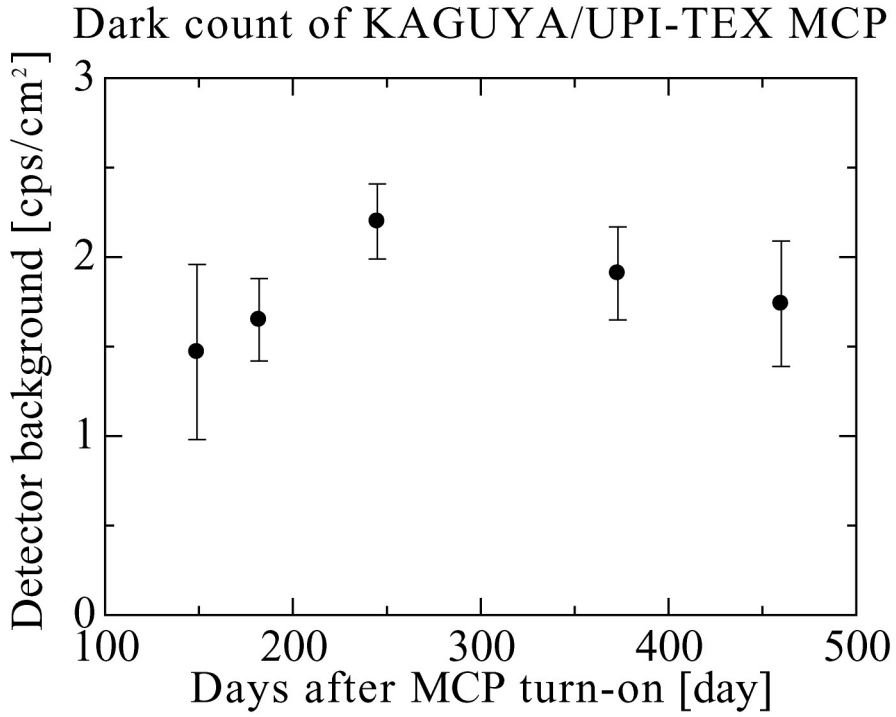

Figure 2.6: The backgrounds as a function of time since the MCPs were first turned on. All the backgrounds were obtained while the TEX instrument was directed to the interplanetary space, so the backgrounds due to the cosmic rays, the high-energy particles, and the emissions from the interplanetary space. The intrinsic detector background measured in the laboratory was below 0.5 cps/cm^2 [Yoshikawa et al., 2007]. The backgrounds are constantly low (~1.8 cps/cm^2) compared to typical signal levels from the plasmasphere (~30 cps/cm^2) and there are no prominent changes.

The signal-to-noise ratio (SNR) during the plasmaspheric observation can be estimated using the background obtained above. The detector behaves as an ideal photon counter so that signal corresponds to the number of photon events collected during an exposure period. During the measurement, a detector pixel sees the EUV signal (N_{signal}), measured in cps/bin, and the background ($N_{\mathrm{background}}$: instrumental background plus contaminations from the other EUV emissions), measured in the same units. The SNR is calculated as follows:

$$N_{\text{signal}} = N_{\text{total}} - N_{\text{background}}$$

$$\sigma_{\text{signal}} = \sqrt{\sigma_{\text{total}}^2 + \sigma_{\text{background}}^2} \approx \sqrt{\sigma_{\text{signal}}^2 + 2\sigma_{\text{background}}^2}$$

$$\approx \sqrt{N_{\text{signal}} + 2N_{\text{background}}} \qquad (2.1)$$

$$SNR = \frac{N_{\text{signal}}}{\sigma_{\text{signal}}} = \frac{N_{\text{signal}}}{\sqrt{N_{\text{signal}} + 2N_{\text{background}}}}.$$

The sensitivity of the TEX instrument for He II (30.4 nm) radiation is 0.016 cps/Rayleigh/pix, and the typical intensity of the plasmasphere at 30.4 nm is ~1 Rayleigh. Assuming the 2 × 2 pixel binning and the exposure time of 20 min, SNR = 9 is achieved.

2.3.4 Pulse height distribution of the MCPs

The aging change of the MCP performance through the mission was verified from the in-orbit data. An important indicator of the MCP stack performance is the statistical variation of the gain; i.e. the pulse height distribution (PHD) of the single photon events. It is well known that all MCPs experience gain decreases as a function of use, a phenomenon caused by electron scrubbing of useful mobile secondary emitting materials out of the channels [e.g., *Joseph et al.*, 1998]. The gain appears to be an exponentially decreasing function of the total amount of charge extracted from the MCP. To verify the aging change of the MCP gain throughout the mission, the PHDs of the MCPs obtained at the beginning (on 14 February 2008) and the end (on 29 March 2009) of the TEX observation were compared, as shown in Figure 2.7. The observation targets on (a) 14 February 2008 and (b) 29 March 2009 were the Earth and a bright EUV star, respectively. In both cases the same input voltages of –1943 V were applied to the MCP stack. Comparing Figure 2.7a and b there are no clear changes of the gains at the peaks in the PHDs. This result indicates that the MCP stack installed in the TEX instrument kept its gain performance throughout the mission.

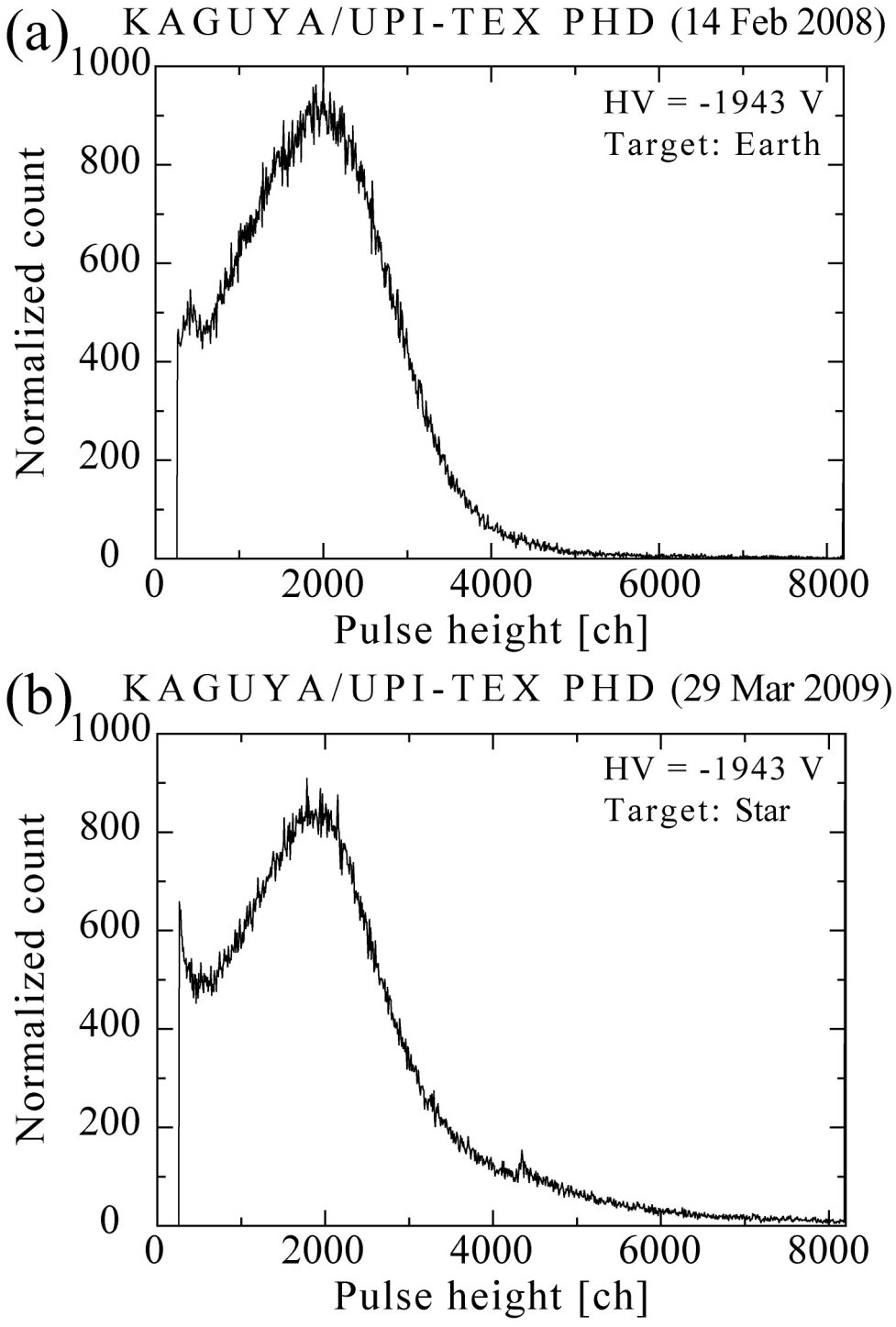

Figure 2.7: Pulse height distributions (PHDs) of the microchannel plates (MCPs) obtained (a) on 14 February and (b) on 29 March 2009. In both cases the same input voltages of –1943 V were applied to the MCPs. Comparing (a) and (b), there are no clear changes in the PHDs.

Table 2.1: Principal TEX parameters

Prime focus	F/1.4	
Angular resolution (1 pix)	0.065 deg	
Spatial resolution (1 pix)	0.068 R_E	
Maximum time resoution	1 min	
Mass	2 kg	
Size	235 mm×φ140 mm	
Open Aperture	48.6 cm^2	
Format	128×128	
FOV	8.3 × 8.3 deg^2	
	Typ. (at 30.4 nm)	Typ. (at 83.4 nm)
Reflectivity of mirror	18.8%	20.2%
Transmittance of filter	11.2%	2.1%
Quantum efficiency of MCP	7.6%	9.8%
Sensitivity	0.016 cps/Rayleigh/bin	0.0036 cps/Rayleigh/bin

2.4 Summary

The performance of the TEX instrument after launch was evaluated using the in-orbit data obtained from February 2008 to May 2009. The image scale of the field of view (FOV) was calibrated by analyzing the images of bright EUV sources observed during the all-sky survey, and the result of 0.065 deg/pix corresponding to 0.068 Re/pix was obtained. The point-spread function (PSF) at the detector was also calibrated using the images of bright EUV sources during the Earth-tracking phase. The average FWHM of PSF was 3.7 ± 1.1 pix, corresponding to 0.24 ± 0.07 Re. This result suggests that the 2 × 2 pixel binning should be used in the analysis of the plasmaspheric images to improve the signal-to-noise ratio (SNR). Furthermore, the long-term variation of the detector performance was also verified. The background throughout the mission was almost constant, in average 1.8 cps/cm^2. This value is enough low and the signal-to-noise ratio (SNR) of 9 can be achieved in the plasmaspheric imaging. No aging degradation was identified in the gain performance of the MCP detector throughout the mission. These results are important not only for the scientific products but also for the future instruments.

3 First sequential images of the plasmasphere from the meridian perspective by KAGUYA

3.1 Introduction

Recent advances in satellite-based imaging techniques have made it possible to routinely obtain full global images of the plasmasphere. The Extreme Ultraviolet Imager (EUV) onboard the IMAGE satellite [*Sandel et al.*, 2000], which detects He II emission, produced consecutive images of the terrestrial plasmasphere from the aerial view [*Sandel et al.*, 2001; *Burch et al.*, 2001]. The IMAGE mission provided new evidence of the dynamic and spatially-structured nature of the plasmasphere. For example, IMAGE/EUV observations show that the nightside plasmapause moves inward in quick (10-30 min) response to the southward turning of the IMF Bz [*Goldstein et al.*, 2003b; *Murakami et al.*, 2007]. The EUV images also provide the first evidence that the main body of the plasmasphere does not always corotate with the Earth [*Sandel et al.*, 2003].

The IMAGE mission identified not only conventional pictures of the plasmasphere (plasmapause, tails, and duskside bulge), but also novel structures (e.g., depleted regions that are called "voids" and a sharp azimuthal gradient in He^+ density called “shoulder”). One of the most striking and puzzling features seen in the EUV images is a radial structure of enhanced brightness called a “finger” [*Sandel et al.*, 2001]. *Sandel et al.* [2001] interpreted these structures as isolated flux tubes that have been filled to higher densities than neighboring tubes. Such flux tubes viewed from a position at high magnetic latitude would appear projected into the magnetic equator plane, leading to the observed finger-like appearance. If this interpretation is correct, investigation of fingers can play a key role to solve the longstanding issues of

plasmasphere refilling. On the other hand, *Adrian et al.* [2004] explained fingers as radial He^+ enhancements arising from some resonance of ultra-low frequency waves. It is very important to know the cause of the finger structures for plasmasphere dynamics. Although the EUV imager observed fingers many times, they have not been completely understood due to the limited perspective of the EUV imager, i.e. only from high magnetic latitude.

Now global images of the plasmasphere from another perspective become available. The Telescope of Extreme Ultraviolet (TEX) onboard the Japan's lunar orbiter KAGUYA images the resonance scattering emissions of oxygen ion at 83.4 nm (O II) and helium ion at 30.4 nm (He II) [*Yoshikawa et al.*, 2007]. The view afforded by the KAGUYA orbit encompasses the plasma distribution in a single exposure, enabling us to examine for the first time the globally-averaged properties of the plasmasphere from the "side" (meridian) perspective. In this study, the first meridional images of the plasmasphere obtained by the TEX instrument onboard the KAGUYA spacecraft were analyzed and discussed.

3.2 Instrumentation and observation

The KAGUYA spacecraft was launched in September 2007, and entered into the lunar polar orbit at an altitude of 100 km. The TEX instrument is mounted on 2-axis gimbal system. Thanks to the gimbal rotations, the Earth can always be kept in the center of FOV, providing images of the Earth's plasmasphere every minute. The TEX instrument detects the resonance scattering emissions of helium ions (He II) and oxygen ions (O II). In this study, only data of He II radiation are used.

The KAGUYA satellite orbits around the Moon with an orbital period of 2 hours. This provides an observation window of the Earth every 2 hours, though observation must satisfy some geometrical conditions. Figure 3.1 shows schematic geometry among the Earth, the Moon, and the satellite. We can turn on the instrument in the following conditions. (1) The satellite has a clear view of the Earth. (2) The satellite is in the umbra of the Moon, thus reducing stray sunlight incident on the TEX instrument. (3) The umbra period is longer than 15 min.

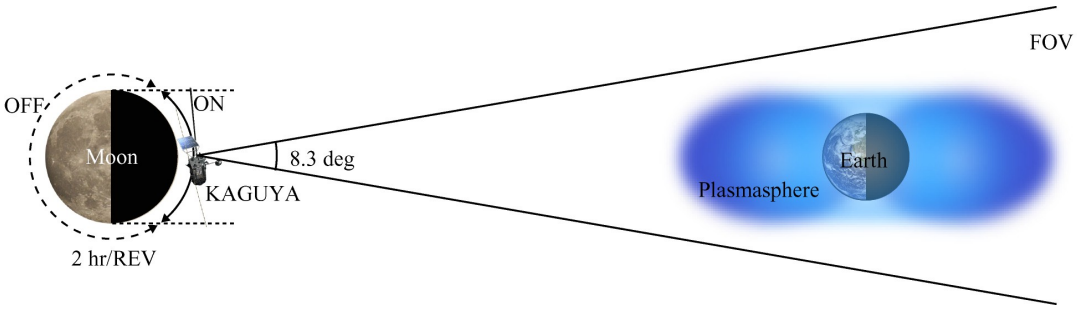

Figure 3.1: Schematic diagram of the geometry among the Earth, the Moon, and the KAGUYA spacecraft. TEX starts to observe in the condition that (1) KAGUYA is in sight from the Earth, (2) KAGUYA is in umbra of the Moon, (3) the umbra period is longer than 15 min.

After the primary function checks of the complete spacecraft and instrument, the observation of the plasmasphere in the Earth-tracking mode was started in March 2008. Unfortunately, the metal band-pass filer was found to be mechanically damaged. This might have been due to the vibration or shock during the vehicle launch phase. Two small pinholes on the filter were identified. The exact locations of these pinholes were investigated, and two circular "ghosts" appeared on all EUV images due to the leak of geocoronal emissions from longer wavelength. The ghost locations are stable in all EUV images and predictable by calculation, independent of plasmaspheric morphology. This fact simplifies the image correction and image analysis, and ensures our study without additional care. In this study, all pixels which were potentially contaminated by the artificial signals have been removed.

Figure 3.2 shows a schematic drawing of geomagnetic field lines from the perspective view of KAGUYA. We should note that a 2-dimensional view of the plasmasphere is not dipole-like, but the outer boundary is elliptic, because the brightness reflects the column density along the line-of-sight (LOS) of the measurement. For example, during the observation in June 2008 reported in the following section, our telescope gazed down to the Earth's geomagnetic equatorial

plane by 20 degree. As described in Chapter 2, the TEX instrument has a field-of-view (FOV) of 8.3 deg × 8.3 deg, which corresponds to 8.7 Re × 8.7 Re at the Earth's position. The format of the image is 128 × 128 pixels (i.e., 1 pix = 0.068 Re).

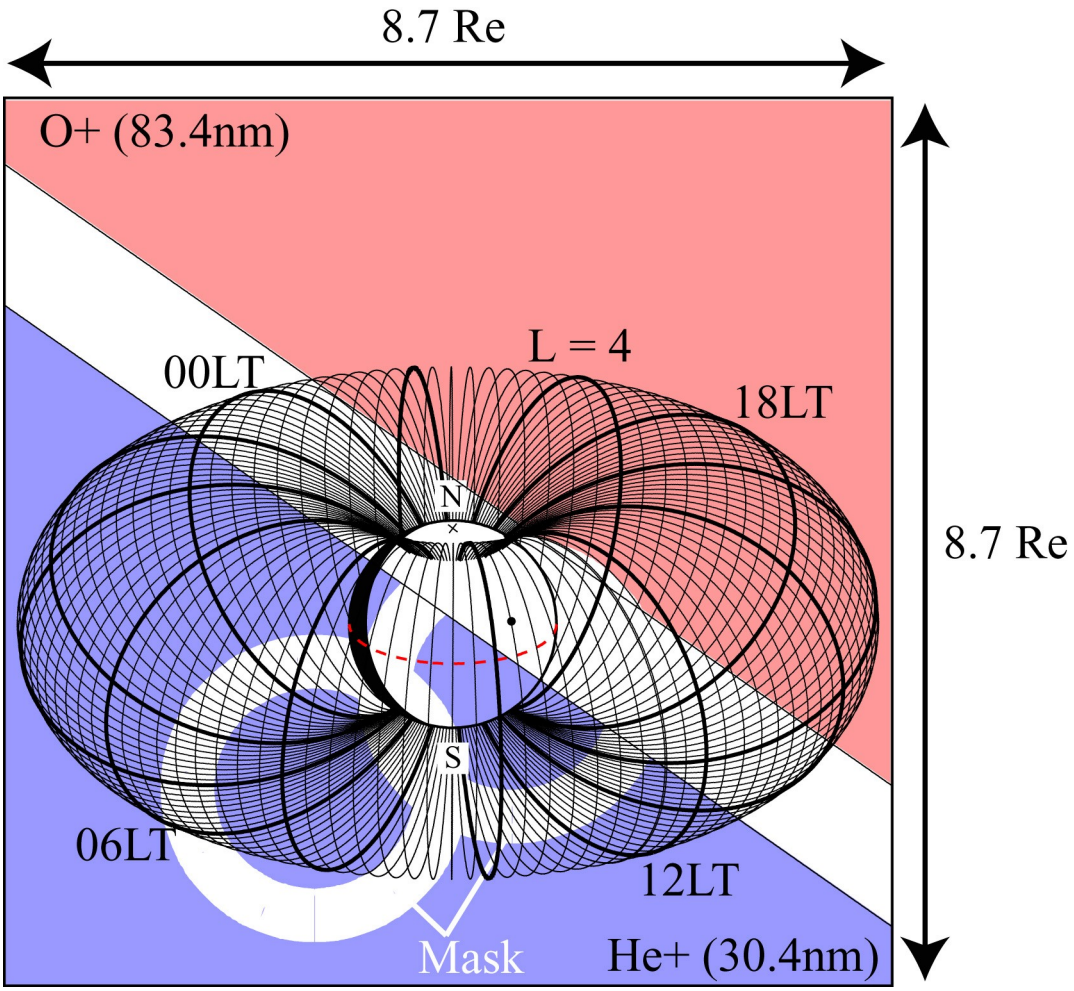

Figure 3.2: View of the geomagnetic field lines seen from KAGUYA. During the observation in June 2008, our telescope gazed down to the Earth's geomagnetic equatorial plane by ~20 deg. Each line indicates a dipolar magnetic field (L = 4). The bold field lines are drawn extending every 2- hour local time. The two white circles are in place to mask the circular ghosts due to an instrument problem.

3.3 Results and discussion

All the plasmaspheric images obtained by TEX from March to June 2008 were analyzed. Prominent phenomena of the plasmasphere, erosion and corotation, were identified in a geomagnetically disturbed and quiet period, respectively. Furthermore, a new striking feature of the plasmasphere was found from the meridian perspective. The detailed studies of these events are presented below.

3.3.1 Inward motion of the nightside plasmapause

There was a succession of geomagnetically quiet days in 2008. Fortunately, the TEX instrument has produced meridian plasmasphere images during a geomagnetically disturbed period from 1 to 2 May. Figure 3.3 shows the geomagnetic conditions (Kp and Dst) and IMF z-component (in GSM coordinates) on 1-2 May 2008. The IMF data, measured by Advanced Composition Explorer (ACE) at the L1 libration point, are time delayed by 54 min to account for propagation to the Earth's magnetopause, assuming the solar wind speed is 470 km/s. The southward turning of the IMF Bz occurred at 20:20 UT on 1 May, and the maximum Kp was 5- during the observation.

Figure 3.4a−c show three EUV snapshots obtained by TEX on 1-2 May 2008. The apparent size and location of the Earth, the day-night terminator, the equator (dashed lines), and sub-solar point (dots) are indicated. The dipole magnetic field lines (L = 2, 3, and 4) at 03 and 15 MLT are also shown. To improve the signal-to-noise ratio, (1) all the images in the same revolution were accumulated to one image and (2) 2 × 2 pixel binning was used (1 bin = 0.14 Re). The sharp He^+ edges in the nightside are identified in Figure 3.4b and c. The nightside edges are aligned to L shells of L = 3.6 and L = 3.2 at 03 MLT, respectively (red broken lines). The detailed study about the temporal and spatial variation of the meridional distribution during this period is demonstrated in Chapter 4.

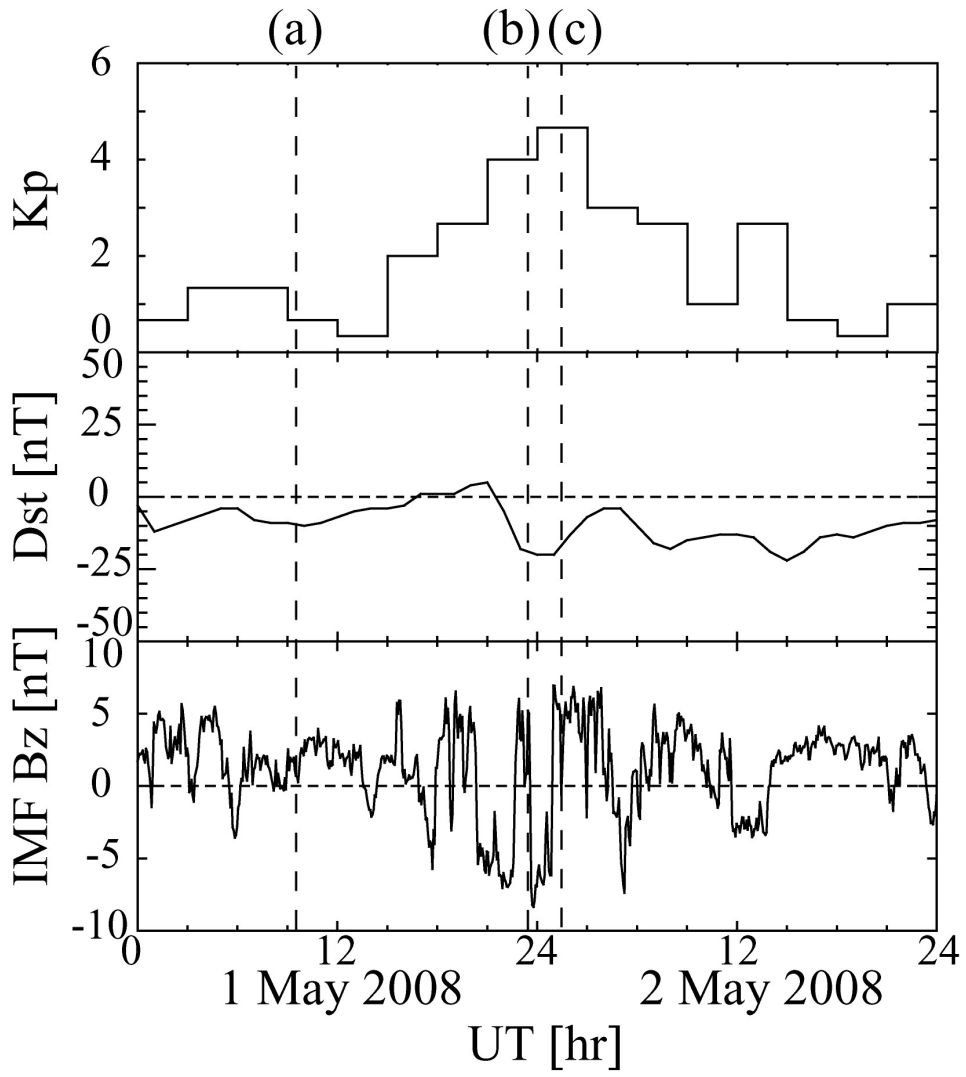

Figure 3.3: Geomagnetic conditions and IMF z-component (in GSM coordinates) on 1-2 May 2008. Vertical dashed lines indicate the observation periods corresponding to each panel of Figure 3.4. We used the IMF data measured by the MAG instrument onboard the ACE satellite. The IMF data is presented with a 54-min time delay to compensate for the propagation from the measurement point to the Earth.

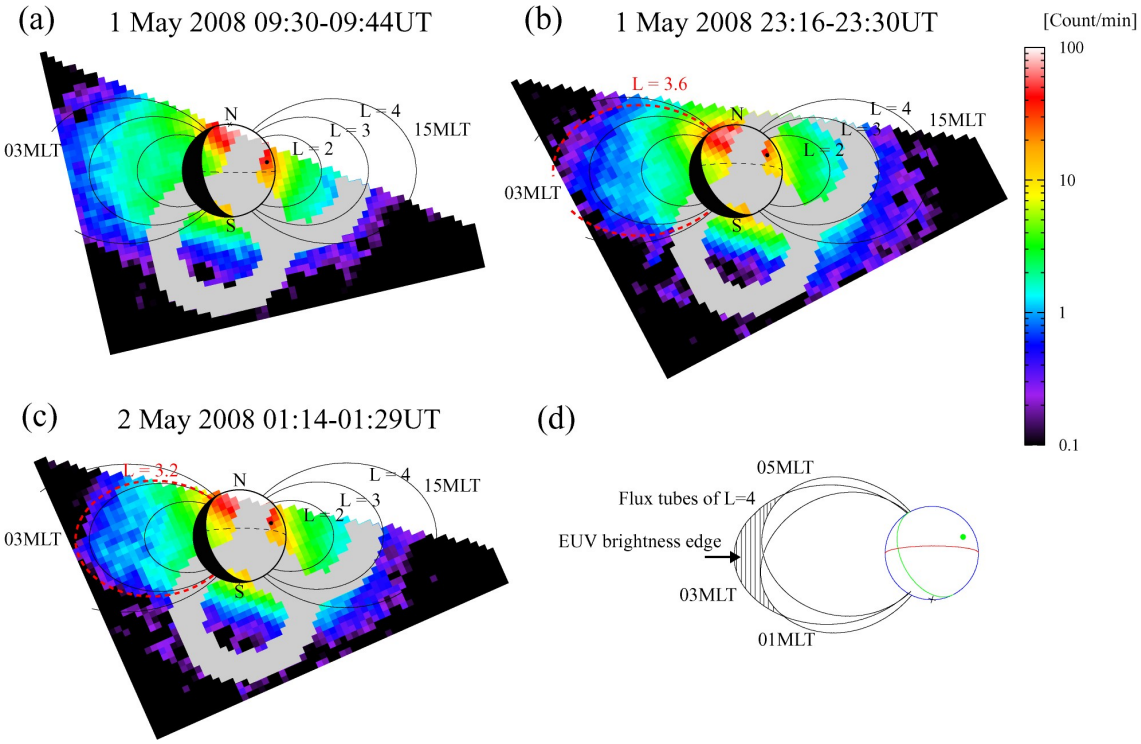

Figure 3.4: (a-c) Three EUV plasmaspheric images from the meridian view taken on 1-2 May 2008. The Earth is located near the upper edge of each image. The dashed arc on the Earth represents the geomagnetic equator and the dot on the Earth is the sub-solar point. The two gray circles are put in order to mask the circular ghosts due to an instrumental trouble. The geomagnetic field line of each L-shell (L=2, 3, and 4) are indicated in the meridional plane at 3-15 magnetic local time (MLT). The inward motion of the plasmapause is clearly seen in the nightside. (d) Flux tubes seen from the lunar orbit. The nightside EUV brightness reflects the plasma distribution at 03 MLT rather than adjacent local times.

Goldstein et al. [2003a] verified that the location of the EUV outer boundary corresponds to the plasmapause by comparing the IMAGE/EUV images with in-situ measurements. In addition, *Obana et al.* [2010] found the agreement between the EUV outer boundary observed by the TEX instrument and the plasmapause location observed by the ground-based magnetometers. According to these studies, we also assume that the sharp He^+ edge does correspond to the plasmapause. In this study, the

EUV outer boundaries were determined along count rate of 0.4 count/min/bin which corresponds to the lower sensitivity threshold achieving SNR of ~2. This determination is reasonable because the EUV intensity from the plasmasphere main-body is generally higher and that from the plasmatrough is lower than the threshold. In our simple estimation assuming the plasmaspheric density based on the statistical in-situ measurement by *Carpenter and Anderson* [1992], the sharp plasmapause ($\Delta L = 0.05$), and the negligible plasmatrough density, the location of the lower sensitivity threshold coincides that of the plasmapause within 0.1 Re at the L-shell below 5. At the larger L-shell the plasmapause location is underestimated in this method. The uncertainty of this plasmapause determination can be estimated to ±1 bin = ±0.14 Re.

Because the nightside EUV radiation at the edge comes from the plasmasphere at 03 MLT rather than adjacent local times, as shown in Figure 3.4d, the brightness edge consists of the outermost L shell in the plasmasphere. If we assume a featureless and azimuthally smooth plasmapause at the nightside, the edges should be interpreted as the plasmapause with L = 3.6 at 03 MLT in Figure 3.4b and with L = 3.2 at 03 MLT in Figure 3.4c.

Based on the results of the long-term in-situ observations by the ISEE 1 satellite, *Carpenter and Anderson* [1992] modeled the plasmapause location as follows:

$$Lpp = 5.6 - 0.46 Kp_{\max}, \tag{3.1}$$

where Kp_{max} is the maximum of Kp value over an interval of several hours and up to a day prior to the observation (details are mentioned in Chapter 1). The location predicted by this conventional empirical model is 3.7 for the Figure 1b period and 3.3 for the Figure 1c period. These values are consistent with the results of the TEX observations.

The IMF was clearly northward until 18 UT on 1 May. The geomagnetic activity was quite low with average Kp of 1. A gradual decrease of brightness (density)

with increasing L shell is seen in Figure 3.4a, as is typically seen in our EUV images of the plasmasphere obtained after prolonged periods of low geomagnetic activity. The earlier successful mission IMAGE-EUV produced EUV images over several years, and *Goldstein et al.* [2005] reported a similar behavior as seen from a high-latitude perspective by IMAGE-EUV during quiet periods.

From 20 UT to 23 UT on 1 May, the IMF polarity turned to southward, and the geomagnetic activity (Kp) increased up to 5-. Dst decreased with a rate of 10 [nT/h] at 21 UT. Comparing the three EUV images in Figure 3.4, it is clear that the nightside plasmapause moved inward. It is likely that the enhanced convection electric field triggered by the southward turning of the IMF generated a new E × B drift trajectory. The diffuse EUV outer boundary at the nightside (Figure 3.4a) then began moving inward, forming a clear boundary. If we compare the outermost L shells described in Figure 3.4b and c, the mean speed was approximately 0.2 Re/h and the total displacement was about 0.4 Re on the equatorial plane. The determination of the plasmapause location is some ambiguous, and we found the subjectivity to be ± 0.14 Re, as mentioned above. The subjective error is smaller than the total displacement, and we estimate the mean inward speed with uncertainty as 0.2 ± 0.14 Re/h. The mean speed of the EUV outer boundary, deduced from the IMAGE/EUV data obtained during a similar geomagnetic trend on 22 April 2001, was 0.3 Re/h [*Murakami et al.*, 2007]. This is not inconsistent with our result.

3.3.2 Corotation of the plasmasphere

On 1-2 June 2008, the geomagnetic activity was quite low, and no geomagnetic storms had been identified since May 23. Figure 3.5 shows the geomagnetic conditions (Kp and Dst) and IMF z-component (in GSM coordinates) on 1-2 June 2008. The maximum Kp was 3- during the observation, and that was 3 in the previous 24-hour. The IMF, measured by ACE at the L1 libration point, had a relatively northward tendency except the very short period.

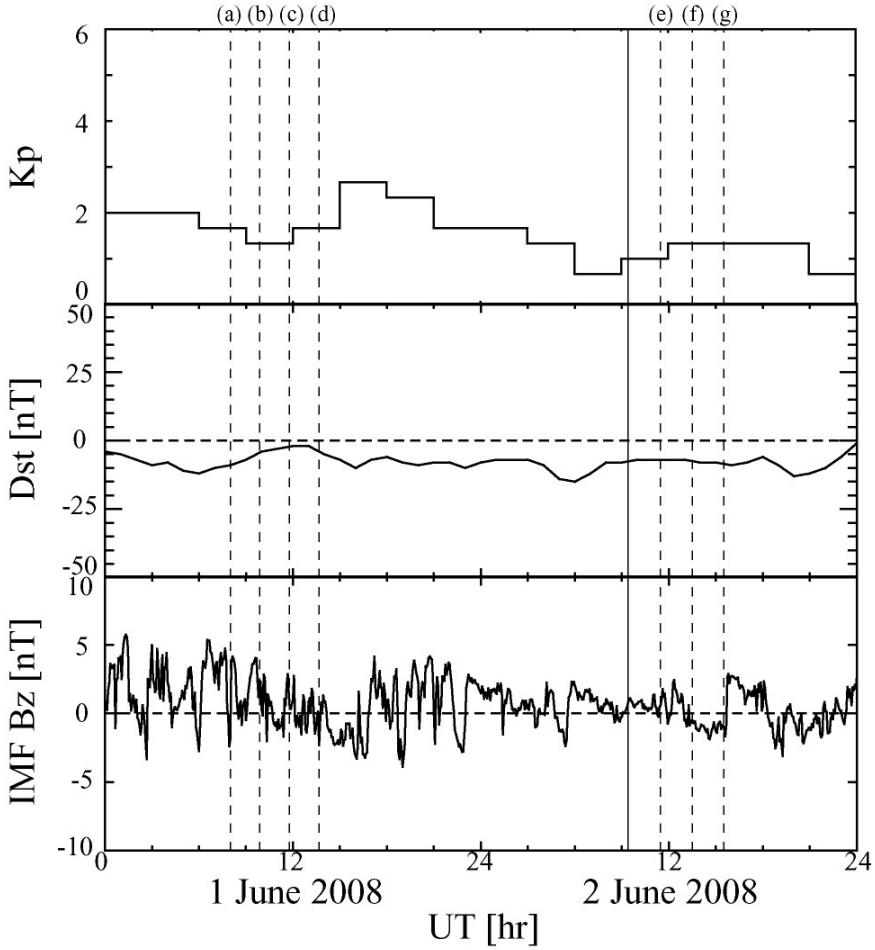

Figure 3.5: Geomagnetic conditions and IMF z-component (in GSM coordinates) on 1-2 June 2008. In this period the geomagnetic activity was quite low. Vertical dashed lines indicate our observation periods corresponding to each panel of Figure 3.6. We used the IMF data measured by the MAG instrument onboard the ACE satellite. The IMF data is presented by 44-min time-delay. The vertical solid line indicates the observation period of the plasmaspheric filament, described in section 3.3.3 and Figure 3.8.

Figure 3.6 presents consecutive snapshots of the plasmasphere obtained by the TEX instrument on 1-2 June 2008. All the images in the same revolution were accumulated into one image and the 2 × 2 pixel binning was used in order to increase the signal-to-noise ratio. The Earth is located near the upper edge of each image. The dashed arc on the Earth represents the Earth's geomagnetic equator and the dot on the

Earth indicates the sub-solar point. During this period, the TEX instrument gazed down the Earth from the Moon and the North Pole is presented as a cross mark in each image. The inner and outer contour lines are drawn at count rates of 2.0 and 1.0 count/min, respectively. The two white circles are put in order to mask the circular ghosts explained in the previous section. For reference, the geomagnetic field lines (L=3) are indicated with magnetic local time (MLT) to align the enhanced density structure. The magnetic field line in the consecutive images from (b) to (d) is identical, i.e., it corotates with the Earth (24-hour duration). The magnetic field line described in (e)-(g) is also identical, but it is described with 2-hour lagged from that in (b)-(d). The images (b)-(d) were taken every 2-hour, and the images (e)-(g) were also taken with the same routine.

In Figure 3.6(a), there seems to be no prominent features in the midnight-to-dawn region except for the shadow. On the other hand, a medium-scale density structure, indicated by a black arrow, exists in the dawnside in (b)-(g). The distribution of this structure inside the plasmasphere clearly agrees with the dipole magnetic field line. Though it could not be distinguished from our view direction as terms (e.g., shoulders) discovered by IMAGE satellite, this is the first result to succeed in imaging a meridional density structure in the plasmasphere.

Furthermore, we clearly identify that the density structure rotates with the Earth in the dawnside. In Figure 3.6(b), a part of the structure was likely to be in the Earth's night shadow. Next, it rotated endways together with the field line in (c) and (d). While it passed through the dayside, it was difficult to be seen due to the high background luminosity (i.e., the main body of the plasmasphere) and due to the intersection with the ghost area (two white circles). No image is shown here for this period. The next day, the structure appeared in the dawnside and corotated with the Earth as seen in (e)-(g). Comparisons of images (b)-(d) with (e)-(g) show the corotation-lag of approximately 2 hours/day. (It should be remembered that the magnetic field line in the images from (e) to (g) is not identical to that in the upper images, but it is lagged by 2 hours.) Thus, the corotation rate, that is the ratio of the observed angular velocity to that of the Earth’s rotation, was ~0.9 in this study.

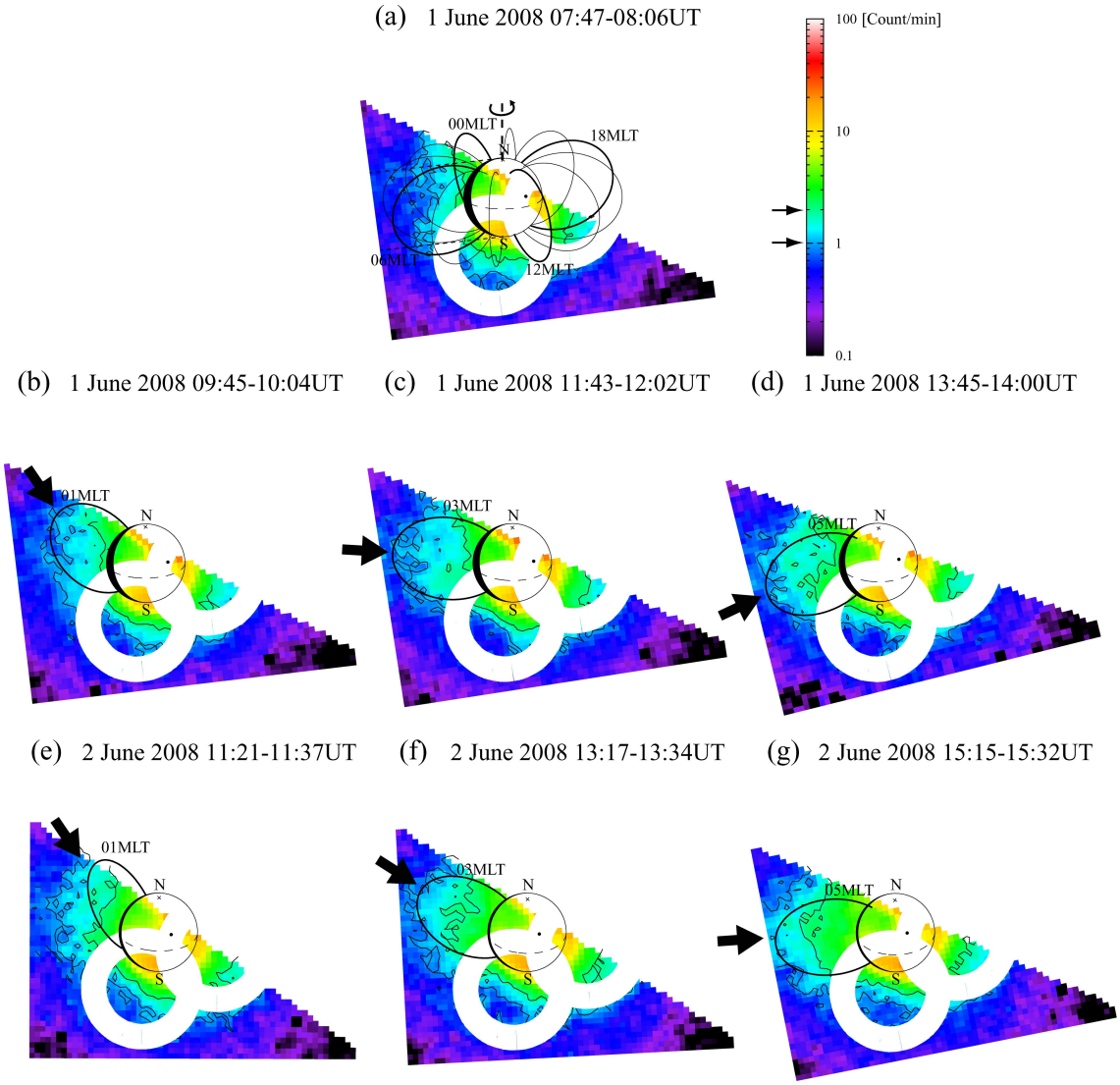

Figure 3.6: Seven EUV images obtained by the TEX instrument on KAGUYA. The image was taken every 2-hour except for the period between (d) and (e). The Earth is located near the upper edge of each image. The dashed arc on the Earth represents the geomagnetic equator and the dot on the Earth is the sub-solar point. The inside and outside contour lines are drawn at count rates of 2.0 and 1.0 count/min, respectively. The two white circles are put in order to mask the circular ghosts due to an instrumental trouble. The geomagnetic field lines (L=3) are indicated with magnetic local time (MLT) to align the enhanced density structure. Except for the image (a), an enhanced density structure, indicated by the black arrow, is clearly seen in each image. It is noted that the magnetic field line

in the consecutive image from (b) to (d) is identical, i.e., it corotates with the Earth. The magnetic field line in the series of image from (e) to (g) is also identical, but it is lagged by about 2 hours from that in (b) to (d).

Sandel et al. [2003] reported the first evidence that the main body of the plasmasphere does not always corotate with the Earth. They tracked notches, persistent distinctive lower-density regions seen in EUV images obtained by the IMAGE satellite, to infer the motion of particular volume elements of plasma. They reported that the corotation rate ranges between 0.77 and 0.93 in the thirteen episodes they used. *Burch et al.* [2004] argued that the departures from corotation in the plasmasphere are driven by corresponding motions of plasma in the ionosphere, where departures from corotation are often observed. They compared DMSP measurements of ionospheric ion drifts to the motion of a notch in the plasmasphere observed by EUV at the same time, and found the consistency between both observations. They suggested that ionospheric corotation lag arises from the ionospheric disturbance dynamo [*Blanc and Richmond* 1980]. Heating of the auroral ionosphere by currents and precipitating particles drives transport towards the equator. As the winds move to lower latitudes, conservation of angular momentum leads to a departure from corotation that takes the form of a westward drift.

A recent study by Galvan et al. [*Galvan et al.*, 2008] found that the plasmasphere on average sub-corotates with 28 hours. *Gallagher et al*. [2005] studied the azimuthal motion of 18 notches seen in EUV pictures taken by the IMAGE satellite, and reported the corotation rate ranges 0.85-0.97. The detailed review of such sub-corotation in the plasmasphere was demonstrated by *Darrouzet et al.* [2009]. The corotation rates reported in the past and estimated in this study are summarized in Figure 3.7. The value of 0.9 in our EUV images seen from the meridian view is not inconsistent with their conclusion based on the observation from the aerial view.

These two results, presented in Section 3.3.1 and 3.3.2, confirmed that the TEX instrument successfully obtained the spatial distribution and temporal variation of

the plasmasphere from the meridian perspective. In the following section, the analysis and discussion on a new striking feature in the plasmasphere first observed by the TEX instrument are performed.

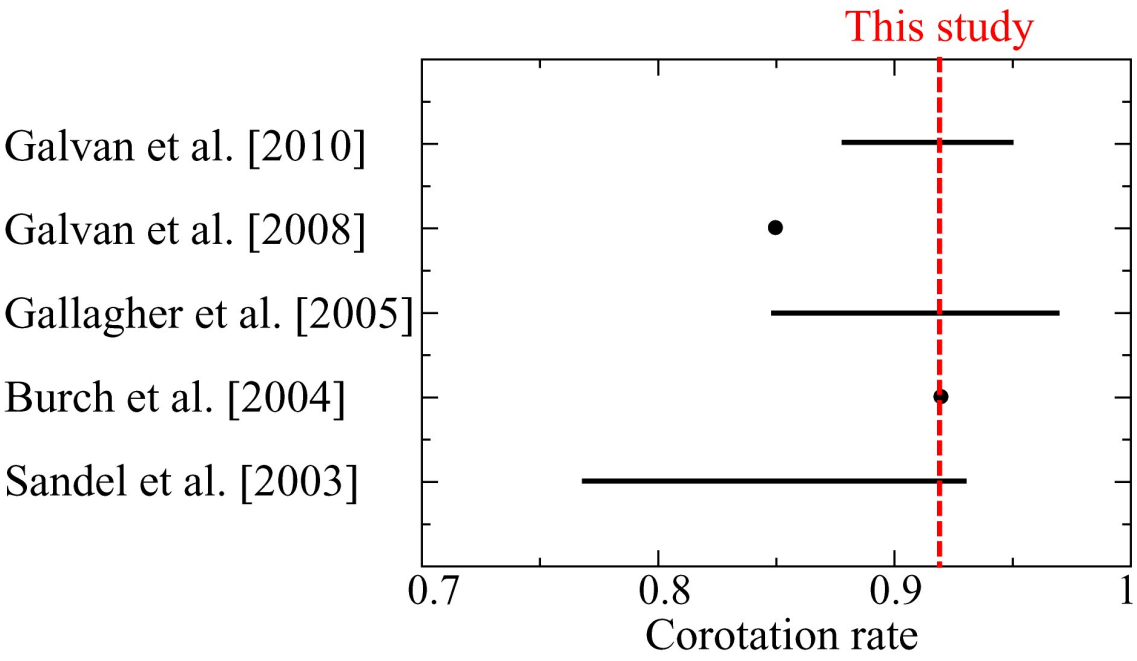

Figure 3.7: Summary plot of the corotation rate in the plasmasphere reported in the past studies and in this study. The horizontal scale indicates the ratio of the observed rotation velocity to that of the Earth's rotation.

3.3.3 Plasmaspheric filament: An isolated magnetic flux tube filled with dense plasmas

We discovered a new striking feature of the plasmasphere during a prolonged quiet period. Figure 3.8 presents a snapshot of the plasmasphere obtained by the TEX instrument on 2 June 2008. The image is presented in almost the same manner as each image in Figure 3.6. In Figure 3.8, an arc-shape structure of enhanced brightness is clearly identified as indicated by the red arrow. Here we call this structure a plasmaspheric "filament." The color contour in Figure 3.8 is adjusted in order to emphasize the structure. For reference, the dipole magnetic field line of L = 3.7 at 7.3 MLT is also drawn by the dashed curve.

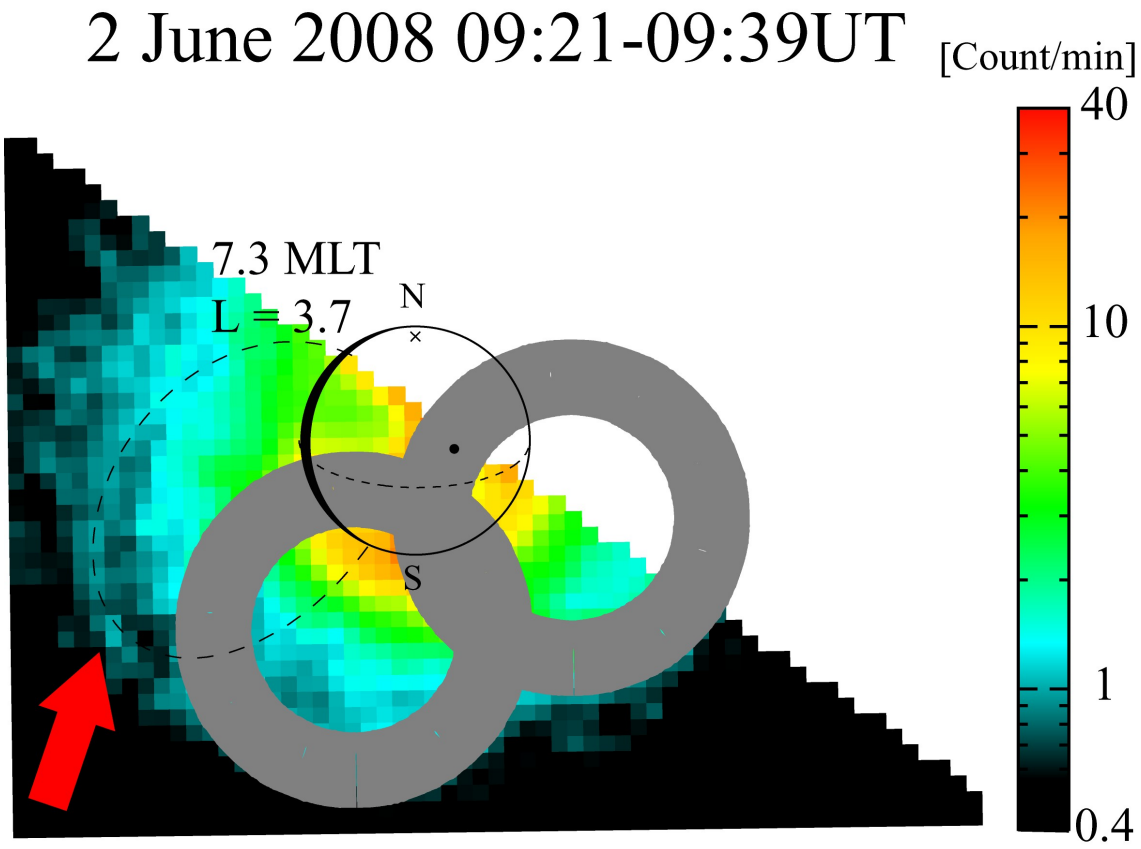

Figure 3.8: An EUV image obtained by the TEX instrument onboard KAGUYA on 2 June 2008. The Earth is located near the upper edge of the image. The dashed arc and the dot on the Earth represent the Earth's geomagnetic equator and the sub-solar point, respectively. The two gray circles are put in order to mask the circular ghosts due to an instrumental trouble. The geomagnetic field line (L = 3.7) at 7.3 MLT is indicated to align the structure of enhanced brightness, the "plasmaspheric filament," pointed by the red arrow.

The shape of this structure seems to be completely agrees with the dipole magnetic field line of L = 3.7 at 7.3 MLT. The magnetic field line that is the most closely aligned to the filament structure was selected as follows. The counts of the pixels in Figure 3.8 were averaged along each dipole magnetic field line (at the magnetic latitude between ±20 deg), and the results are shown in Figure 3.9. A clear peak can be identified at MLT = 7.3 and L = 3.7, indicated by the black circle, and this

means that this magnetic field line is the best fitted to the filament structure. The vertical cross-section profile at 7.3 MLT of Figure 3.9 is presented in Figure 3.10. The increase of the average count at the peak (L = 3.7) comparing to the backgrounds (e.g., L = 3.4 and L =3.9) is larger than the statistical errors. This fact supports the reality of the enhanced brightness along the magnetic field line. This suggests that the filament represents an isolated flux tube filled up to higher density than the neighboring tubes. The TEX instrument first succeeded in identifying the isolated flux tube with dense plasma in the plasmasphere because of imaging from the meridian perspective.

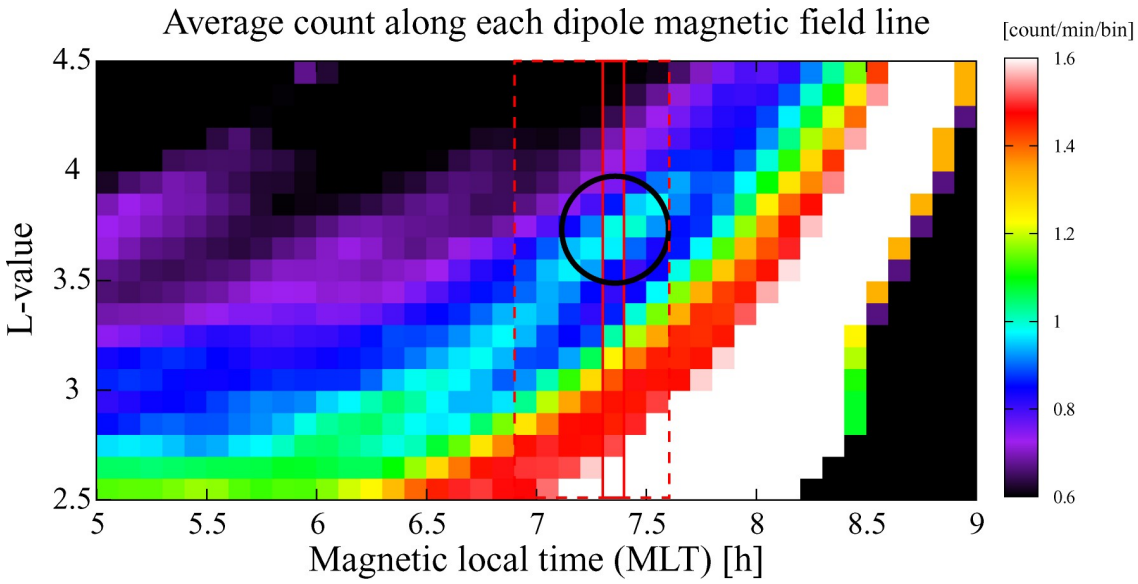

Figure 3.9: The average count along each dipole magnetic field line, derived from the TEX image at 09:21-09:39 UT on 2 June 2008 (shown in Figure 3.8). The counts of the pixel along each dipole magnetic field line (at magnetic latitudes between ±20 deg) were averaged. There exists a peak at MLT = 7.3 and L = 3.7 as indicated by the black circle. The cross-sectional profile at MLT = 7.3 is presented in Figure 3.10. The dashed vertical lines also indicate the range of MLT where the enhancement at the peak is larger than the error bars.

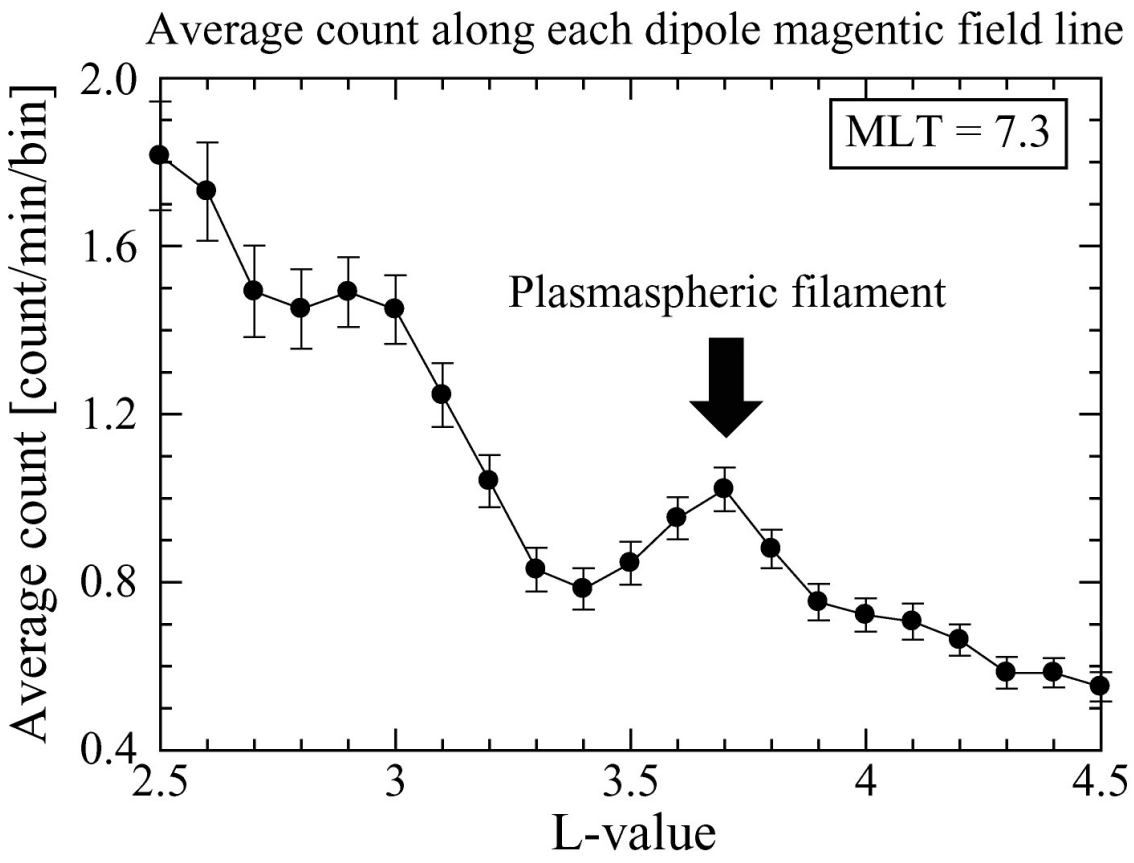

Figure 3.10: The cross-sectional profile at MLT = 7.3 in Figure 3.9. The clear peak at L = 3.7 is indicated by the black arrow, and it corresponds to the plasmaspheric filament seen in Figure 3.8. The error bar gives the standard deviation of accumulated counts along each magnetic field line.

Indeed, the filament structure shown in Figure 3.8 can be simulated by assuming an isolated flux tube filled with denser plasma than its neighbors. Figure 3.11 shows the calculated image of the plasmaspheric filament viewed from KAGUYA on 2 June 2008. In this calculation, we assumed the equatorial density distribution based on the statistical in-situ measurement by *Carpenter and Anderson* [1992] (see Equation 1.1) and the circular shape of the plasmasphere. The He^+ density (n) along the magnetic field line was also assumed to follow radial power law $n = n_0 (L\ Re\ /\ R)^3$, where n_0 is the density at in the equatorial plane and R is the geocentric radius [e.g., *Obana et al.*, 2010]. Inside the flux tube at L = 3.7 (ΔL = 0.3) and MLT = 7.3 (ΔMLT =

0.4) the He^+ density was higher than its neighbors by a factor of 5, which was the typical value of the density enhancement as discussed below. The calculated image in Figure 3.11 is viewed from the same position as the KAGUYA spacecraft at 09:30 UT on 2 June 2008. The dark region at the upper left of the Earth corresponds to the shadow. In the result of our calculation, the intensity of the filament is higher than its neighbors by 13%, and this value is larger than the statistical errors. Comparing Figure 3.11 with Figure 3.8, it is clear that the filament structure is reconstructed by our calculation. Therefore, it is concluded that a plasmaspheric filament corresponds to an isolated flux tube filled with dense plasma.

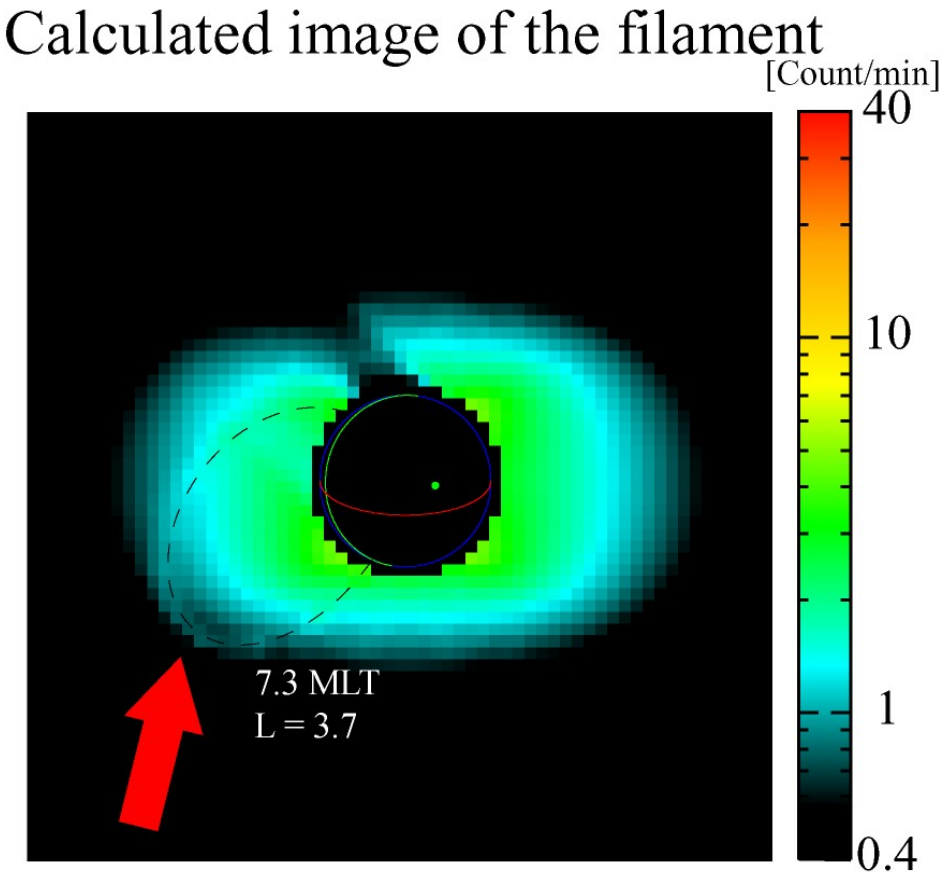

Figure 3.11: A calculated image of a plasmaspheric filament viewed from KAGUYA on 2 June 2008. Inside the isolated flux tube at L = 3.7 and MLT = 7.3 the He^+ density is assumed to be higher than its neighbors by a factor of 5. This image is presented in the same manner as that in Figure 3.8.

We approximately estimated the He^+ density in the filament flux tube and its neighboring tubes at L = 3.7 using the conventional method [*Yoshikawa et al.*, 2000; *Gallagher et al.*, 2005]. The measured brightness is directly proportional to the He^+ column density along the line of sight because the plasmasphere is optically thin for the He II radiation. Observed TEX instrument counts are converted to column density using the following equation derived from the laboratory calibrations:

$$N = a * 1.0 * 10^{20} / F_{30.4}, \quad (3.2)$$

where N is the He^+ column density in cm^{-2}, a is the EUV signal in count/min/bin (for 2 × 2 pixel binning), and $F_{30.4}$ is the solar flux at 30.4 nm in units of photons/cm^2/s. The solar 30.4-nm flux was 3.03×10^9 photons/cm^2/s on 2 June 2008, measured by the SEE instrument onboard the TIMED satellite. Column density can be converted to average density by dividing by an estimate of the distance along the line of sight that contributes most to the image intensity at each location in the field of view [*Gallagher et al.*, 2005]. This technique is applicable since densities in the plasmasphere rapidly fall with increasing L-shell, and thus the inner most regions penetrated by a given line of sight contribute the most to the observed 30.4-nm intensity. In addition to the technique described by *Gallagher et al.* [2005], we used the assumption concerning the azimuthal isotropy of the density in the plasmasphere. This assumption is based on the past density observations which showed only small longitudinal (MLT) dependence [e.g., *Clilverd et al.*, 2007].

In the event on 2 June 2008 shown in Figure 3.8, the average 30.4-nm intensity of the plasmasphere at L = 3.7 was 0.5 count/min/bin, corresponding to the column density of 1.7×10^{10} ions/cm^2. The calculated column length through the L-shell of 3.7 along the line-of-sight was 1.1×10^9 cm. Thus, the average He^+ density in the plasmasphere at L = 3.7 was estimated to be 15 ions/cm^3. This value is consistent with past in-situ measurements of the plasmasphere [e.g., *Carpenter and Anderson*, 1992], considering the low He^+/H^+ density ratio of ～0.05 for the minimum solar

activity [*Craven et al.*, 1997]. On the other hand, the 30.4-nm intensity along the filament was higher than its neighboring bins by 0.25 count/min/bin, and then the column density along the filament was higher by 8.3×10^9 ions/cm^2. If we assume the outer shape of the filament as the cylinder whose diameter is ～2 bins (equal to 0.28 Re), the column length through the filament was estimated to be 2.0×10^8 cm. Therefore, the density inside the filament flux tube is higher than its neighboring tubes at L = 3.7 by 42 ions/cm^3. This means that the filament flux tube is filled with denser plasmas than its neighbors by a factor of ～4.

We searched all the TEX data obtained in the period of March-June 2008, and identified 4 events of the plasmaspheric filament. Table 3.1 shows the date, UT, Kp, L-value and MLT for each event. As the total of the TEX observation periods was ~26 days, the occurrence rate of the plasmaspheric filament identified by TEX was ~1 event / 8 days. It should be noted that all the events were observed during extremely quiet periods, i.e. Kp < 2. Although the geomagnetic activity tended to be low during the TEX observation, this result is not negligible. The dependence of the filament occurrence on MLT was not found in the TEX observation.

Furthermore, all the events of the plasmaspheric filament occurred around the L-value of 3.5. This result may not reflect the nature of the plasmasphere but be caused by some limitations of the observation. At the inner L-shells, it is difficult to identify the filament (enhancement of the brightness) due to the high background luminosity (i.e., the main body of the plasmasphere). On the other hand, at the outer L-shells, the intensity of the filament decreases and it results in the low signal-to-noise ratio. The field-of-view (FOV) of the TEX instrument also limits the opportunity to find the filaments at the outer L-shells.

The plasmaspheric filaments can be compared with the structures called “fingers” observed by IMAGE/EUV [*Sandel et al.*, 2001; *Adrian et al.*, 2004]. The fingers are regions of enhanced brightness having radial extents in the EUV images. *Sandel et al.* [2001] interpreted that these structures represent isolated flux tubes that have been filled to higher densities than neighboring tubes. Our result agrees with their interpretation. The comparisons between the features of the fingers observed by

IMAGE/EUV and the filaments observed by KAGUYA/TEX are summarized in Table 3.2 and described in detail below. Good agreement between them was found.

1. (Occurrence rate:) *Adrian et al.* [2004] found 20 events of the finger in IMAGE/EUV images between February and August 2001. This indicates that the occurrence rate of the fingers identified by IMAGE/EUV is ~1 event / 10 days. This value is consistent with that of the filament observed by TEX.

2. (Geomagnetic activity:) Almost all the fingers were observed by IMAGE/EUV in geomagnetically quiet conditions. The average Kp value of the observation periods listed in *Adrian et al.* [2004] is 1.8. This value is also consistent with the result in this study.

3. (L-value:) The regions of enhanced brightness in the IMAGE/EUV images radially extend to the L-shells of 2-4. In this study the L-shells of the filament concentrates to 3.4-3.7 due to the limitation of the observation discussed above. Nevertheless, these results are not inconsistent.

4. (Local time:) The EUV instrument observed the finger structure corotating over 12 hours [*Sandel et al.*, 2001] and found it at every local time. This result agrees with the result in this study that the filament appears independently of the local time. However, it is difficult to identify the corotation of the filament in the consecutive TEX images due to the instrumental limitations discussed above.

5. (Azimuthal extent:) The azimuthal extents of the fingers are up to 20 deg [*Sandel et al.*, 2001]. Although it is difficult to distinguish the azimuthal (local time) and radial (L-shell) extents in the TEX images, the azimuthal extent of the filament on 2 June 2008 was at most 11 deg (ΔMLT = 0.7 h), as estimated in Figure 3.9. This value is not inconsistent with the results of IMAGE/EUV observations.

6. (Intensity enhancement:) In the case study of the IMAGE/EUV image on 7 June 2000, the EUV intensity of the finger was higher by ~25% than its neighbors at L = 3. In this study the intensity of the filament was higher by ~35% than its neighbors as shown in Figure 3.10, and this value is comparable to that of the finger.

Table 3.1: The event list of the plasmaspheric filament showing the date, UT, Kp, L-value, and MLT

Date	UT	Kp	L-value	MLT
1 April 2008	18:10-18:32	1-	3.5	15.7
8 May 2008	06:54-07:12	1+	3.4	8.0
26 May 2008	02:32-02:46	1-	3.5	21.0
2 June 2008	09:21-09:39	1	3.7	7.3

Table 3.2: The summary of the comparisons between the fingers in the IMAGE/EUV images and the filaments in the KAGUYA/TEX images

	Fingers (IMAGE/EUV)	Filaments (KAGUYA/TEX)
Occurrence rate	~1 event / 10 days[a]	~1 event / 8 days
Geomagnetic activity	Average Kp = 1.8[a]	Kp < 2
Local time	No dependence[b]	No dependence
L-value	L = 2-4	L = 3.4-3.7
Azimuthal extent	< 20 deg[b]	< 11 deg
Intensity enhancement	~25%	~35%

[a][Adrian et al., 2004]

[b][Sandel et al., 2001]

On the other hand, *Adrian et al*. [2004] interpreted fingers as radial He^+ enhancements arising from some resonance of ultra-low frequency waves. In all the TEX data, we found only one event that can be interpreted as such a structure was found. As mentioned in the previous section 3.3.2 and shown in Figure 3.6, the TEX instrument observed a localized density enhancement and its corotation on 1-2 June 2008. We simulated the plasmasphere images with radial He^+ enhancements viewed from KAGUYA by the same way as the previous calculation of the filament shown in Figure 3.11. Each panel of Figure 3.12 represents the calculated image of the

plasmasphere with the radial structure at 01, 03, and 05 MLT. A radial density enhancement by a factor of 5 was assumed at L < 4 with an azimuthal extent of 15 deg. Comparing Figure 3.6b-d and Figure 3.12a-c, the structure obtained by the TEX instrument on 1-2 June 2008 can be interpreted as a radial density enhancement as proposed by *Adrian et al*. [2004], though it cannot be distinguished exclusively from our view direction. Nevertheless, at most one event of the radial density enhancement was identified, while four events of the plasmaspheric filament were identified by the TEX instrument. This suggests that the fingers observed by IMAGE/EUV represent the projection of isolated flux tubes into the magnetic equator plane rather than that of radial density enhancements.

In recent years, many studies demonstrated the correlations between the plasmaspheric and ionospheric density structures. For example, recent comparisons of maps of ionospheric total electron content (TEC) with EUV images show good agreements between plasmaspheric drainage plumes and ionospheric storm enhanced densities (SEDs) [e.g., *Foster et al.*, 2002]. Furthermore, localized plasma density enhancements in the ionosphere (called "plasma blobs") have been observed by in-situ and ground-based observations [e.g., *Yokoyama et al.*, 2007; *Pimenta et al.*, 2007; *Park et al.*, 2008]. This ionospheric structure may cause the localized density enhancements in the plasmasphere through the magnetic field line. However, further investigation is needed to understand the cause of the plasmaspheric filaments. In the future, simultaneous observations of the plasmaspheric filaments and their foot points in the ionosphere will be performed by the EUV Imager from the International Space Station (ISS) (see Chapter 5). Investigating the origin of the plasmaspheric filaments plays a key role to understand the plasmasphere-ionosphere connections, especially the physical process of the plasmaspheric refillngs.

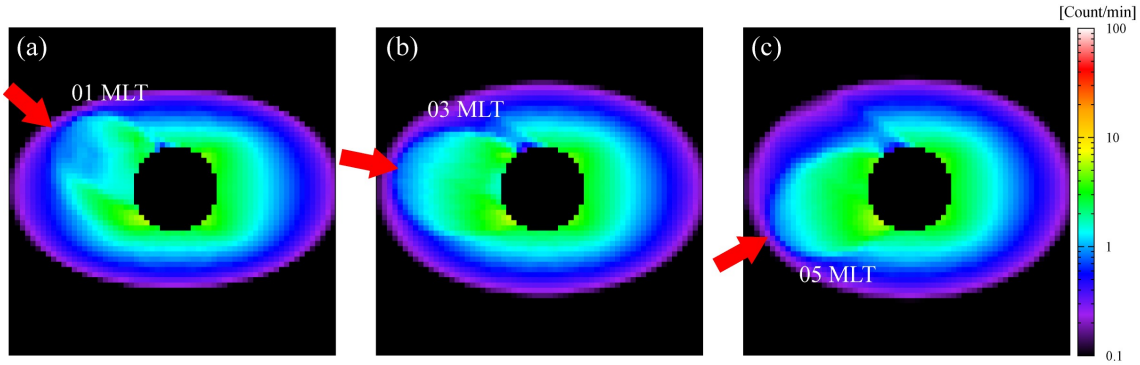

Figure 3.12: Calculated images of radial He^+ enhancements viewed from KAGUYA on 1 June 2008. Localized density enhancement by a factor of 5 at L < 4 was assumed to exist at (a) 01, (b) 03, and (c) 05 MLT with an azimuthal extent of ΔMLT = 1.0.

3.4 Summary

The TEX instrument onboard the KAGUYA satellite obtained the first EUV images of the plasmasphere from the meridian perspective in March-June 2008. The inward motion of the plasmapause in the nightside during the disturbed period on 1-2 May 2008 was clearly observed by the TEX instrument. From the meridian view, the inward speed was estimated to be 0.2 Re/h on the assumption that the plasmapause was featureless and azimuthally smooth on the nightside. This result is consistent with that of the past study based on the IMAGE/EUV data.

The corotation of the plasmasphere during the quiet period on 1-2 June 2008 was also detected by the TEX instrument. A density enhancement inside the plasmasphere was tracked to estimate the angular rotation rate of the plasmasphere. The observed corotation lag of 2 hours/day was consistent with the results from the recent studies derived from the IMAGE/EUV mission. These agreements confirmed that the TEX instrument successfully obtained the spatial distribution and temporal variation of the plasmasphere from the meridian perspective.

Furthermore, a new striking feature of enhanced brightness in the

plasmasphere, called as a plasmaspheric filament, was found in the TEX image during a prolonged quiet period. The shape of the filament was closely aligned to the dipole magnetic field line, and this suggests that the filaments are caused by isolated magnetic flux tubes filled with denser plasmas than their neighbors. We searched all the TEX data obtained in the period of March-June 2008, and identified 4 events of the plasmaspheric filament. The nature of the filament was consistent with that of the finger structure observed by IMAGE/EUV. Consequently, the result indicates that the finger structure seen in the EUV images should be the equatorial projection of isolated flux tubes filled with denser plasmas than its neighbors. The filament may be caused by a localized structure in the ionosphere, such as plasma blobs. Investigation of filaments can play a key role to solve the longstanding issues such as plasmasphere refilling.

4 The plasmapause formation seen from meridian perspective by KAGUYA

4.1 Introduction

The plasmasphere constitutes the extension of the ionosphere at high altitude: cold plasma from the ionosphere moves along magnetic field lines and populates flux tubes forming the plasmasphere. The outer surface in the plasmasphere is often characterized by a sharp decrease in the plasma density, called the plasmapause. Whistler and in-situ satellite observations have revealed that the equatorial position of the plasmapause generally depends on the level of geomagnetic activity and varies from 2.5 Re to 7 Re [*Carpenter and Anderson*, 1992; *Moldwin et al.*, 2002].

It is well admitted that the configuration of cold plasma in the plasmasphere depends on the electric field. This electric field is formed by the interplay of the corotation electric field, which dominates near the Earth, and the convection electric field, generated by the interaction of the solar wind with the magnetosphere. *Nishida et al.* [1966] proposed the first theory for the formation of the plasmapause based on the postulate that the outer edge of the plasmasphere coincides with the last closed equipotential (LCE) of the magnetospheric convection electric field superposed on the Earth's corotation electric field. The details of this longstanding idea are introduced in Chapter 1.

On the other hand, some recent experimental evidences disagree with this conventional theory. The first global comprehensive images of the Earth's plasmasphere were provided by the Extreme Ultraviolet (EUV) imager onboard the IMAGE spacecraft launched in March 2000 [*Burch et al.*, 2000; *Sandel et al.*, 2001]. With these images, the large-scale dynamics of the plasmasphere were revealed. The numerous EUV observations indicate the formation of a sharp plasmapause occurs in the post-midnight sector soon (< 1 hour) after the sudden enhancement of the

convection [e.g., *Goldstein et al.*, 2003b, 2005; *Murakami et al.*, 2007]. In addition, when the convection is very weak for a prolonged period, smooth electron density transitions from plasmasphere to the outer subauroral regions were often observed by in-situ measurements [e.g., *Tu et al.*, 2007]. These results are inconsistent with the conventional theoretical formulation of the plasmasphere. In the conventional theory, the sharp plasmapause appears on the LCE of the electric field after a prolonged quiet period rather than a disturbed period, and it takes over one whole day for the plasmapause to approach slowly its steady state position and settle down along the LCE after the convection electric field changes. These disagreements have been pointed out in several studies [e.g., *Lemaire and Pierrard*, 2008; *Pierrard et al.*, 2009; *Darrouzet et al.*, 2009].

Another mechanism based on quasi-interchange instability has been proposed to explain the plasmapause formation [e.g., *Lemaire*, 1974; 1985; 2001]. This mechanism causes the peeling off of the plasmasphere as a result of sudden enhancements of the convection velocity in the nightside (See Chapter 1). According to this mechanism, the plasma becomes unstable above a Zero Parallel Force Surface (ZPFS) where the parallel component of the gravitational plus centrifugal accelerations is equal to zero [*Lemaire*, 1985, 2001]. The plasma elements above this surface are peeled off and drift away in the plasmatrough region toward the magnetopause or into the magnetotail due to the type-2 quasi-interchange motion. In this scenario, (1) the sharp plasmapause density gradient develops first in the equatorial region, (2) the plasmapause is formed along the equipotential surface along the ZPFS, and (3) the plasmapause formation is occurred in the post-midnight sector where the convection velocity is significantly enhanced and it increases the centrifugal acceleration.

Pierrard and Lemaire [2004] performed the dynamic simulations of plasmapause formation on the basis of this scenario. The plasmapause positions in the geomagnetic equatorial plane predicted by these simulations were successfully confirmed by IMAGE/EUV observations [*Pierrard and Cabrera*, 2005, 2006; *Pierrard et al.*, 2008]. Indeed, the model reproduces quite well the formation of plumes and shoulders observed by IMAGE/EUV. However, the EUV instrument onboard the

IMAGE satellite provides information on only the azimuthal distribution of the plasmapause projected to the equatorial plane. The formation mechanism of the plasmapause remains an open issue, and more experimental evidences from different perspectives are required to reveal it.

The first meridian images of the plasmasphere were provided by the TEX instrument onboard the KAGUYA spacecraft in 2008. In this study, the sequential TEX images during the geomagnetic disturbance on 1-2 May 2008 were analyzed. The plasmapause positions at the post-midnight viewed from the meridian perspective were compared with those predicted by the dynamic simulations. Furthermore, the meridional distribution of the plasmapause was investigated. This study provides an important experimental evidence for the formation mechanism of the plasmapause.

4.2 Methodology

4.2.1 Observation of the plasmapause from the meridian perspective

The TEX instruments onboard the KAGUYA spacecraft successfully obtained the images of the plasmasphere from the meridian perspective between March and June 2008, as demonstrated in Chapter 3. The TEX instrument detects the resonance scattering emissions of He^+ (He II: 30.4 nm). Because the plasmasphere is optically thin for the He II radiation, the measured brightness is directly proportional to the He^+ column density along the line-of-sight. The KAGUYA satellite orbits around the Moon with an orbital period of 2 hours. This provides an observation window of the Earth every 2 hours.

The meridian plasmasphere images during a geomagnetically disturbed period from 1 to 2 May 2008 are used in this study. Figure 4.1, which is the same as Figure 3.3, shows the geomagnetic conditions (Kp and Dst) and IMF z-component (in GSM coordinates) on 1-2 May 2008. The IMF data, measured by Advanced Composition Explorer (ACE) at the L1 libration point, are time delayed by 54 min to account for propagation to the Earth's magnetopause, assuming the solar wind speed is 470 km/s.

The southward turning of the IMF Bz occurred at 20:20 UT on 1 May, and the maximum Kp was 5- during the observation.

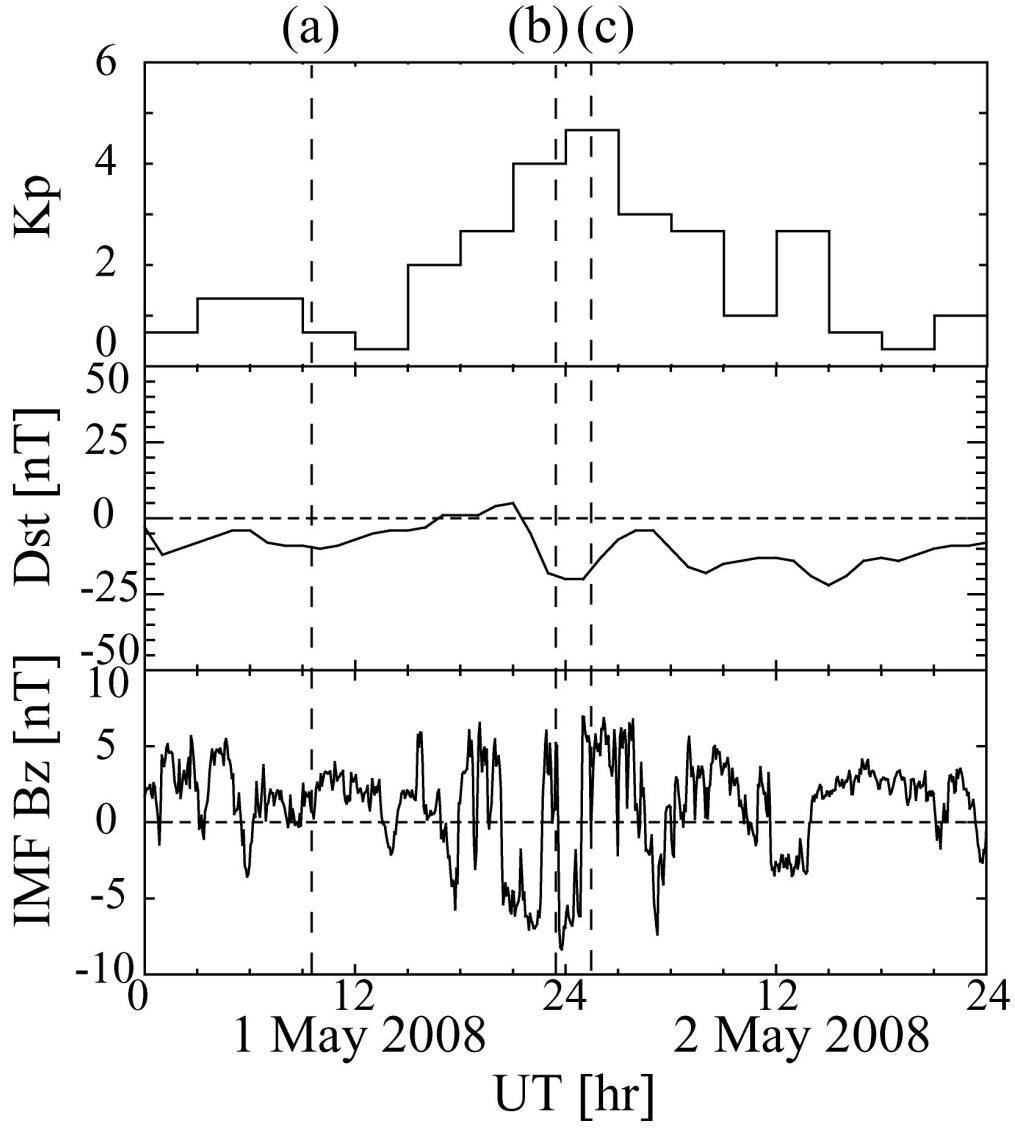

Figure 4.1: Geomagnetic conditions and IMF z-component (in GSM coordinates) on 1-2 May 2008. Vertical dashed lines indicate the observation periods corresponding to each panel of Figure 4.2. We used the IMF data measured by the MAG instrument onboard the ACE satellite. Southward turnings of the IMF Bz occurred at 20:23 and 23:35 UT on 1 May 2008. The IMF data is presented with a 54-min time delay to compensate for the propagation from the measurement point to the Earth. This figure is the same as Figure 3.3.

4.2.2 Calculation of the plasmapause location

In this study, the dynamic simulations based on the physical mechanisms and the numerical method, which are explained by *Lemaire and Gringauz* [1998] and *Pierrard and Lemaire* [2004], are used to calculate the plasmapause locations. This method has been widely used in several recent studies [e.g., *Pierrard and Cabrera*, 2005; *Pierrard and Stegen*, 2008; *Lemaire and Pierrard*, 2008]. The dynamic code that calculates the postion of the plasmapause can be available on the space weather portal (www.spaceweather.eu). The code calculates the locations of the plasmapause versus MLT every hour UT during that given day using the successive values of Kp.

According to the interchange mechanism, the plasmapause is formed along a Zero Parallel Force Surface (ZPFS) where the field-aligned components of the gravitational force and of the centrifugal force balance each other [*Lemaire*, 1985; 2001]. The radial distance of the ZPFS in the geomagnetic equator is given by

$$L_Z = \left(\frac{2GM_E}{3\Omega^2 R_E} \right)^{1/3} = 5.78 \left(\frac{\Omega_E}{\Omega} \right)^{2/3}, \qquad (4.1)$$

where $G = 6.6726 \times 10^{-11}$ m^3 s^{-2} kg^{-1} is the gravitational constant, $M_E = 5.976 \times 10^{24}$ kg is the mass of the Earth, $\Omega_E = 7.29 \times 10^{-5}$ rad s^{-1} is the angular velocity of the Earth, and Ω is the local angular velocity of the plasma. When the rotation rate of the plasma is equal to the angular velocity of the Earth, the ZPFS intersects the equatorial plane along a circle whose radius is equal to 5.78 R_E. The drift velocity of plasma is given by

$$\frac{\vec{E} \times \vec{B}}{B^2}, \qquad (4.2)$$

and the angular drift velocity is given by

$$\Omega(r) = \frac{\left|\left(\vec{E}_{tot} \times \vec{B}\right) \times \vec{r}\right|}{r^2 B^2}, \qquad (4.3)$$

where E_{tot} is the total electric field of the convection and the corotation.

The Kp-dependent empirical electric field model E5D [*McIlwain*, 1986] is used in this dynamic simulation to determine the convection velocity, and ultimately the location of the plasmapause. The E5D electric field model is derived from dynamic proton and electron spectra measured onboard the geostationary satellites ATS-5 and 6. This empirical electric field is fully determined only by the values of Kp. During a geomagnetic disturbance, the angular rotational speed of the magnetospheric plasma is accelerated due to the enhanced convection electric field in the post-midnight sector. Consequently the minimum equatorial distance of the ZPFS is reduced and the nightside plasmapause moves inward. For instance, the ZPFS locates at 2.8 Re from the Earth for the angular rotation speed faster than the Earth's rotation by a factor of 3 ($\Omega = 3\Omega_E$).

The deepest penetration of the ZPF surface is located around 02:00 LT where the convection electric field accelerates the angular velocity of the corotating plasma and is most enhanced in the E5D model. Once the minimum radial distance for the ZPF surface has been calculated as indicated above, the MHD drift velocity is used to calculate the positions of the plasmapause in following MLT sectors.

Other magnetospheric convection electric field models are available in the literature and some of them have been used to determine the positions of the plasmapause by *Pierrard et al.* [2008]. Among all most popular electric field models tested by these authors (Volland-Stern, E5D, and Weimer), it happens that the E5D model offers the results that were in slightly best agreement with the observations from IMAGE/EUV for the cases examined in their comparative study. According to their result, the E5D electric field model is used in this study.

It has been inferred from IMAGE/EUV [e.g., *Burch et al.*, 2004] and KAGUYA/TEX observations (see Section 3) that the azimuthal velocity of the

plasmasphere is slower than corotation in the outermost layers of the plasmasphere. This effect is taken into account in the simulation by reducing the corotation potential. In this study, the rotation rate of 90% corotation is used based on the result in Section 3.3.2.

4.3 Analysis and discussion

4.3.1 Comparisons of the plasmapause positions between the TEX observations and numerical simulations

The plasmaspheric images obtained by the TEX instrument from 09:30 UT on 1 May 2008 to 01:29 UT were analyzed. In order to increase the signal to noise ratio, all the images observed in the same spacecraft revolution were accumulated to one image (i.e., exposure time of ~15 min) and 2 × 2 pixel binning was used. Figure 4.2 shows the EUV plasmaspheric images from the meridian view taken by TEX at (a) 09:30-09:44 UT on 1 May, (b) 23:16-23:30 UT on 1 May, and (c) 01:14-01:29 UT on 2 May 2008. In these periods the line-of-sight of TEX was perpendicular to the meridional plane at 03-15 MLT. The apparent size and location of the Earth, the equator (red lines), the day-night terminator (green lines), and sub-solar point (green dots) are indicated. The dipole magnetic field lines at 03 and 15 MLT are shown. The color contour is proportional to the logarithm of the count rate, corresponding to the intensity of resonantly scattered light (at 30.4 nm) from helium ions. The average background of 1.8 cps/cm^2 (corresponding to 0.16 count/min/bin), described in Section 2.3.3, was subtracted from each image. The sharp He^+ edges, corresponding to the plasmapause at 03 MLT, are clearly identified as indicated by red lines in Figure 4.2. As shown in Figure 4.1, southward turnings of the IMF Bz occurred at 20:23 and 23:35 UT on 1 May 2008. The inward motion of the nightside plasmapause due to the enhancement of the convection electric field is clearly seen in Figure 4.2.

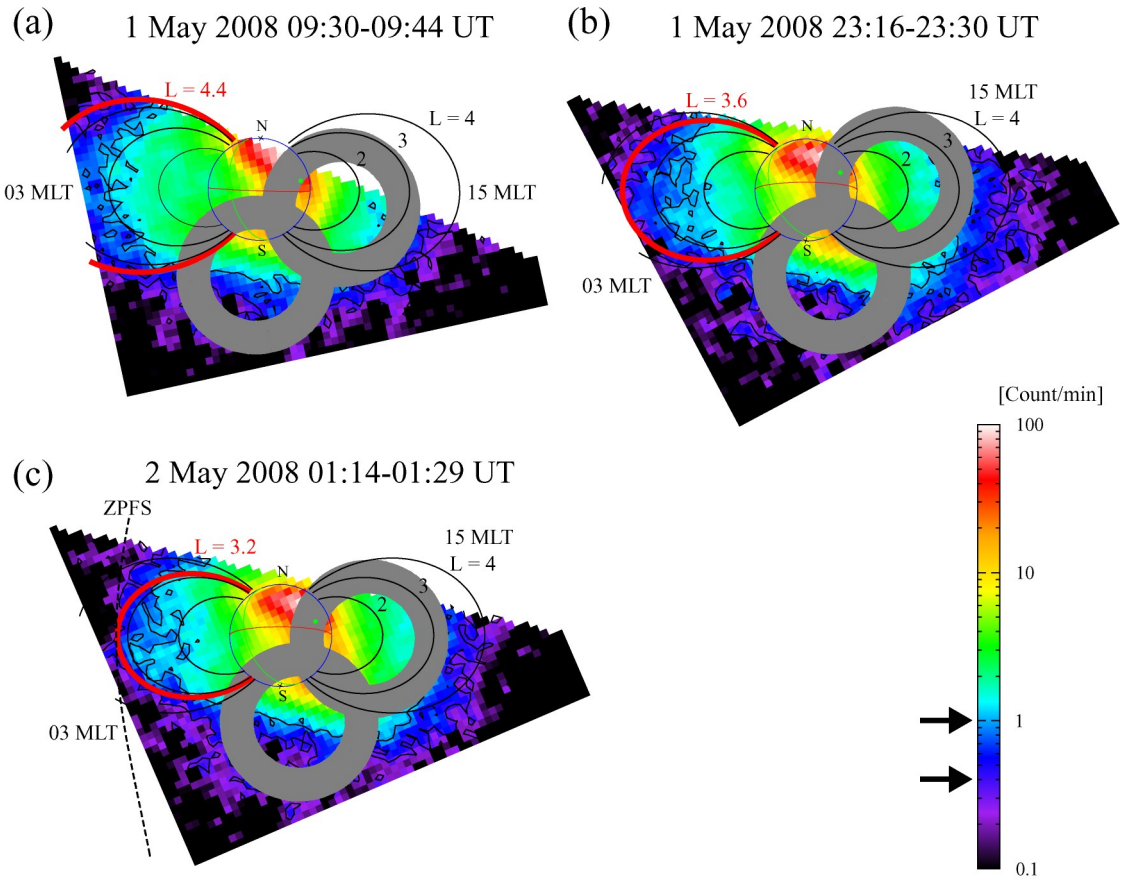

Figure 4.2: Three EUV plasmaspheric images from the meridian view taken by TEX at (a) 09:30-09:44 UT on 1 May, (b) 23:16-23:30 UT on 1 May, and (c) 01:14-01:29 UT on 2 May 2008, which are almost the same as Figure 3.4. In these periods the line-of-sight of TEX was perpendicular to the meridional plane at 03-15 MLT. The Earth is located near the upper edge of each image. The red arc on the Earth represents the geomagnetic equator and the green dot on the Earth represents the sub-solar point. The two gray circles are put in order to mask the circular ghosts due to an instrumental trouble. The color contour is proportional to the logarithm of the count rate, corresponding to the intensity of resonantly scattered light (at 30.4 nm) from helium ions. Contour lines at 1.0 (inner) and 0.4 (outer) count/min are superposed. The geomagnetic field line of each L-shell (L=2, 3, and 4) is shown. The location of each nightside plasmapause is indicated by red bold line. The inward motion of the plasmapause is clearly seen in the nightside. The location of the ZPFS at 03 MLT is also represented by the dashed line in (c).

Dynamic simulations based on the interchange mechanism were also performed. Figure 4.3 represents the examples of the simulation results at (a) 09:30 UT on 1 May, (b) 23:30 UT on 1 May, and 01:30 UT on 2 May 2008. The time of each panel corresponds to the observation period of the TEX instrument presented in Figure 4.2. The plasmapause in the geomagnetic equatorial plane are shown as the black dots in each panel. The inward motion of the nightside plasmapause at 03 MLT due to the convection enhancement can be identified.

In order to compare the TEX observation and the dynamic simulation, the plasmapause locations at 03 MLT in the geomagnetic equatorial plane are identified both in the TEX images and the simulation results on 1-2 May 2008. Figure 4.4 shows the temporal variation of the plasmapause locations in the geomagnetic equatorial plane at 03 MLT. The subjective error to determine the plasmapause in the TEX image was estimated to be ±0.14 Re, as discussed in Chapter 3. The TEX images during 16-19 UT were not available. The arrival time of the southward IMF at the dayside magnetopause (20:23 UT) is also indicated by the vertical dashed line in Figure 4.4. After the southward turning of the IMF Bz, the plasmapause moves inward both in the calculation and the TEX observation. The locations of the plasmapause observed by TEX completely agrees with the calculation results, except at 15:30 and 21:30 UT on 1 May 2008.

The difference between the calculation and the observation at 15:30 UT occurred due to a bulge formation. In the result of the calculation at 09:30 UT (in Figure 4.3a), a bulge (or a remaining plume) is located near 21 MLT. This structure corotated and was located near 03 MLT at 15:30 UT. Thus the plasmapause location at 15:30 UT was quite far from the Earth (L = 4.8) in the calculation result. On the other hand, the TEX observation demonstrated that the plasmapause at 15:30 UT was closer to the Earth (L = 4.4). The bulge-like structure predicted in the calculation was not detected by the TEX instrument. Nevertheless, this disagreement is not important for this study because the bulge formation is largely dominated by the E×B drift motion at the dayside rather than the plasmapause formation at the nightside.

The difference of the temporal response to the southward IMF between the

calculation and the observation can cause the disagreement of the plasmapause location at 21:30 UT. *Murakami et al.* [2007] reported that the nightside plasmapause starts to move inward 10-30 min after the southward turning of the IMF Bz. The result of the TEX observation is not inconsistent with this timescale. However, the empirical electric field model E5D used in the dynamic simulation depends on the 3-hourly Kp geomagnetic activity index, so it cannot reproduce the quick response of the plasmapause. It is needed to develop empirical models of higher time resolution for the magnetospheric electrostatic field distribution in order to test quantitatively and more definitely the theories for the plasmapause formation by comparing their theoretical predictions to observations. Nevertheless, the locations of the nightside plasmapause predicted by the dynamic simulation agree with those identified in the TEX images (obtained every 2 hours). This study suggests that the plasmapause formation theory based on the interchange mechanism is consistent with the TEX observation from the meridian perspective.

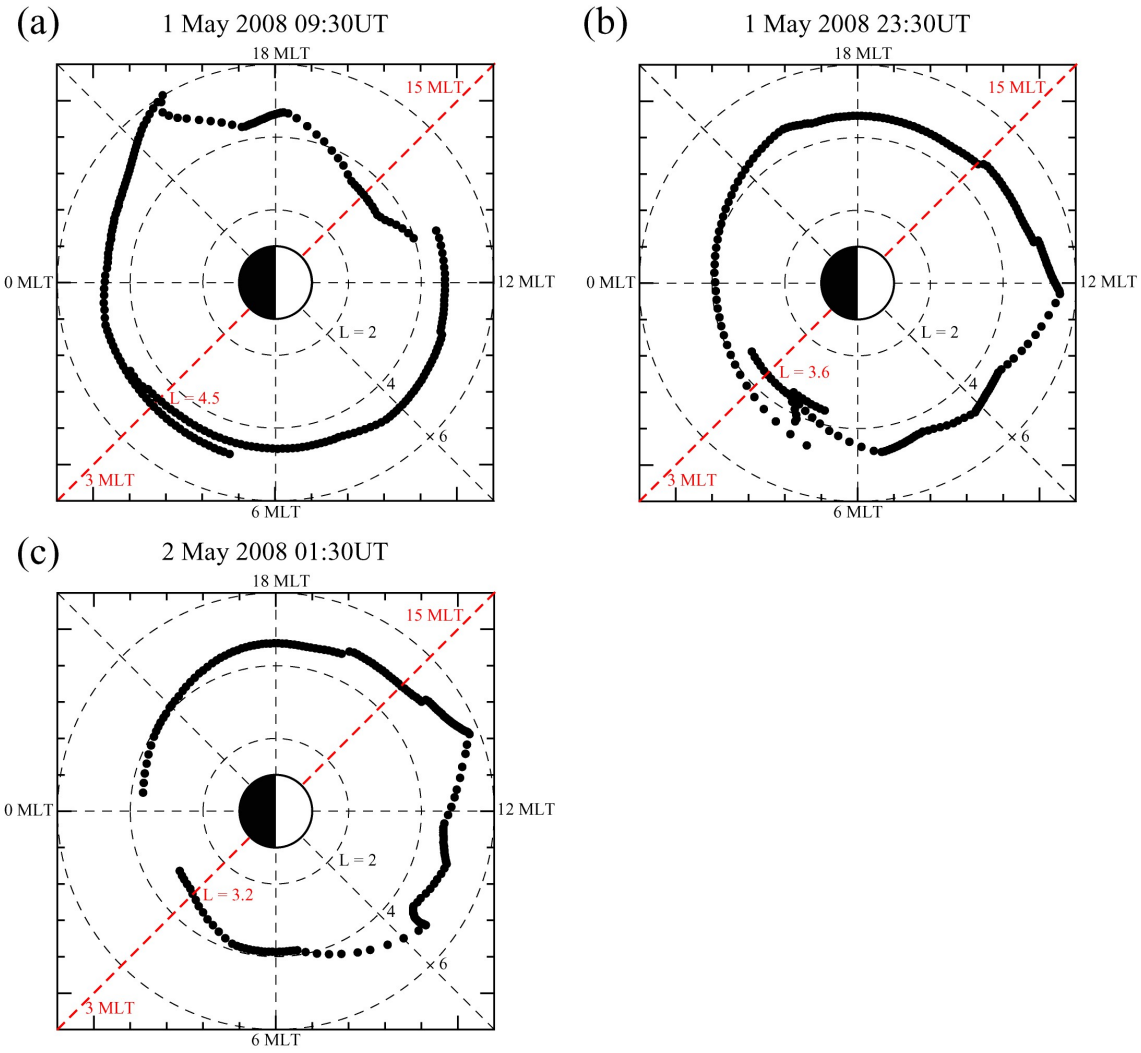

Figure 4.3: Results of the simulation based on the interchange mechanism at (a) 09:30 UT on 1 May, (b) 23:30 UT on 1 May, and 01:30 UT on 2 May 2008. The plasmasphere is viewed from a point of view above the North Pole. The plasmapause in the geomagnetic equatorial plane corresponds to the black dots in each panel. The dashed circles on each figure correspond to a radial distance of 2, 4, and 6 Re. The meridonal plane at 03-15 MLT, which is perpendicular to the line-of-sight from the TEX instrument, is also shown as a red dashed line in each panel. The time of each panel approximately corresponds to the observation period of the TEX instrument presented in Figure 4.2.

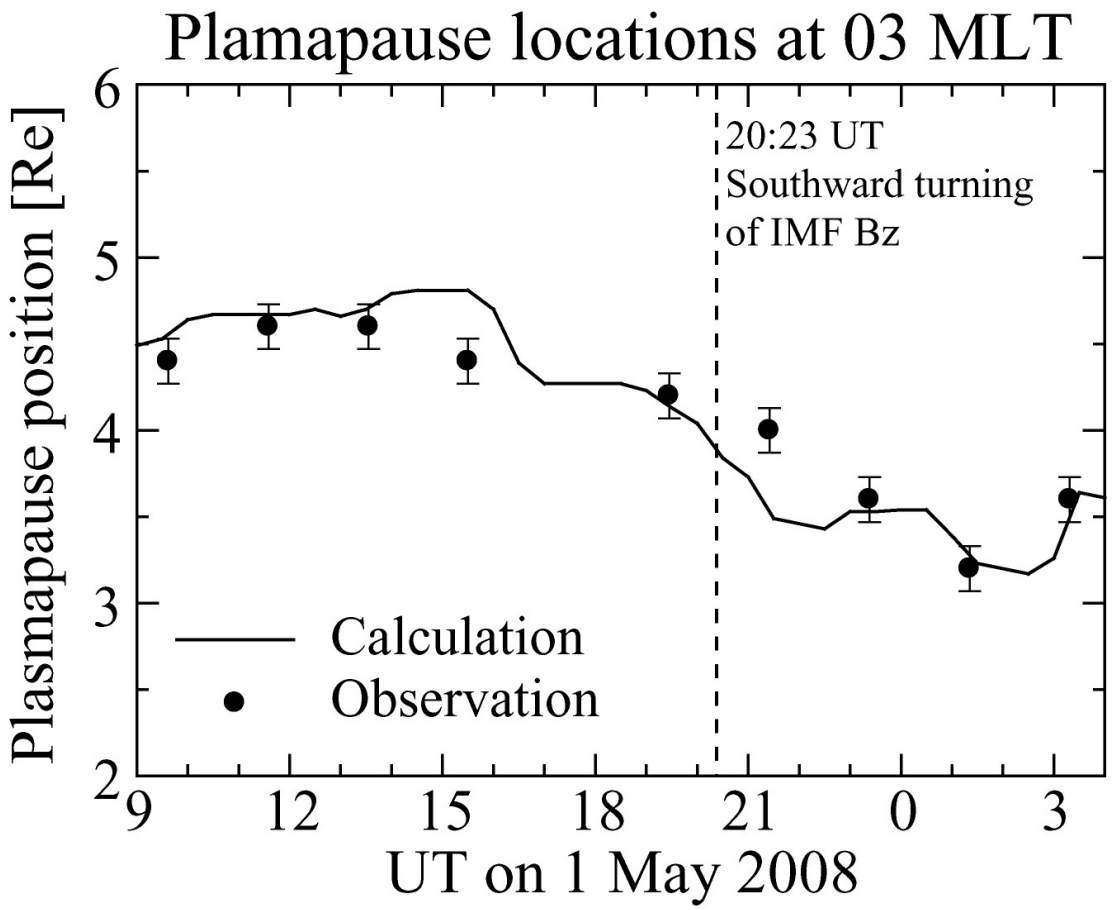

Figure 4.4: Temporal variation of the plasmapause locations in the geomagnetic equatorial plane at 3 MLT, obtained by the interchange simulations (solid line) and TEX observations (dots) on 1-2 May 2008. The arrival time of the southward IMF Bz is shown by the vertical dashed line.

4.3.2 Meridional distribution of the plasmapause observed by TEX

The temporal variation of the meridional distribution in the plasmasphere was investigated by analyzing the TEX images during the inward motion of the nightside plasmapause. In Figure 4.2a, the distribution of the EUV radiation seems to be aligned to the dipole magnetic field lines. On the other hand, as seen in Figure 4.2b and c, the EUV radiations in the nightside near the geomagnetic equatorial plane are relatively low in comparison with those in higher latitudes. These depletions of the EUV

radiations at low latitudes can be seen more clearly in Figure 4.5. Figure 4.5 shows the average counts along the dipole magnetic field lines of L = 2.2-2.6 at 03 MLT as a function of the magnetic latitude (MLAT). Each symbol represents the meridional profile of EUV radiation shown in Figure 4.2a, b, and c. In Figure 4.5, the EUV radiations clearly decrease below the magnetic latitude of 20 deg after the convection enhancement. Each average count below the MLAT of 20 deg is also presented as the horizontal line. After the convection enhancement, the EUV radiation at low latitudes decreased by ~30% during the inward motion of the nightside plasmapause.

If the helium ions were in motion relative to the sun, the He II emission line would be affected by Doppler shift in system moving with them. The wavelength λ after the shift can be expressed by $\lambda = \lambda_0 (1 - v/c)$, where λ_0 is the original wavelength (30.38 nm), v is the velocity of the He^+ relative to the Sun with a positive value towards the Sun, and c is the speed of light. The FWHM of the solar He II emission line is ~0.125 Å [Feldman and Behring, 1974]. For example, even if the helium ions were moving away from the Sun at v = 10 km/s (~6 Re/h), the He II emission line would shift to a wavelength 0.01 Å longer in the system and the intensity would decrease by only 1%. As the typical drift velocity in the plasmasphere is below 10 km/s, the decrease of the He II intensity due to Doppler shift is negligible.

Because the plasmasphere is optically thin for the He II radiation, the measured brightness is directly proportional to the He^+ column density along the line-of-sight. Therefore, the TEX instrument detected the depletion of the He^+ column density by ~30% near the equatorial plane during the geomagnetic disturbance.

This depletion of the equatorial column density can be caused by two possibilities: (1) the decrease of the number density inside the plasmasphere at L = 2-3 (i.e. the irregularity of the density inside the plasmasphere) and/or (2) the decrease of the column length through the plasmasphere along the line-of-sight (i.e. the irregularity of the plasmapause shape). The former structures are known as the density troughs inside the plasmasphere, called “inner-troughs” or “donkey-ears”, which were previously observed by in-situ measurements [e.g., *Horwitz et al.*, 1990; *Oya*, 1997; *Carpenter et al.*, 2000; *Fu et al.*, 2010]. The inner-trough is a structure with

significantly lower density (by a factor of 2-10) inside the plasmasphere compared to that in the surrounding region, as shown in Figure 1.6. *Carpenter et al.* [2000] conducted a statistical study of inner troughs using the data from the CRESS satellite that encircled the Earth in near-equatorial orbits. The properties of the inner density trough have been described by the occurrence rate (~13% of total passes), L shell range ($L < 4$ and $\Delta L = 0.5$-1.5), occurrence in MLT (most in the nighttime), duration (up to 10 hours or more), and extent in longitude (at least 20 deg) [*Carpenter et al.*, 2000].

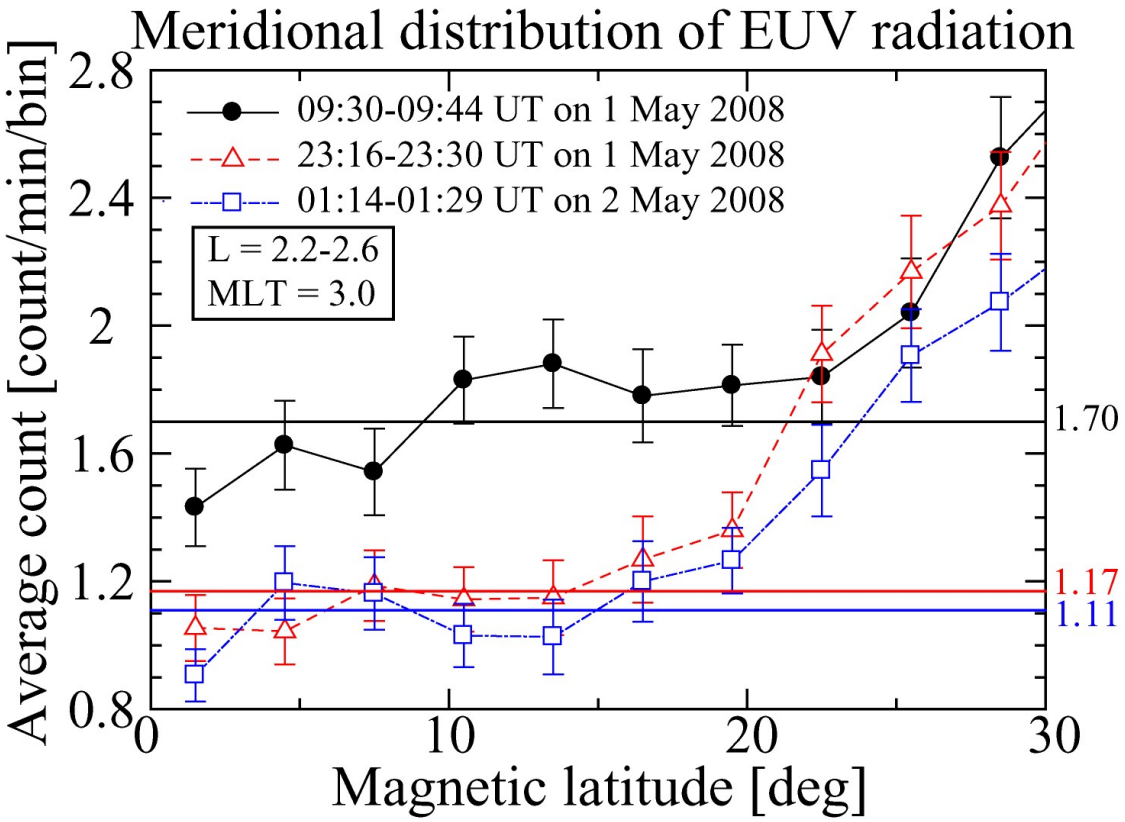

Figure 4.5: The meridional distribution of the TEX counts inside the plasmasphere on 1-2 May 2008 shown in Figure 4.2. The instrument counts averaged between L = 2.2 and 2.6 are plotted as a function of the geomagnetic latitude. The average counts in the magnetic latitude below 20 deg is also represented by each horizontal line.

Some other simultaneous observations, such as measurements of magnetospheric field line resonances by ground-based magnetometers or in-situ measurements by the spacecrafts, are needed in order to determine whether an inner trough was present at the nightside during the disturbance period on 1-2 May. The plasma mass density near the equatorial plane can be estimated by using the ground magnetometer data of magnetospheric ultralow frequency (ULF) waves that couple to standing field line eigenoscillations (field line resonances) [e.g., *Obayashi and Jacobs*, 1958; *Menk et al.*, 1999]. However, this technique cannot be used at the nightside because the resonances exist only in the dayside magnetosphere.

On the other hand, the in-situ measurement data of the THEMIS spacecrafts at the nightside plasmasphere on 1-2 May were available. The spacecraft potential measured by the Electric Field Instrument (EFI) can be used to estimate the electron number density surrounding the spacecraft in the plasmasphere [*Bonnell et al.*, 2008; Courtesy of *Y. Nishimura*]. Figure 4.6a shows the orbit of the THEMIS-C (P2) spacecraft on 2 May 2008. The THEMIS-C orbits the Earth on the geomagnetic equatorial plane with a period of ~2 days and a perigee of 1.4 Re at 07 MLT. The spacecraft passed the inner plasmasphere in the noon sector around 09:00 UT. If the equatorial depletion of He^+ column density in Figure 4.2b and c were caused by the same inner-trough, it should exist in the noon sector indicated by the red shaded area in Figure 4.6, assuming the pure corotation of the plasmasphere. Figure 4.6b presents the electron number density estimated from the spacecraft potential of THEMIS-C. No electron density depletions were identified by THEMIS-C in the red-shaded area. *Carpenter et al.* [2000] reported inner-troughs are generally large (ΔL = 0.5-1.5 and azimuthal extent of at least 20 deg) and last up to 10 hours or more. Therefore, this result does not agree with the possibility that an inner-trough caused the equatorial depletion of He^+ column density during the erosion on 1-2 May.

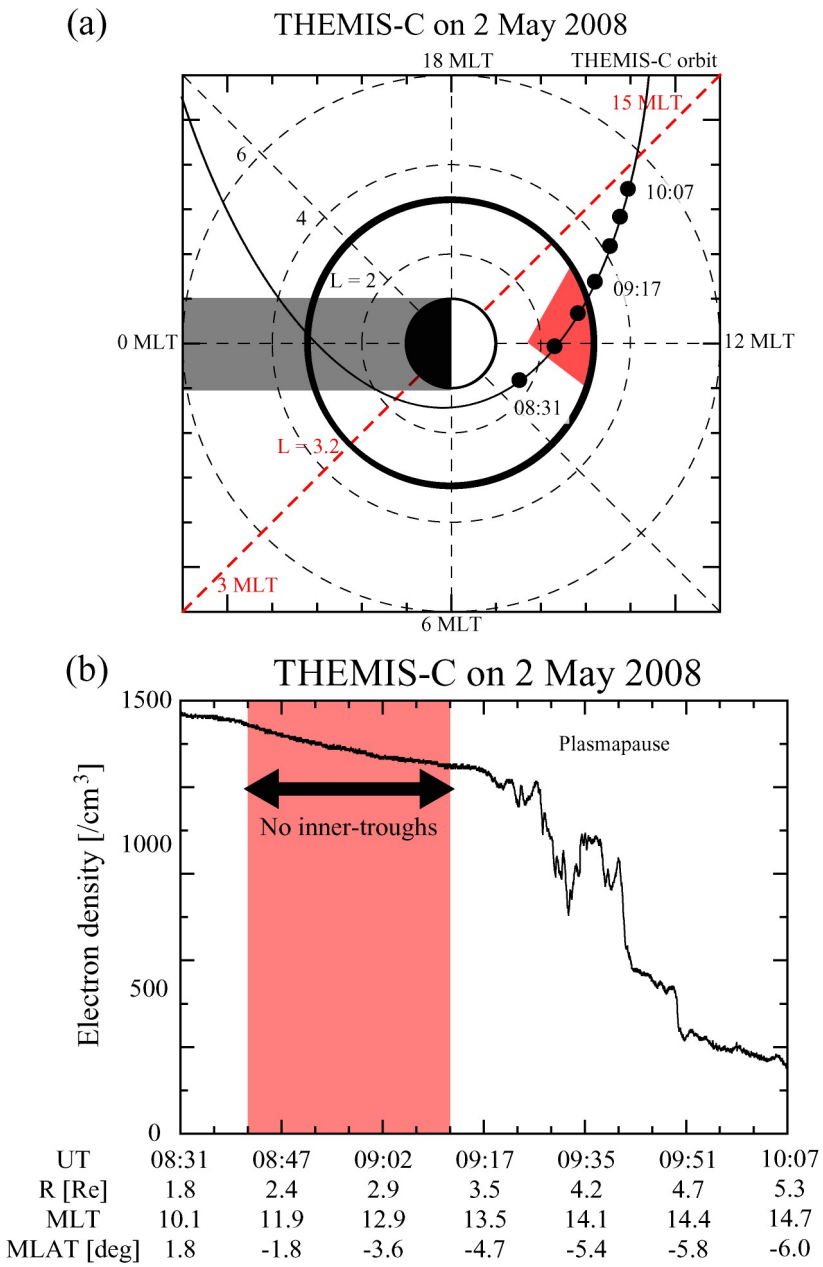

Figure 4.6: (a) The THEMIS-C (P2) orbit in the solar-magnetic (SM) coordinate on 2 May 2008, drawn in the same order as Figure 4.3. The positions of the spacecraft are presented by black dots every ~16 min from 08:31 to 10:07 UT. For reference, the L-shell of 3.2 is also shown as the solid black circle. The plasma elements in the red shade area were located at the post-midnight sector around 00:00 UT on 2 May. (b) The electron number density estimated from the spacecraft potential of THEMIS-C from 08:31 to 10:07 UT on 2 May.

The second possible cause of the depletion of the equatorial column density is the decrease of the column length through the plasmasphere along the line-of-sight at the low latitudes. For example, the flux tubes of L = 3.2 at 00 and 06 MLT were seen over that of L = 2.3 at 03 MLT from KAGUYA on 1-2 May 2008. Using the same method as the previous simulations in Chapter 3 (shown in Figure 3.11 and Figure 3.12), the intensities of the plasmasphere were briefly calculated for various cases of the plasmapause shapes. Figure 4.7 shows the comparisons of the observation results with the calculated images of the plasmasphere with various plasmapause shapes viewed from KAGUYA. The images are projected to the meridional plane at 03-15 MLT (only 03 MLT sectors are shown). The plasmapause shape is assumed to be aligned (a) to the dipole magnetic field line (L = 4.4), (b) to the ZPFS (Lz = 3.2) at low magnetic latitudes below 10 deg and to the dipole magnetic field line (L = 4.4) at high magnetic latitudes above 10 deg, (c) to the ZPFS (Lz = 3.2), and (d) to the dipole magnetic field line (L = 3.2). The calculated shapes of the plasmapause at 03 MLT does not agree with the observation results, especially calculation (b) with the TEX image at 23:16-23:30 on 1 May. This may be caused by the simple assumption of the same plasmapause shapes at all local times. Nevertheless, as indicated by the red circles in Figure 4.7, the equatorial depletion of the intensity was clearly seen in our calculation.

Figure 4.8 shows the meridional distribution of the intensity inside the plasmasphere shown in Figure 4.7. This figure is presented in the same manner as Figure 4.5. Comparing Figure 4.8 (a) with the others (b)-(d), the decrease of the equatorial column density was estimated to be ~20% when the equatorial plasmapause moves inward from L = 4.4 to 3.2. This value is in reasonable agreement with the observational result. Furthermore, the profiles of (b) and (c) seems to be comparable with the observational results of Figure 4.5 (b) and (c), respectively. Thus, these results can be interpreted that the nightside plasmapause at 00-06 MLT moved inward only at low latitudes during the disturbed period. In *Lemaire*'s [1974, 1985, 2001] interchange scenario for the formation of the plasmapause, the plasmapause develops first in the equatorial region, and subsequently at lower altitudes along the magnetic field lines

tangent to the ZPFS. On the other hand, the conventional theory can explain only the profiles of Figure 4.8 (a) and (d), because the effects of the gravitational and the centrifugal accelerations on the field-aligned plasma density distribution are not taken into account. Therefore, the meridional distribution of the plasmasphere viewed from the KAGUYA spacecraft agrees with the interchange scenario rather than the conventional theory for the plasmapause formation.

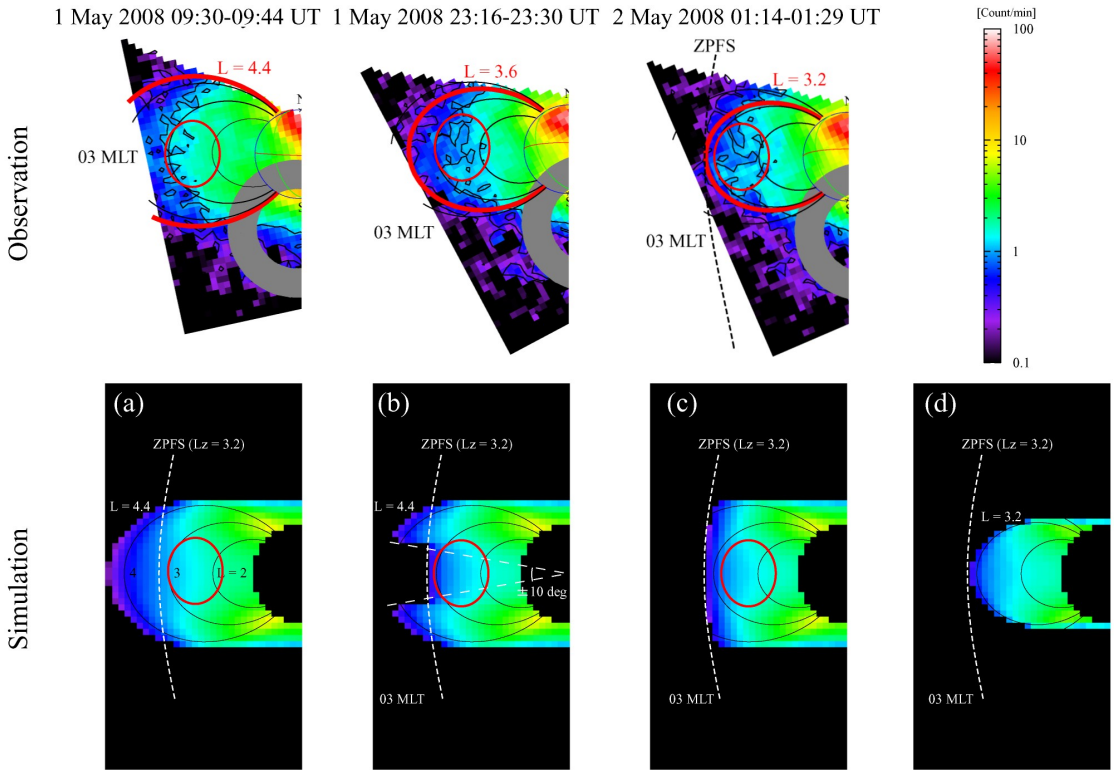

Figure 4.7: Comparison of the observed and calculated images of the plasmasphere. (Upper) The observed images of the plasmasphere during erosion on 1-2 May 2008. They are the same as those in Figure 4.2. (Bottom) Calculated images of the plasmasphere with various plasmapause shapes viewed from KAGUYA at 09 MLT on the geomagnetic equatorial plane. The plasmapause is assumed to be aligned to (a) the dipole magnetic field line (L = 4.4), (b) to the ZPFS (Lz = 3.2) at low magnetic latitudes below 10 deg and to the dipole magnetic field line (L = 4.4) at high magnetic latitudes above 10 deg, (c) to the ZPFS (Lz = 3.2), and (d) to the dipole magnetic field line (L = 3.2).

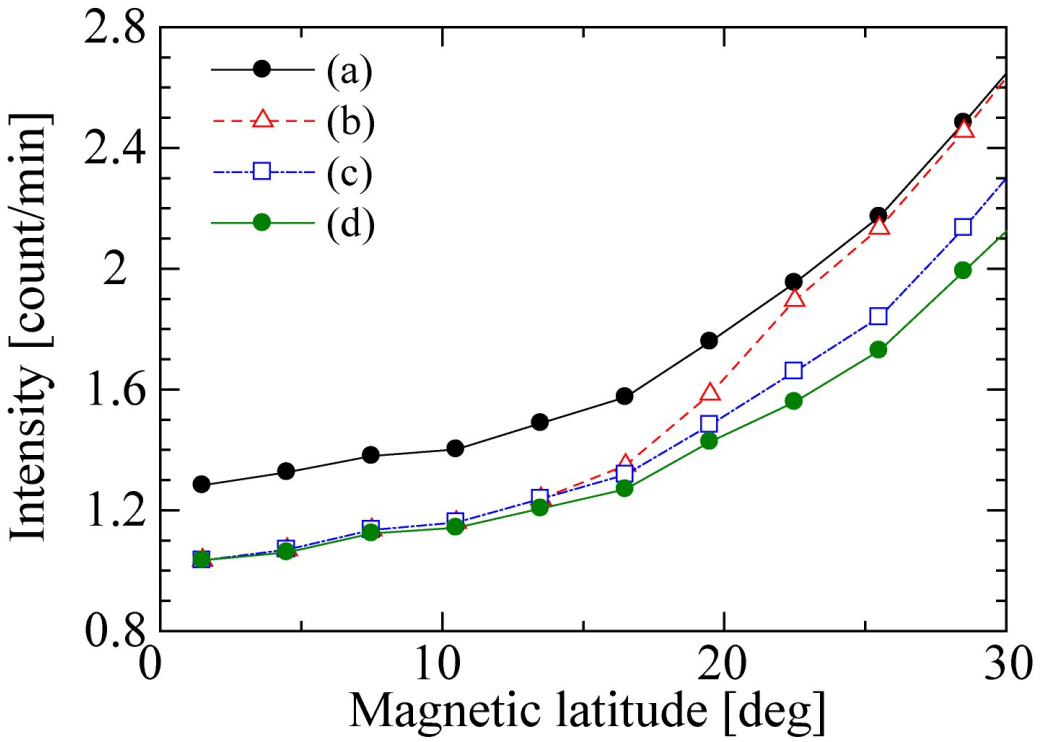

Figure 4.8: The meridional distribution of the intensity inside the plasmasphere shown in Figure 4.7. These profiles were estimated in the same manner as those in Figure 4.5.

The results presented in this study, however, do not prove that the interchange scenario is exclusive. Our simulation discussed above was performed on quite brief assumptions, such as the azimuthal (LT) symmetry. Indeed, the plasmapause shape in the calculated image of Figure 4.7 (b) is not comparable with the image obtained by TEX (Figure 4.4). In order to compare the images from observations and calculations more precisely, detailed numerical simulations for the plasmapause formation based on the interchange mechanism are required. Further investigation is necessary to understand the plasmapause formation. Nevertheless, the unique observation by the TEX instrument first detected the depletion of the equatorial column density by ~30% during the inward motion of the nightside plasmapause. This equatorial depletion cannot be explained only in terms of the traditional paradigm involving the interplay of the magnetospheric convection and the Earth's corotation. The results shown in this study will play a key role to determine the plasmapause formation mechanism.

4.4 Summary

The formation mechanism of the plasmapause was studied using the meridian images of the plasmasphere observed by the TEX instrument onboard the KAGUYA spacecraft. The sequential TEX images during the geomagnetic disturbance (Kp = 5) on 1-2 May 2008 were analyzed. The plasmapause positions at the post-midnight observed from the meridian perspective clearly agreed with those predicted by the dynamic simulations based on the interchange mechanism. Furthermore, after the convection enhancement, the He+ column density in the nightside plasmasphere decreased by ~30% only at the low latitudes (< 20 deg). The depletion of the column density may be caused by the decrease of the column length through the plasmasphere along the line-of-sight at the low latitudes during the geomagnetic disturbance. This result is consistent with the formation mechanism of the plasmapause based on the quasi-interchange instability. Although the interchange mechanism is not exclusive, this is the first study to present the plasmapause formation viewed from the meridian perspective.

5 Development of a multilayer mirror for Extreme Ultraviolet Imager onboard ISS-JEM

5.1 Introduction

Based on the heritage of the TEX instrument onboard the KAGUYA spacecraft, the next EUV imaging mission to observe the meridional distribution of the plasmasphere from low altitude is proposed and now in progress. The ISS-IMAP (Ionosphere, Mesosphere, upper Atmosphere, and Plasmasphere mapping) mission will make the imaging observation of the Earth's upper atmosphere from the Exposed Facility of Japanese Experiment Module on the International Space Station (EF of ISS-JEM). It is scheduled to start observation in 2012. The objective of this mission is to clarify the physical mechanism of the following three processes: (1) energy transport process by the atmospheric structures whose horizontal scale is 50-500km in the upper atmosphere (2) process of the plasma transport up to 20,000km altitude (3) effect of the upper atmosphere on the space-borne engineering system. To elucidate these processes, ISS-IMAP consists of two imaging instruments, Visible and Infrared Spectral Imager (VISI) and Extreme Ultra Violet Imager (EUVI). VISI will measure the airglow of 630nm (O), 650nm (OH), and 762nm (O_2) in the mesosphere and the ionosphere. Its field-of-view (FOV) is in the nadir direction. EUVI will measure the resonant scattering of 30.4nm (He^+) and 83.4nm (O^+) of the plasmasphere. Its FOV is in the backward limb direction.

The EUVI instrument consists of two telescopes, one is for He II radiation (30.4 nm) and the other is for O II radiation (83.4 nm). The design of each telescope is almost the same as that of the TEX instrument, which is a type of normal-incidence telescope with a multilayer mirror, a thin metal filter, and a MCP detector. The filter for

He II is composed of Al/C and that for O II is composed of In.

For the He II imaging from ISS, the contamination from geocoronal He I (58.4 nm) emission should be eliminated more effectively than the TEX instrument, because ISS orbits at a low altitude of ~350 km, inside the Earth's geocorona. The intensity of He II (30.4 nm) emission from the main body of the plasmasphere is ~5 Rayleigh [Nakamura et a., 2000], while the intensity of He I (58.4 nm) from the geocorona is ~400 Rayleigh [*Chackrabarti et al.*, 1983]. If completely the same optics as TEX is used in the EUVI instrument, the signal from the plasmasphere is comparable to the background from the geocorona. In order to solve this problem, it is necessary to develop a new multilayer coating having high reflectivity at 30.4 nm and low reflectivity at 58.4 nm. This specification is challenging because most materials have much higher single layer reflectivities at 58.4 nm than at 30.4 nm, e.g., the normal incidence reflectivity of Mo at 58.4 nm is 24%.

Periodic multilayer films have been developed in recent years for use as reflective coatings operating at normal incidence in the soft-x-ray and extreme ultraviolet (EUV) spectral regions. The coatings comprise a stack of nanometer-scale bilayers of optically dissimilar materials. The layers are arranged so that the reflections occurring at each interface in the stack achieve constructive interference over a range of photon wavelengths and incident angles. The response of the coating can be tuned by adjusting the multilayer period d (i.e., the bilayer thickness) according to Bragg's law $n\lambda = 2d\cos\theta$, where θ is the incident angle and n is the Bragg order. The number of periods and the relative thickness of each constituent material can also be adjusted in order to control the spectral response of the coating.

In space and planetary science, a number of imaging or spectroscopic observations in the EUV region have been and will be performed. High-reflectivity multilayer coatings for the He-II radiation at 30.4 nm have been required and developed for some of these applications [e.g., *Sandel et al.*, 2000; *Yoshikawa et al.*, 2008]. For the He II emission line, a multilayer mirror of Mo/Si has been usually and conventionally used, because it is highly stable. *Yoshikawa et al.* [2008] presented the reflectivity of the Mo/Si multilayer mirror installed in the TEX instrument is 18.8% at

30.4 nm.

In this work, a stable EUV mirror that has higher reflectivity at 30.4 nm with lower reflectivity at 58.4 nm than those of Mo/Si was developed for the plasmaspheric imaging from ISS. The sample mirrors of SiC/Mg and Y_2O_3/Al multilayer coatings are fabricated and evaluated. The performance and the temporal stability of each multilayer coating are reported in this chapter. Furthermore, the calibration results of the flight mirror for the EUVI instrument are also presented.

5.2 Observations from ISS

One of the targets of the EUVI instrument is the plasmaspheric filament. The TEX instrument onboard the KAGUYA spacecraft found the isolated flux tubes filled with dense plasma in quiet periods, as discussed in Chapter 3. However, due to the short duration of the TEX observation, only four events of the filaments were identified and the cause of the filament is still remaining open issue. In order to understand the physical process of the filament formation, especially relationship with the underlying ionosphere, we plan to observe the plasmasphere by the EUVI instrument onboard ISS. Investigation of filaments can play a key role to solve the longstanding issues such as plasmasphere refilling.

ISS orbits the Earth at an altitude of ~350 km with a period of 90 min. The EUVI instrument has the FOV of 14 deg × 14 deg, and it looks toward the backward limb direction of the ISS orbit. The inclination of the ISS orbit is 51 deg, so the EUVI can observe the magnetic flux tubes below L-value of ~4 at low altitudes. We simulated the plasmaspheric filaments viewed from ISS using the same assumptions as those of the previous calculations in Section 3.3.3 and 4.3.2. Figure 5.1 shows the calculated images of the plasmaspheric filament viewed from ISS during one revolution. Each case of the ISS orbit with the ascending node at 00, 03, 06, and 09 MLT is shown in Figure 5.1(a), (b), (c), and (d), respectively. The horizontal axis represents the azimuthal (longitudinal) angle of the FOV and the sunward direction corresponds to 0 deg. The vertical axis represents the elevation (latitudinal) angle of

the FOV and the geomagnetic equatorial plane corresponds to 0 deg. At the altitudes higher than 1000 km inside the flux tube at MLT = 21 and L = 3, the He^+ density was assumed to be higher than its neighbors by a factor of 5. As shown in Figure 5.1, the filament can be identified, especially in (a) and (d), because in this case it appears at the nightside and the intensity of its neighboring background is enough low thanks to the Earth's shadow. For example, in Figure 5.1(d) the intensity of the filament is higher than its neighbors by ~50%.

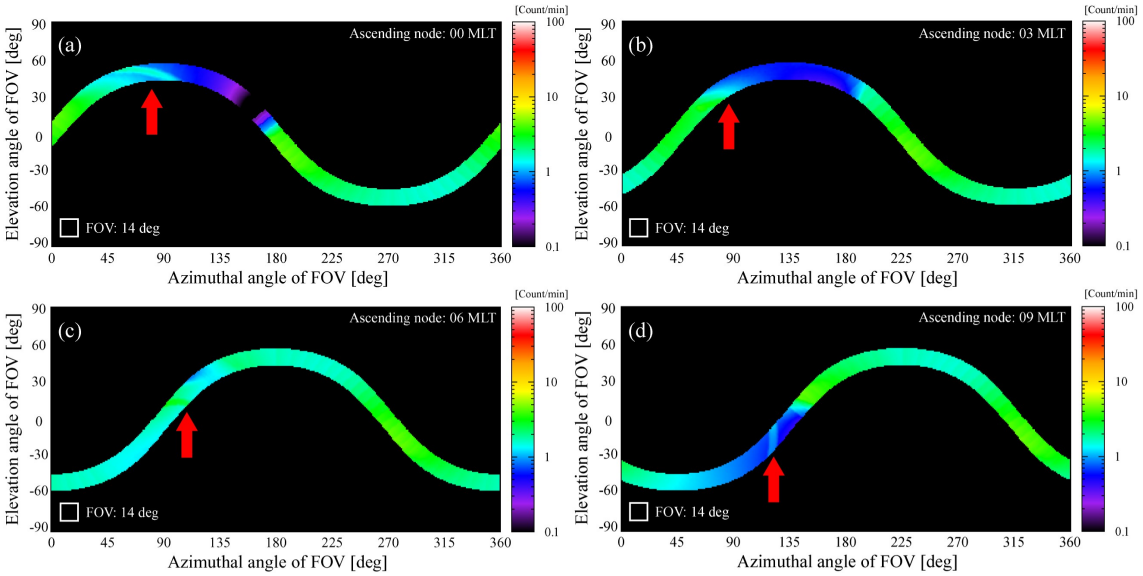

Figure 5.1: Calculated images of the plasmaspheric filament viewed from ISS. The horizontal axis represents the azimuthal (longitudinal) angle of the FOV (the sunward direction corresponding to 0 deg) and the vertical axis represents the elevation (latitudinal) angle of the FOV (the geomagnetic equatorial plane corresponding to 0 deg). Inside the isolated flux tube at L = 3 and MLT = 21 the He^+ density is assumed to be higher than its neighbors by a factor of 5.

On the other hand, Figure 5.2 shows calculated images of the filament at 09 MLT. The images were calculated in the same manner as Figure 5.1 except for the MLT of the filament. As shown in Figure 5.2, when the filament appears at the dayside, it is difficult to identify the filament structure due to its neighboring bright

backgrounds. Nevertheless, our calculation suggests that the EUVI instrument onboard ISS can observe the plasmaspheric filament in the nightside region and detect its corotating motion for several hours (during 2-3 revolutions of ISS).

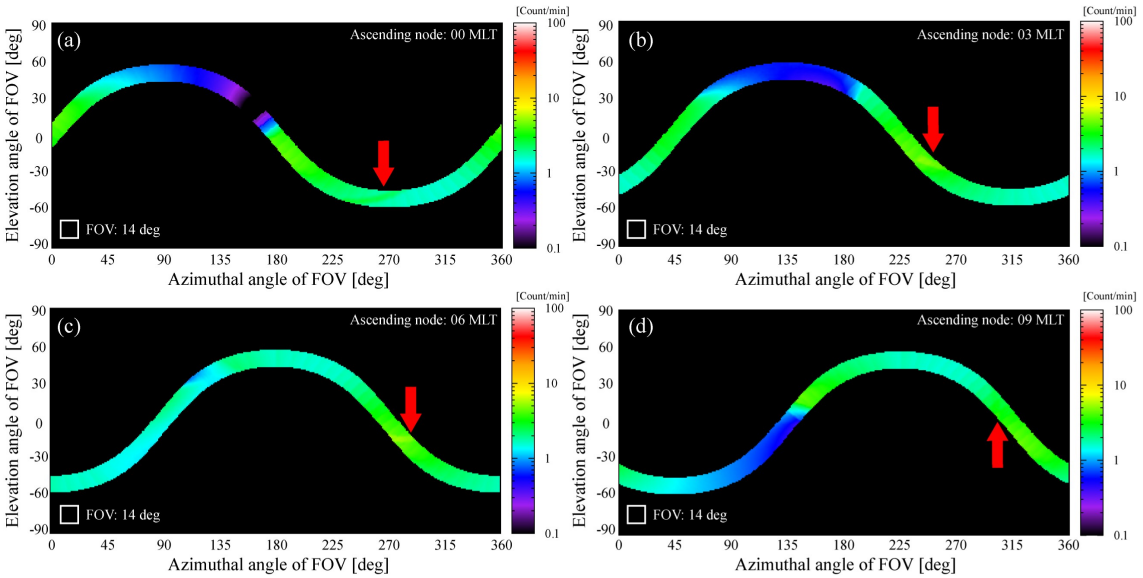

Figure 5.2: Calculated images of the plasmaspheric filament viewed from ISS. These images were calculated in the same manner as Figure 5.1 except for the MLT of the filament (09 MLT).

5.3 Designs and calculations

In order to decide the materials for the multilayer mirror installed in the EUVI instrument, the reflectivities of various multilayer coatings at 30.4 nm and 58.4 nm were calculated by using a conventional method [e.g. *Windt*, 1998]. We selected the materials which have been used for multilayer coatings in past studies and whose optical constants at 30.4 nm and 58.4 nm are available. Table 5.1 shows the materials and their optical constants (i.e., complex refractive indices n-ik) used in this study. Generally, multilayer coatings consisting of pairs with small k and large differences of n perform high reflectivities [e.g., *Hotta et al.*, 2002]. We calculated the reflectivities of all the combinations between upper six materials in Table 5.1 (Y_2O_3, Ir, Au, C, Pt,

and SiC) with small *n* values at 30.4, and lower six materials (Mo, MgF_2, Si, Al, Mg, and W) with large *n* values.

Table 5.1: Optical constants at 30.4 nm and 58.4 nm of various materials

	30.4 nm		58.4 nm	
	n	k	n	k
Y_2O_3	0.77	0.21	1.04	0.54
Ir	0.79	0.21	0.99	1.04
Au	0.80	0.31	1.06	0.84
C	0.81	0.085	0.65	0.75
Pt	0.83	0.21	0.79	0.92
SiC	0.85	0.045	0.35	0.48
Mo	0.91	0.43	0.61	0.75
MgF_2	0.92	0.15	1.1	0.82
Si	0.93	0.0090	0.64	0.051
Al	0.94	0.0082	0.71	0.0024
Mg	0.99	0.0025	0.86	0.045
W	1.04	0.18	0.50	0.87

Here, the calculated results can be classified into two groups, i.e. with and without Mg as an element. All of the multilayer coatings with Mg performed quite higher reflectivities at 30.4 nm than those without Mg. Figure 5.3 shows the calculated reflectivities of various multilayer coatings with Mg. They all had high reflectivity over 40% at 30.4 nm for the normal incidence of 10 deg, and the SiC/Mg multilayer coating performed the highest reflectivity in our calculation. *Yoshikawa et al.* [2005] first developed SiC/Mg multilayer coatings and their sample mirror achieved the reflectivity of 39.7% at the wavelength of 30.4 nm for the normal incidence of 10 deg. However, Mg is known to be highly reactive (e.g. Mg is usually found in nature in the form of an oxide, a carbonate, or a silicate, often in combination with calsium).

Questions remain about the long-term stability of Mg-based multilayer coatings [e.g., Soufli et al., 2005].

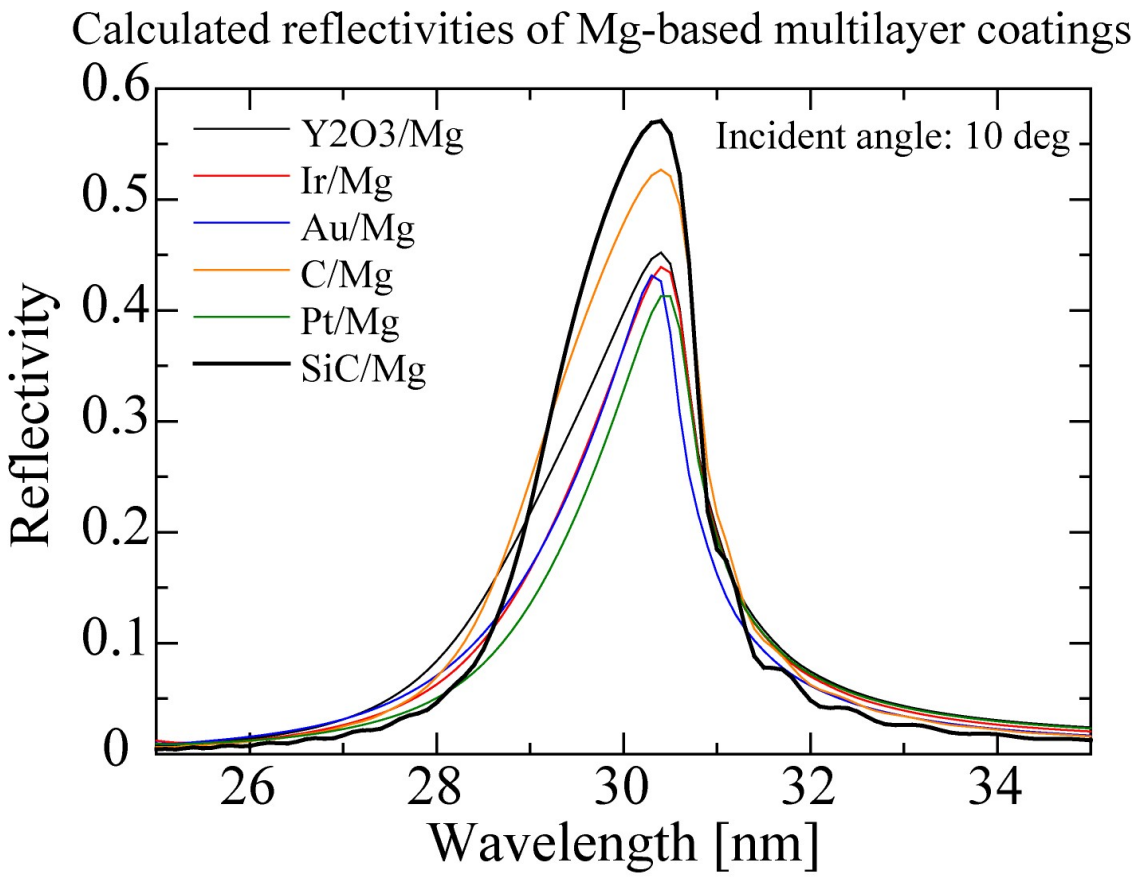

Figure 5.3: Calculated reflectivities of the various multilayer coatings with Mg at the normal incidence of 10 deg. The thickness of each element was optimized to normal incidence light (10 deg) at 30.4 nm.

On the other hand, the multilayer coatings without Mg that achieved higher reflectivities than 25% at 30.4 nm were listed in Table 5.2. In these multilayer combinations, Y_2O_3/Al achieved the largest ratio of reflectivities at 30.4 nm and 58.4 nm ($R_{30.4}/R_{58.4}$). Figure 5.4 shows the calculated reflectivies of SiC/Mg, Y_2O_3/Al, and Mo/Si multilayer coatings at the normal incidence of 10 deg. In the calculation both SiC/Mg and Y_2O_3/Al multilayer coatings achieve higher reflectivity at 30.4 nm and lower reflectivity at 58.4 nm than conventional Mo/Si. However, the performance of

Y_2O_3/Al multilayer coatings has not been experimentally evaluated yet. Therefore, in this study, sample coatings of SiC/Mg and Y_2O_3/Al were fabricated and the performance of each coating including the stability under various environments was evaluated. This is the first study to verify the performance of the Y_2O_3/Al multilayer coating.

Table 5.2: Parameters and calculated reflectivities at 30.4 nm and 58.4 nm of various multilayer coatings without Mg

Materials	Number of periods (N)	Multilayer period (d) [nm]	Thickness ratio (Γ)	$R_{30.4}$	$R_{58.4}$	$R_{30.4}/R_{58.4}$
Y_2O_3/Si	40	17.0	0.25	0.276	0.0051	54
Y_2O_3/Al	**40**	**16.7**	**0.24**	**0.301**	**0.0030**	**100**
Ir/Si	40	16.9	0.24	0.263	0.057	5
Ir/Al	40	16.7	0.24	0.287	0.049	6
Au/Si	40	16.9	0.23	0.276	0.022	13
Au/Al	40	16.6	0.21	0.298	0.015	20
C/Si	40	17.1	0.33	0.279	0.077	4
C/Al	40	16.8	0.31	0.321	0.056	6
Pt/Al	40	16.6	0.23	0.261	0.042	6
SiC/Si	40	17	0.35	0.256	0.106	2
SiC/Al	40	16.8	0.36	0.314	0.077	4

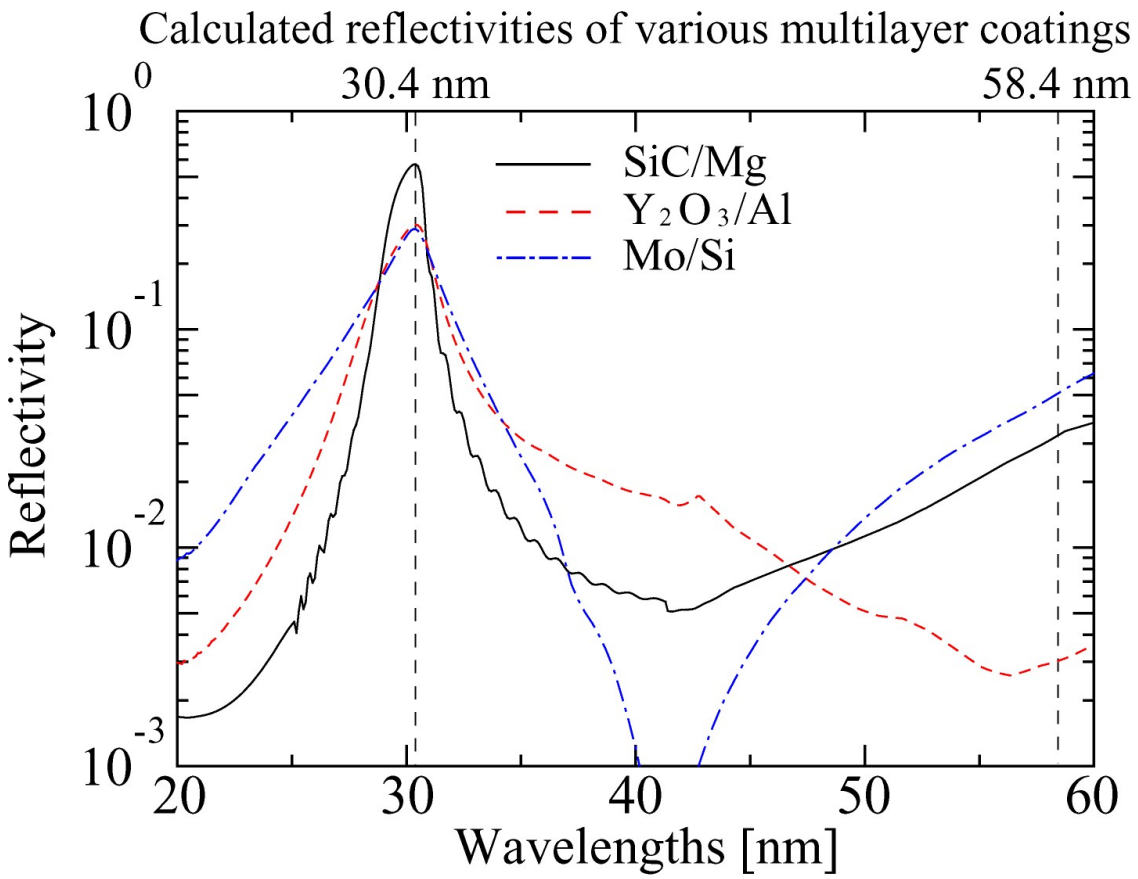

Figure 5.4: Calculated reflectivities of SiC/Mg, Y2O3/Al, and Mo/Si multilayer coatings by a conventional theoretical method. The mirrors are aimed for normal incidence of 10 deg.

The designs of the samples are listed in Table 5.3. The SiC/Mg sample mirror consists of periodic 40 pairs of SiC and Mg on a flat Si plane deposited by an ion-beam sputtering system. The SiC/Mg sample was aimed for grazing angle reflection (27 deg). We also fabricated two samples which were periodic 20 pairs of Y_2O_3 deposited by RF magnetron sputtering and Al deposited by DC magnetron sputtering. Sample 1 is aimed at normal incidence reflection (10 deg). Sample 2 is for grazing angle reflection (22 deg). We evaluated the multilayer period (d) in each sample with an x-ray diffractometer by measuring the small angle diffraction pattern (not shown). All the sample coatings were manufactured by the NTT-AT Company.

Table 5.3: Design parameters of SiC/Mg and Y_2O_3/Al multilayer coatings

Multilayer coating	Multilayer period (d) [nm]	Thickness ratio (Y_2O_3 / d)	Number of periods	Incident angle of peak reflectivity [deg]
SiC/Mg	18.1	0.30	40	27
Y2O3/Al (1)	17.1	0.33	20	10
Y2O3/Al (2)	18.2	0.24	20	22

5.4 Mesurements

Figure 5.5 shows the calibration setup of the EUV facility. The calibration system for EUV measurements consists of a windowless RF excited flow lamp filled with source gases and connected to a JOVIN YVON LHT30 30-cm scanning monochromator. Using an atomic source with the monochromator provides radiation limited only by the line widths of spectral lines from the light source. The use of gases such as helium and argon enables us to calibrate mirrors at various wavelengths in the 25-120 nm spectral range. The radiations at 30.4 nm (He II) and 58.4 nm (He I) are available from helium gas discharge. In the vacuum chamber, the mirror is set on a manipulator with three orthogonal axes of translation and a single axis of rotation aligned perpendicularly to the incident beam. The incident and reflected beams are detected by a photon detector consisting 5 microchannel plates (MCPs) and a resistive anode encoder (RAE). The reflectivity can be measured at the incident angle of more than 5 deg due to configuration constraint in our facility. Hereafter we discuss the reflectivities at 30.4 nm and 58.4 nm versus incident angle measured from the normal incidence.

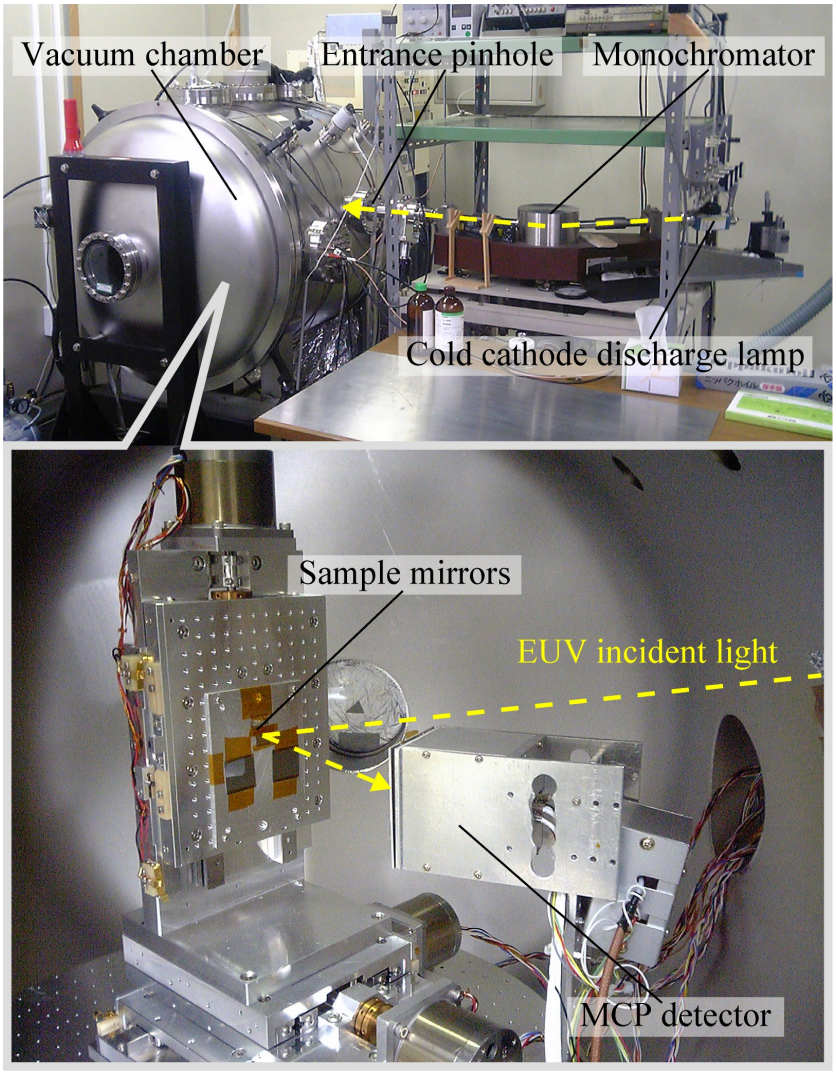

Figure 5.5: The calibration setup of the EUV facility. A cold discharge lamp is used as an EUV light source and the target line is selected by a monochromator. The selected light is collimated by pinhole at the entrance to the main vacuum chamber. An assembly of 5 microchannel plates (MCPs) and a resistive anode encoder (RAE) is used as an EUV detector.

5.5 Results and discussion

5.5.1 SiC/Mg multilayer coating

The sample of SiC/Mg multilayer coating was kept under atmosphere and vacuum alternately to identify the aging and to find its dependence on the

environments. Table 5.4 shows the environment during each period. For example, from the 1st to the 2nd measurement the sample was kept in the vacuum chamber where the pressure was under 10^{-4} Pa.

Table 5.4: Environment during each period

Order	Days after 1st measurement	Environment
1st	0	N_2 purge
		Vacuum
2nd	18	
		N_2 purge
3rd	95	
		Vacuum
4th	117	
		Vacuum
5th	529	
		N_2 purge
6th	565	

The reflectivity of the sample coating was measured for 6 times, and the results are shown in Figure 5.6 and Figure 5.7. Figure 5.6 shows the reflectivities of the SiC/Mg coating at 30.4 nm as a function of the incident angle. The calculated reflectivity is also represented as a dashed curve. Figure 5.7 summarizes the temporal variation of the reflectivity at the incident angle of 27 deg shown in Figure 5.6. The white circle represents the calculated reflectivity, and the black dots represent the measured reflectivities. During the shaded period the sample was kept in vacuum, and during the other period the sample was kept in dry N_2 purge.

As shown in Figure 5.6 and Figure 5.7, the reflectivity of the sample changes dramatically in atmosphere (between the 2nd and 3rd measurement) and gradually even

under vacuum (between 3rd and 5th measurement). On the other hand, the incident angle of the peak reflectivity did not change throughout all the measurements, as shown in Figure 5.6. These results indicate that the elements of the multilayer became opaque or clear without any change in thickness of the multilayer period. Indeed, Mg is known to be highly reactive (e.g. Mg is usually found in nature in the form of an oxide, a carbonate, or a silicate, often in combination with calsium). The nature of this aging, however, seems complicated because the tendency of aging-effect was not constant. This experimental result suggests that further investigation is necessary for practical use of the SiC/Mg multilayer coatings.

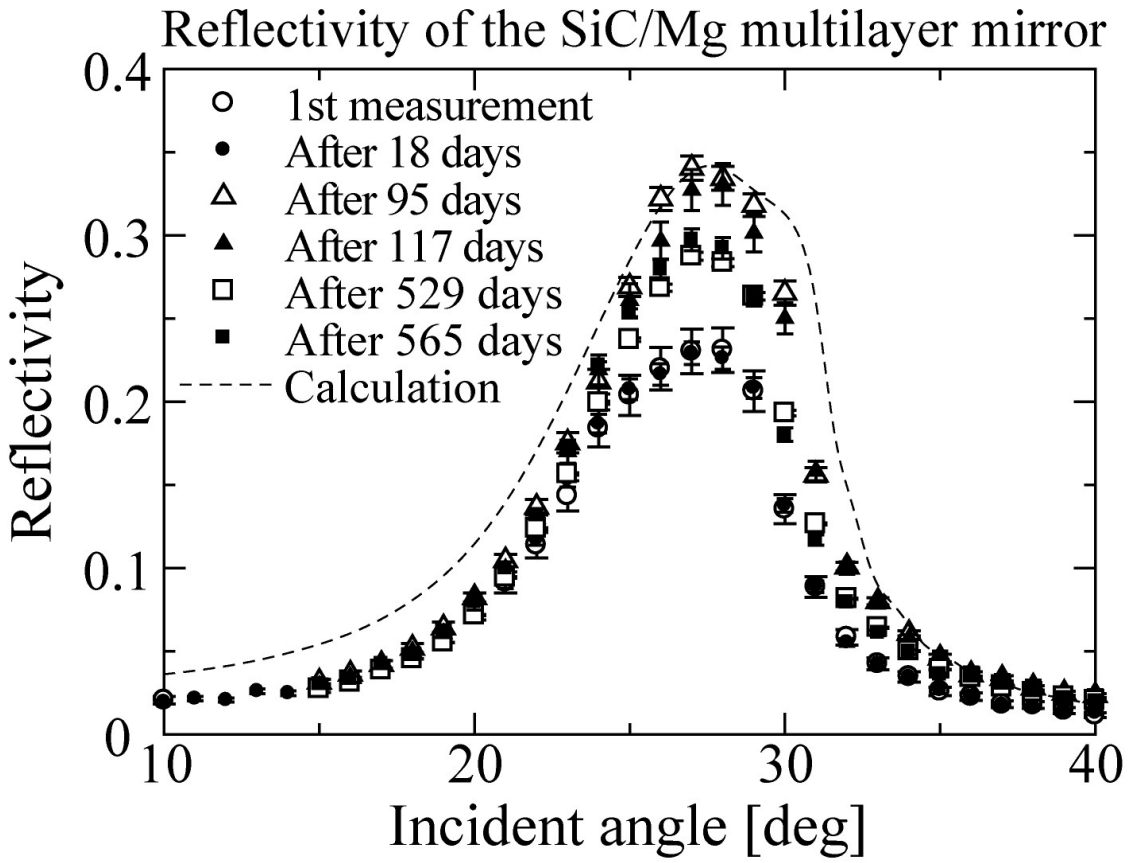

Figure 5.6: Reflectivities of the SiC/Mg multilayer mirror at 30.4 nm. The dashed line represents the calculated reflectivity. The storage environment during each period is shown in Figure 5.9.

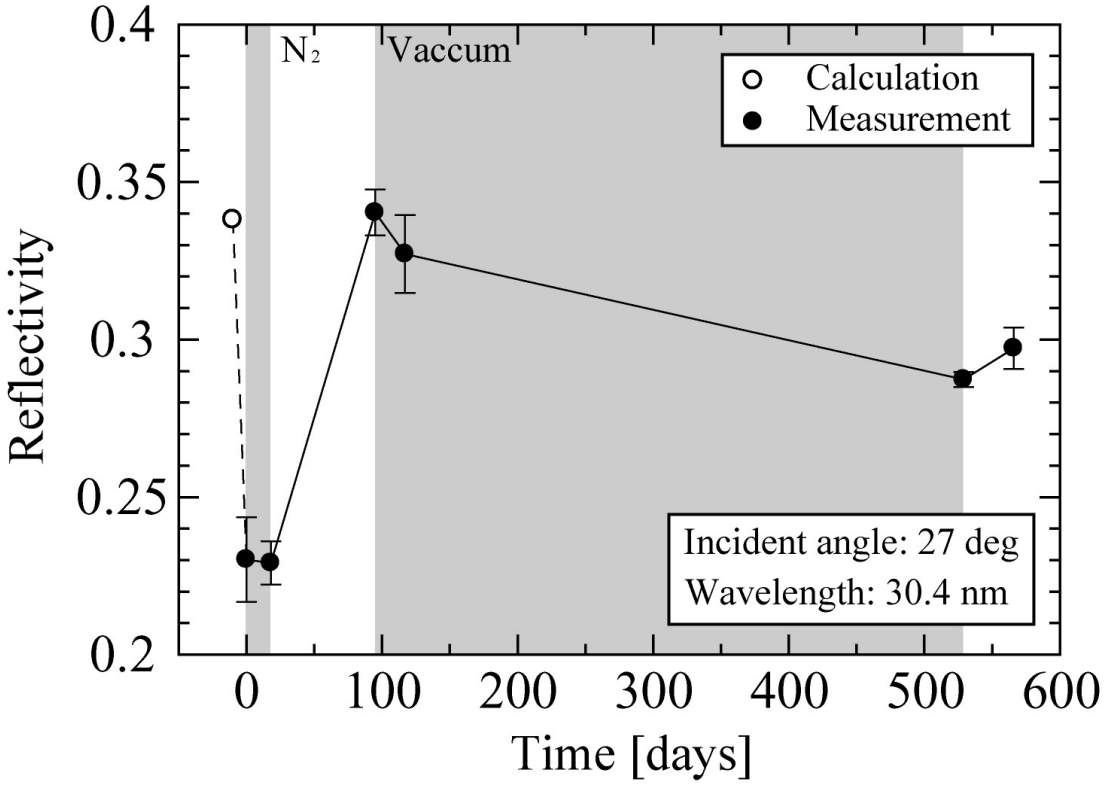

Figure 5.7: Peak reflectivity measured as a function of time for the SiC/Mg multilayer coating. The white circle shows the calculated reflectivity, and black dots represent the measured reflectivities. The wavelength was 30.4 nm and incident angle was 27 deg at the measurement.

5.5.2 Y_2O_3/Al multilayer coating

We measured the reflectivities of sample 1 at 30.4 nm and 58.4 nm as a function of incident angle from the normal incidence. The result is shown in Figure 5.8. The dots and triangles represent the measured reflectivities at 30.4 nm and 58.4 nm, respectively. The calculated reflectivity at 30.4 nm is also shown. At normal incidence of 10 deg, the reflectivity of sample 1 was 24.9% at 30.4 nm and 1.3% at 58.4 nm. The result shows that our multilayer coating consisting of 20 pairs of Y_2O_3 and Al has higher reflectivity at 30.4 nm and significantly lower reflectivity at 58.4 nm than the conventional coatings such as Mo/Si.

Figure 5.9 shows the reflectivity of sample 2 at 30.4 nm as a function of

incident angle. The reflectivity was measured just after its fabrication. In order to investigate the temporal stability of Y_2O_3/Al multilayer coatings, we kept sample 2 under vacuum, dry N_2 purge, and normal atmosphere. We have measured the peak reflectivity of sample 2 at 30.4 nm over a time span of about 3 months, and the result is shown in Figure 5.10. It is clear that there are no changes in the reflectivity. This result indicates that the EUV performance of the Y_2O_3/Al multilayer coating is quite stable over a period of at least 3 months independently of the environment, and there is no evidence to suggest that further changes in performance will occur over time.

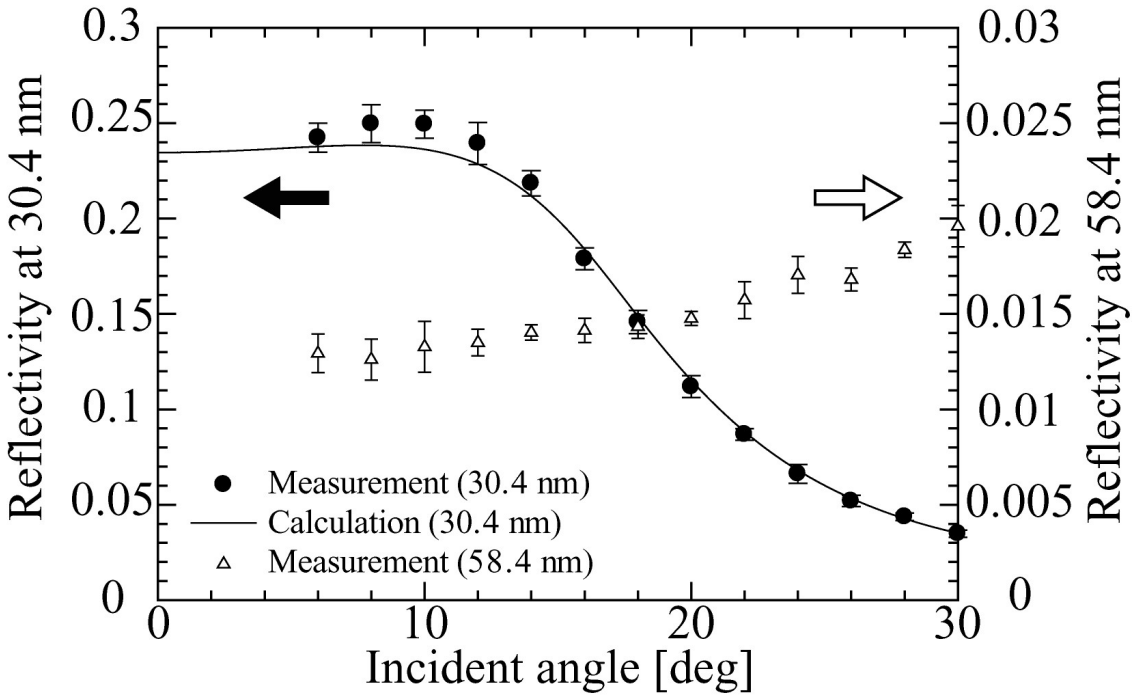

Figure 5.8: Reflectivities at 30.4 nm and 58.4 nm of a Y_2O_3/Al multilayer coating (sample 1). The calculated reflectivity at 30.4 nm is also shown.

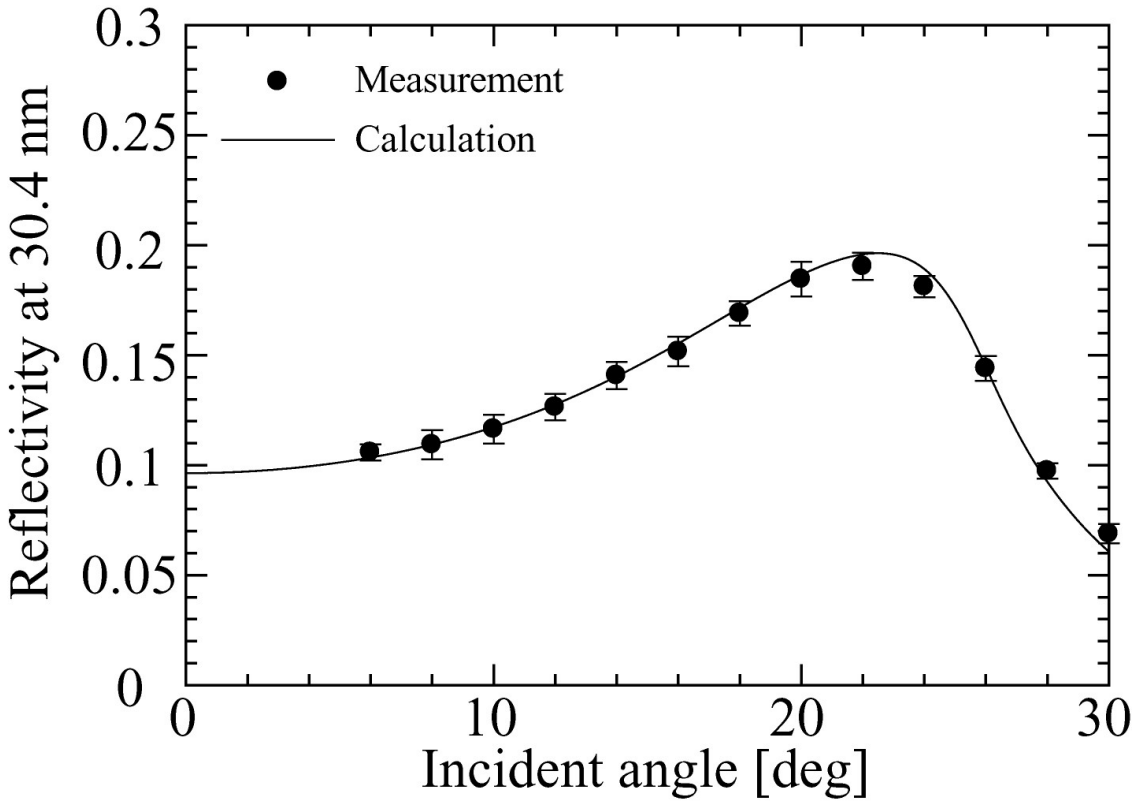

Figure 5.9: Reflectivity at 30.4 nm of a Y_2O_3/Al multilayer coating (sample 2), measured just after the fabrication. The calculated reflectivity is also shown.

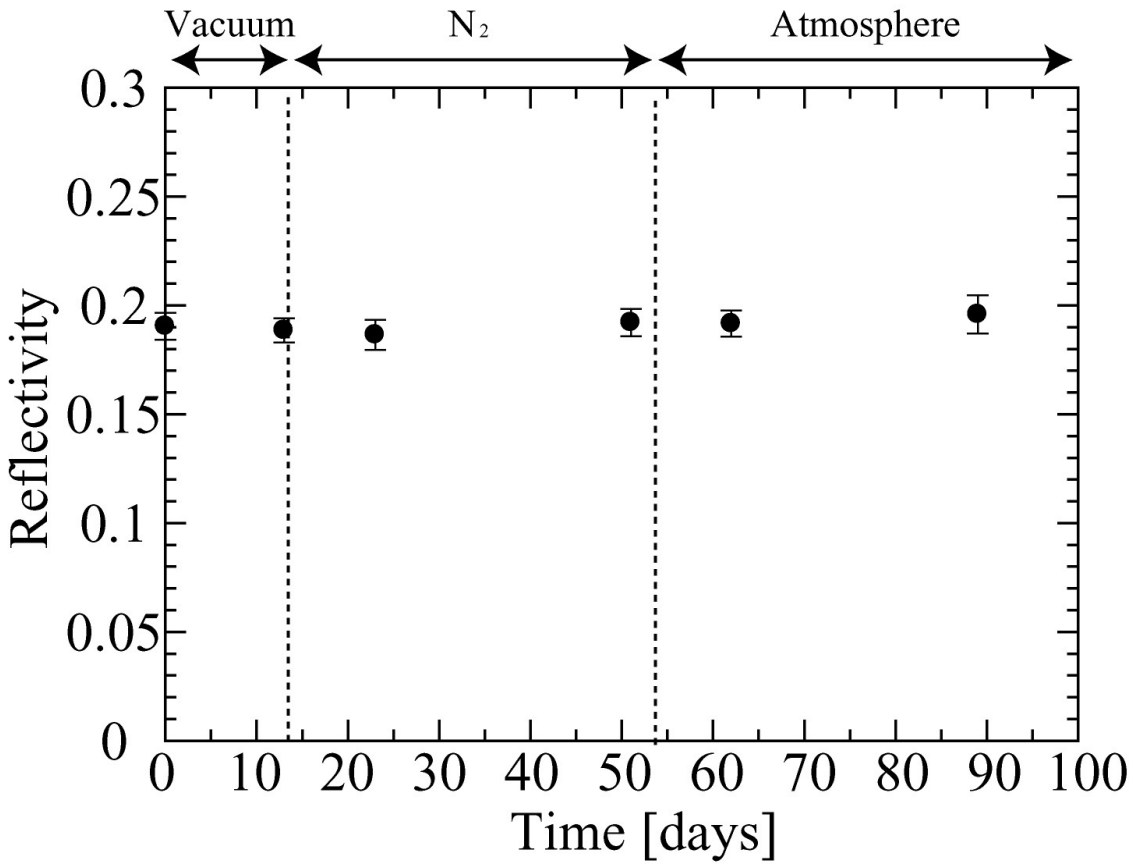

Figure 5.10: Peak reflectivity measured as a function of time for a Y_2O_3/Al multilayer coating (sample 2). The wavelength was 30.4 nm and incident angle was 22 deg at the measurement.

5.5.3 Calibration of the flight mirror for the EUVI instrument

The experimental results in Section 5.5.1 and 5.5.2 suggest that Y_2O_3/Al multilayer coatings are preferable and can be applied for the optics of the Extreme Ultraviolet Imager (EUVI) onboard ISS. Therefore, the flight mirror for the EUVI instrument was fabricated and calibrated.

Figure 5.11 shows a schematic diagram of the EUVI instrument, whose design is almost same as that of the TEX instrument onboard the KAGUYA spacecraft shown in Figure 2.2. The mirror substrate is made of Zerodur, and the mirror has a focal

length of 166 mm, a diameter of 120 mm, and a spherical shape to reduce aberration. A photograph of the flight mirror is shown in Figure 5.12. The design of the flight mirror substrate is almost the same as that of the TEX instrument. The mirror surface is coated by the Y_2O_3/Al multilayer. The number of periods are 20 and the multilayer period (d) is 17.0 nm (Y_2O_3 thickness of 5.1 nm and Al thickness of 11.9 nm). These parameters are set to aim at the normal incidence of 10 deg, and the same as that of Sample 1 described above. The Y_2O_3 layers were deposited by RF magnetron sputtering and the Al layers were deposited by DC magnetron sputtering. The NTT-AT Company manufactured the coating of the mirror.

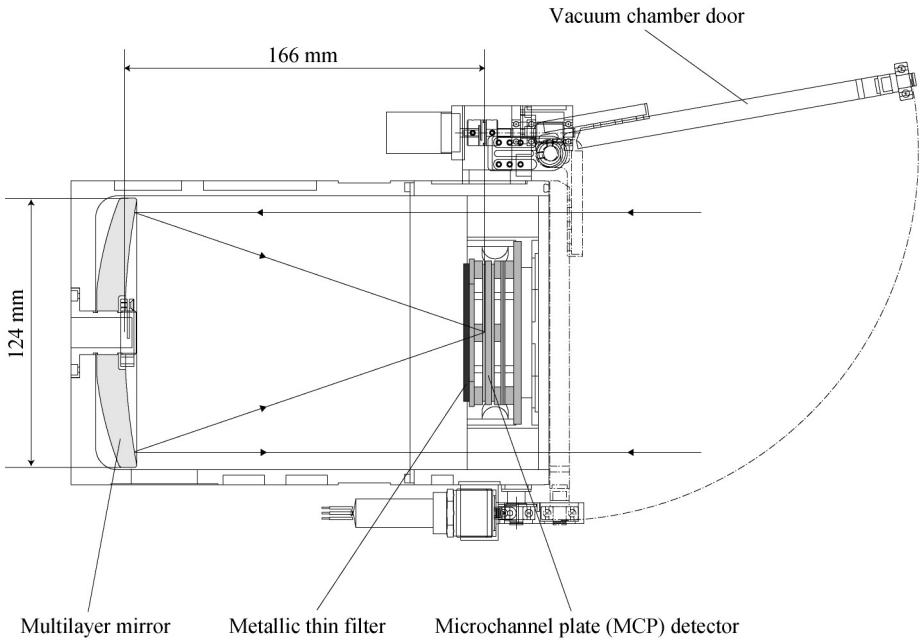

Figure 5.11: A schematic diagram of the Extreme Ultraviolet Imager (EUVI) instrument onboard ISS. Main optical components are a multilayer mirror, a metallic thin filter, and a MCP detector. The design of the EUVI instrument is almost the same as that of the TEX instrument onboard the KAGUYA spacecraft (shown in Figure 2.2).

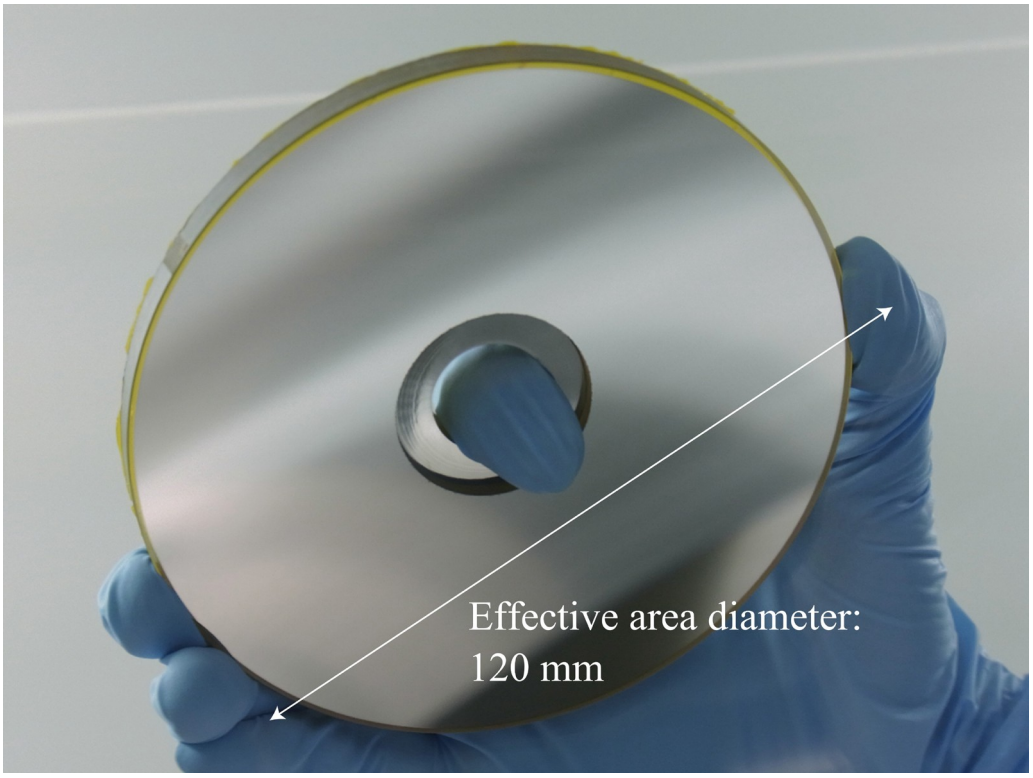

Figure 5.12: A photograph of the flight mirror for the EUVI instrument. The mirror has a focal length of 166 mm, a diameter of 120 mm, and a spherical shape to reduce aberration. The surface is coated by a 20-period of Y_2O_3/Al multilayer.

The reflectivity of the flight mirror was calibrated by using the same calibration system mentioned in Section 5.4. Figure 5.13 shows the reflectivities at 30.4 nm as a function of the incident angle to the mirror surface. The reflectivities were measured at three positions of 30 mm, 40 mm, and 50 mm from the center of the mirror. There are no dependences of the reflectivity on the position, and this result indicates the uniformity of the multilayer coating on the mirror surface.

Figure 5.14 gives the reflectivity of the flight mirror (at 40 mm from the center) as a function of wavelength. The incident angle was set to 10 deg in this measurement. The difference between the calculation and measurement at longer wavelengths may be due to the ambiguity of the optical parameter of Y_2O_3 in the EUV region. The reflectivities of 23.0% at 30.4 nm and of 1.7% at 58.4 nm were achieved. The ratio between the reflectivities at 30.4 nm and 58.4 nm ($R_{30.4}/R_{58.4}$) was 14, while

$R_{30.4}/R_{58.4}$ of the Mo/Si multilayer mirror installed in the TEX instrument was 2.

Using these results of calibrations, the signal-to-noise ratio (SNR) can be estimated. It was reported that the intensity of the plasmasphere mainbody at 30.4 nm is ~5 Rayleigh [*Nakamura et al.*, 2000] and that of the geocoronal contamination at 58.4 nm is ~400 Rayleigh in the dayside [*Chackrabarti et al.*, 1983]. Assuming the same transmittance of the filter and quantum efficiency of the MCP as those of TEX, the signal-to-noise ratio (SNR) of 16 can be achieved for 10-sec accumulation. This indicates that the EUVI instrument with the newly developed Y2O3/Al multilayer mirror is able to identify the plasmasphere through the geocorona from ISS.

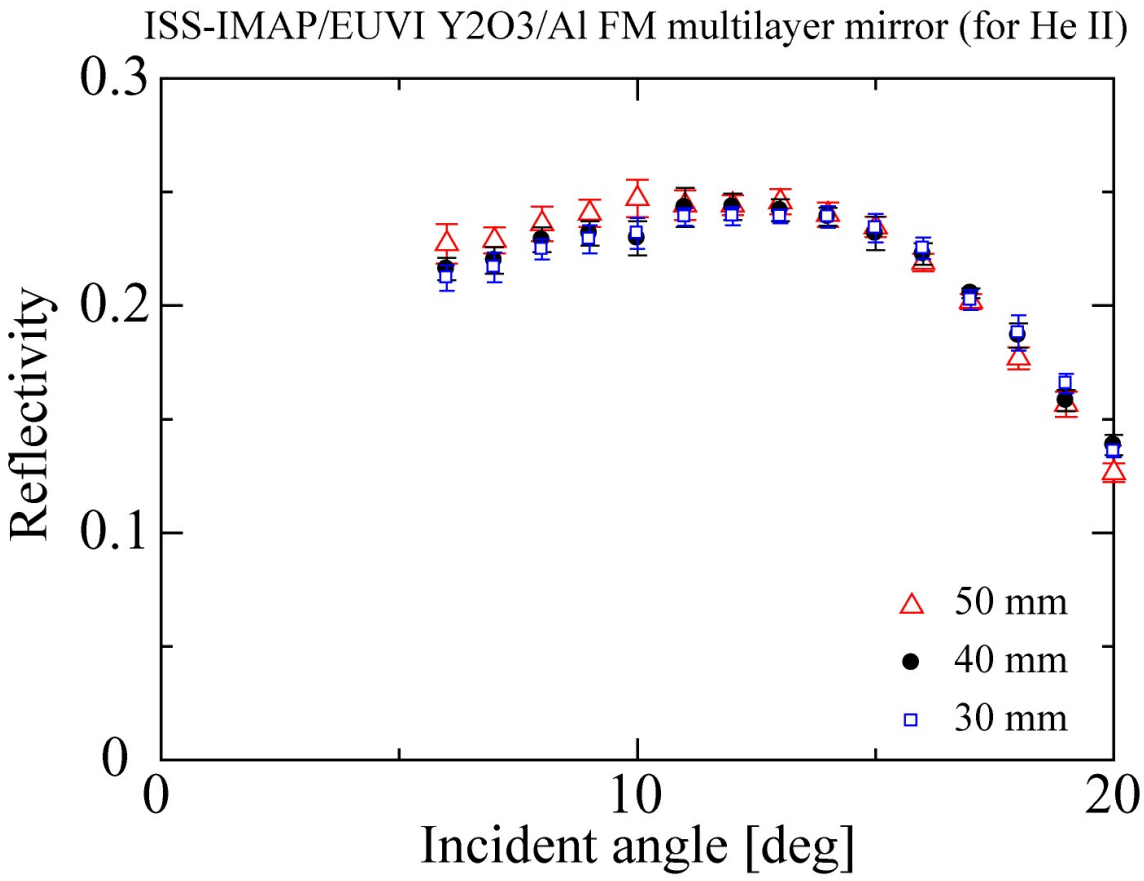

Figure 5.13: Dependence of the mirror reflectivity on incident angle to the mirror surface at 30.4 nm. The reflectivities were measured at positions of 30 mm, 40 mm, and 50 mm from the center.

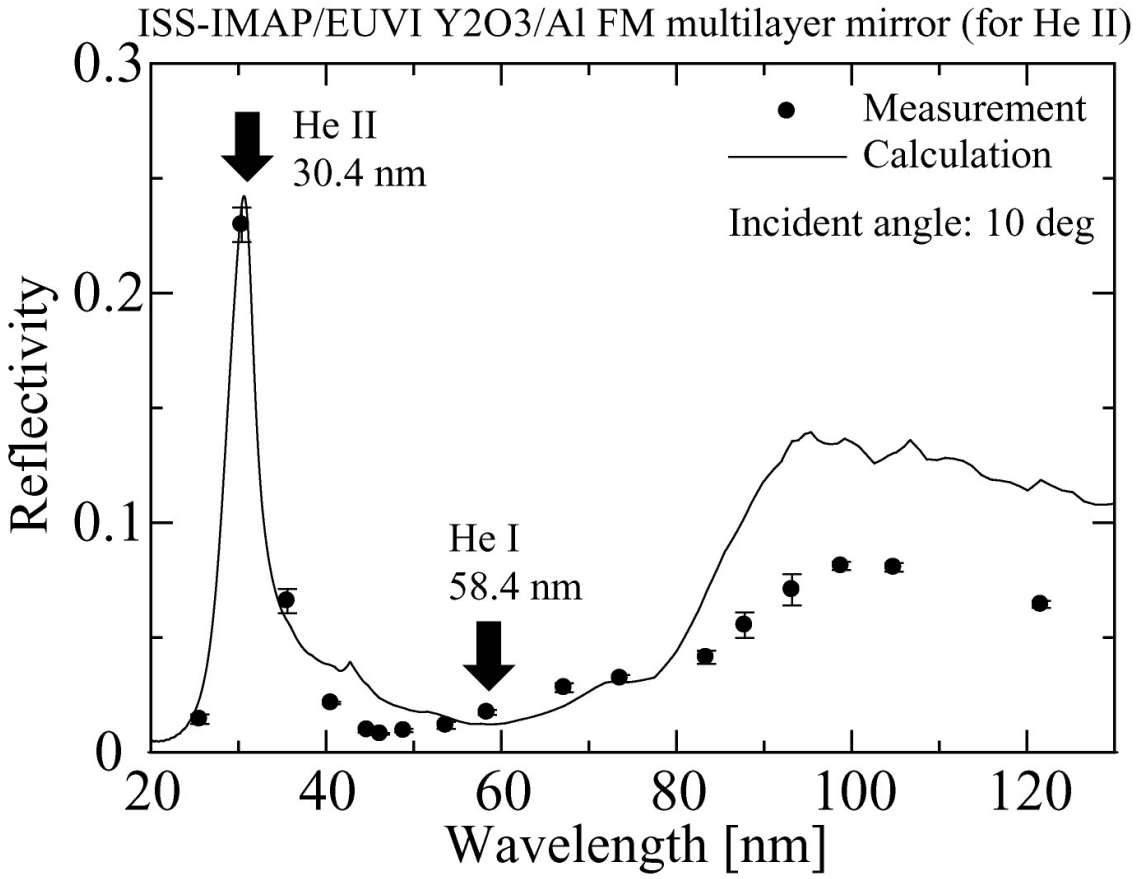

Figure 5.14: Reflectivity of the Y_2O_3/Al multilayer mirror used in the EUVI instrument. The reflectivities at 30.4 nm and at 58.4 nm are 23.0% and 1.7%, respectively. In this measurement the incident angle was set to 10 deg.

5.6 Summary

For the next plasmaspheric imaging from the International Space Station (ISS), new multilayer coatings having high reflectivity at 30.4 nm and low reflectivity at 58.4 nm were developed. The SiC/Mg multilayer coating for grazing angle reflection of 27 deg achieved quite high reflectivity of 34.0% at 30.4 nm. However, the SiC/Mg multilayer coating was unstable and the reflectivity changed under dry N2 purge and even under vacuum. On the other hand, the temporal stability of the Y2O3/Al multilayer coating was evaluated and found to be highly stable under vacuum, dry N_2 purge, and normal atmosphere. The Y_2O_3/Al multilayer coating designed for normal

incidence reflection had higher reflectivity (24.9%) at 30.4 nm and significantly lower reflectivity (1.3%) at 58.4 nm than the conventional coatings such as Mo/Si. These are the first result in the world to evaluate the performance of Y_2O_3/Al multilayer coatings.

Based on these results, the Y_2O_3/Al multilayer coating was selected to apply for the flight mirror of the Extreme Ultraviole Imager (EUVI) onboard ISS. The calibration of the flight mirror was performed, and the uniformity of the multilayer coating on the mirror surface was confirmed. Finally, the reflectivities of 23.0% at 30.4 nm and of 1.7% at 58.4 nm for the normal incident angle of 10 deg were achieved. This result indicates that the EUVI instrument with the newly developed Y_2O_3/Al multilayer mirror is able to identify the plasmasphere with a high SNR of 16.

6 Concluding remarks

The novel meridian images produced by the TEX instrument onboard the lunar orbiter KAGUYA has allowed us to explore several aspects of plasmaspheric dynamics from an entirely new perspective. Through the detailed analysis of the TEX images, we have obtained new results as well as confirmed and extended the results of previous experimental studies of the plasmasphere. In addition, for the instrumental point of view, the present study contributed to establishment of a remote sensing technique in the EUV range and its improvement for the future missions. This thesis details the in-orbit calibration of the Telescope of Extreme Ultraviolet onboard the KAGUYA spacecraft, the analysis on the plasmasphere images obtained from the meridian perspective, and the development of a new multilayer coated mirror for the next plasmasphere imaging from the International Space Station.

The performance of the TEX instrument after launch was evaluated using the in-orbit data obtained from February 2008 to May 2009. The imaging characteristics were calibrated using the images of bright EUV sources. The image scale of the field of view (FOV) is 0.068 Re/pix, and the total FOV equals to 8.7 Re × 8.7 Re. The average FWHM of PSF was 3.7 ± 1.1 pix, corresponding to 0.24 ± 0.07 Re. These values were considered in all the analysis of the TEX images demonstrated in this study. The long-term aging of the detector performance was also verified. The background throughout the mission was constantly low (~1.8 cps/cm^2) enough to achieve the signal-to-noise ratio (SNR) of 9 in the plasmaspheric imaging. No aging degradation was identified in the gain performance of the MCP detector throughout the mission. These results are important not only for the scientific products but for the future instruments.

The TEX instrument onboard the KAGUYA satellite obtained the first EUV images of the plasmasphere from the meridian perspective in March-June 2008. The inward motion of the plasmapause in the nightside during the disturbed period on 1-2 May 2008 was clearly observed by the TEX instrument. From the meridian view, the

inward velocity was estimated to be 0.2 Re/h on the assumption that the plasmapause was featureless and azimuthally smooth on the nightside. This result is consistent with that of the past study based on the IMAGE/EUV data. Furthermore, the corotation of the plasmasphere during the quiet period on 1-2 June 2008 was also identified in the sequential TEX images. By tracking a dipole-like density enhancement inside the plasmasphere, the corotation lag of the plasmasphere was estimated to be 2 hours/day, which agrees with the results from the recent studies derived from the IMAGE/EUV data. These agreements validate the observation of the plasmasphere by the TEX instrument from the meridian perspective.

A new striking feature of enhanced brightness (~30%) in the plasmasphere, called as a plasmaspheric filament, was found in the TEX image during a prolonged quiet period. The shape of the filament was extremely aligned to the dipole magnetic field line, and this suggests that the filaments are caused by isolated magnetic flux tubes filled with denser plasmas than their neighbors. We found 4 events of filaments in March-June 2008, and the occurrence rate was estimated to be about 1 event / 8days. All the filaments were observed during extremely quiet periods (Kp < 2). No dependence of their occurrence on local time was identified. These features of the filaments are consistent with those of the finger structure observed by IMAGE/EUV. Consequently, the result indicates that the finger structure seen in the EUV images should be the equatorial projection of isolated flux tubes filled with denser plasmas than its neighbors. Further investigation of filaments or fingers can play a key role to solve the longstanding issues of plasmasphere refilling.

The formation mechanism of the plasmapause was studied by analyzing the sequential TEX images of the erosion event during the geomagnetic disturbance (Kp = 5) on 1-2 May 2008. The temporal development of the plasmapause locations at the post-midnight (03 MLT) observed from the meridian perspective agreed with that predicted by the dynamic simulations based on the interchange mechanism. Furthermore, the He^+ column density in the nightside plasmasphere decreased by ~30% only at the low latitudes (< 20 deg) during the period of enhanced convection. On the other hand, no decreases of electron density (or inner troughs) in the plasmasphere were

identified in the simultaneous in-situ measurement by the THEMIS satellite. Therefore, this depletion of the column density suggests that the formation of the new plasmapause (i.e. the inward motion of the plasmapause) has occurred first near the equatorial region. This result is consistent with the scenario of the plasmapause formation based on the quasi-interchange instability. Although the interchange mechanism is not exclusive, this is the first study to present the plasmapause formation viewed from the meridian perspective. The experimental result in this study is novel and should be an important clue to completely understand the formation mechanism of the plasmapause.

For the next plasmaspheric imaging from the International Space Station (ISS), new multilayer coatings were developed in order to reduce the contamination of geocoronal He I (58.4 nm) emission. The SiC/Mg multilayer coating for grazing angle reflection of 27 deg achieved quite high reflectivity of 34.0% at 30.4 nm, but it was quite unstable and the reflectivity changed under dry N_2 purge and even under vacuum. On the other hand, the temporal stability of the Y_2O_3/Al multilayer coating was evaluated and found to be highly stable under vacuum, dry N2 purge, and normal atmosphere. The Y_2O_3/Al multilayer coating designed for normal incidence reflection had higher reflectivity (24.9%) at 30.4 nm and significantly lower reflectivity (1.3%) at 58.4 nm than the conventional coatings such as Mo/Si. These are the first result in the world to evaluate the performance of Y_2O_3/Al multilayer coatings. Then, based on these results, the flight mirror with Y_2O_3/Al multilayer coating was manufactured and calibrated for the ISS mission. It has the reflectivities of 23.0% at 30.4 nm and of 1.7% at 58.4 nm for the normal incident angle of 10 deg. This indicates that the instrument can produce the plasmaspheric images from ISS with a high SNR of 16.

Remaining problems and comments for future research

This study reveals that the finger structure seen in the IMAGE/EUV images are the equatorial projection of isolated flux tubes filled with denser plasmas than its neighbors. However, the physical process to form them is not understood yet. Further study of the plasmaspheric filaments (or fingers) should be performed. The future

imaging by the EUVI instrument onboard ISS will give us key information on the cause of filaments. As ISS orbits at an altitude of ~350 km with an orbital period of 90 min and an inclination of 52 deg, the EUVI instrument will have enough opportunity to observe the filaments. For example, the EUVI instrument can observe the extent of filaments at lower altitudes. Almost simultaneous observations of the ionosphere by Visible and Infrared Spectral Imager (VISI) onboard ISS will be also useful to compare the plasmaspheric and ionospheric features. The VISI instrument can observe the ionospheric density enhancements (or plasma blobs) by detecting OI 630 nm emission that comes from an altitude region of 220-300 km [e.g., *Pimenta et al.*, 2007]. These studies enable us to deduce the dominant initial conditions for the refilling process, such as plasma density, flow velocity, and temperature, and finally to determine the physical mechanism of the refilling.

As for the physical process of the plasmapause formation, further investigations are also necessary. In this study, using the novel images observed by the TEX instrument onboard the KAGUYA spacecraft, we have presented the experimental result that the nightside plasmapause moves inward first at the low latitudes during the disturbed period. However, the plasma detachment from the main-body of the plasmasphere has not been detected directly by imaging (IMAGE/EUV and KAGUYA/TEX) due to the instrumental limitations, such as sensitivity, temporal resolution, and FOV. Additional future observations, not only a high-resolution (~1 min) imaging with the sensitivity of at least ~2 cps/Rayleigh but also simultaneous in-situ measurements outside the plasmapause, are necessary to clarify this problem.

References

Adrian, M. L., D. L. Gallagher, and L. A. Avanov (2004), IMAGE EUV observation of radially bifurcated plasmaspheric features: First observations of a possible standing ULF waveform in the inner magnetosphere, *J. Atmos. Sol. Terr. Phys.*, *68*, 213-227.

Andre, N., and J. F. Lemaire (2006), Convective instabilities in the plasmasphere, *J. Geophys. Res.*, *109*, A01203, doi:10.1029/2003JA009974.

Blanc, M., and A. D. Richmond (1980), The ionospheric disturbance dynamo, *J. Geophys. Res.*, *85*, 1669-1686.

Bonnell, J. W., F. S. Mozer, G. T. Delory, A. J. Hull, R. E. Ergun, C. M. Cully, V. Angelopoulos, and P. R. Harvey (2008), The Electric Field Instrument (EFI) for THEMIS, *Space Sci. Rev.*, 141, 303-341.

Burch, J. L., S. B. Mende, D. G. Mitchell, T. E. Moore, C. J. Pollock, B. W. Reinisch, B. R. Sandel, S. A. Fuselier, D. L. Gallagher, J. L. Green, J. D. Perez, and P. H. Reiff (2001a), Views of Earth's magnetosphere with the IMAGE satellite, *Science*, *291*(5504), 619.

Burch, J. L., D. G. Mitchell, B. R. Sandel, P. C. Brandt, and M. Wüest (2001b), Global dynamics of the plasmasphere and ring current during magnetic storms, *Geophys. Res. Lett.*, *28*(6), 1159.

Burch, J. L., Goldstein, J., and B. R. Sandel (2004), Cause of plasmasphere corotating lag, *Geophys. Res. Lett.*, 31, L05802, doi:10.1029/2003GL019164.

Carpenter, D. L. (1963), Whistler evidence of a 'knee' in the magnetospheric ionization density profile, *J. Geophys. Res.*, *68*, 1,675.

Carpernter, D. L., and R. R. Anderson (1992), An ISEE/Whistler model of equatorial electron density in the magnetosphere, *J. Geophys. Res.*, *97*, 1097-1108.

Carpernter, D. L., R. R. Anderson, W. Calvert, and M. B. Moldwin (2000), CRESS observations of density cavities inside the plasmasphere, *J. Geophys. Res.*, *105*, 23323-23338.

Chakrabarti, S., F. Paresce, S. Bowyer, Y. T. Chiu, and A. Aikin (1982), Plasmaspheric helium ion distribution from satellite observations of He II 304 Å, *Geophys. Res. Lett.*, *9*, 151.

Chakrabarti, S., F. Paresce, S. Bowyer, and R. Kimble (1983), The extreme ultraviolet day airglow, J. *Geophys. Res.*, *88*(A6), 4898-4904.

Chappell, C. R., K. K. Harris, and G. W. Sharp (1970), A study of the influence of magnetic activity on the location of the plasmapause as measured by OGO 5, *J. Geophys. Res.*, *75*, 50.

Comfort, R. H. (1986), Plasmasphere thermal structure as measured by ISEE-1 and DE-1, *Adv. Space Res.*, *6*, 31-40.

Craven, P. D., Gallagher, D. L., and R. H. Comfort (1997), Relative concentration of He^+ in the inner magnetosphere as observed by the DE 1 retarding ion mass spectrometer, *J. Geophys. Res.*, *102*(A2), 2279-2290.

Darrouzet, F., D. L. Gallagher, N. André, D. L. Carpenter, I. Dandouras, P. M. E. Décréau, J. De Keyser, R. E. Denton, J. C. Foster, J. Goldstein, M. B. Moldwin, B. W. Reinisch, B. R. Sandel, and J. Tu (2009), Plasmaspheric density structures and dynamics: Properties observed by the CLUSTER and IMAGE missions, *Space Sci. Rev.*, *145*, 55-106.

Feldman, U., and W. E. Behling (1974), Solar coronal line profiles in the extreme-ultraviolet, *Astrophys. J., 189*, L45-L46.

Foster, J. C., P. J. Erickson, A. J. Coster, J. Goldstein, and F. J. Rich (2002), Ionospheric signatures of plasmaspheric tails, *Geophys. Res. Lett.*, *29*(13), 1623, doi:10.1029/2002GL015067.

Fu, H. S.. J. Tu, J. B. Cao, P. Song, B. W. Reinisch, D. L. Gallagher, and B. Yang (2010), IMAGE and DMSP observations of a density trough inside the plasmasphere, *J. Geophys. Res.*, *115*, A07227, doi:10.1029/2009JA015104.

Gallagher, D. L., M. L. Adrian, and M. W. Liemohn (2005), Origin and evolution of deep plasmaspheric notches, *J. Geophys. Res.*, *110*, A09201, doi:10.1029/2004JA010906.

Gallagher, D. L., and M. L. Adrian (2007), Two-dimensional drift velocities from the

IMAGE EUV plasmaspheric imager, *J. Atmos. Sol. Terr. Phys.*, *69*(3), 341-350.

Galvan, D. A., M. B. Moldwin, and B. R. Sandel (2008), Diurnal variation in plasmaspheric He^+ inferred from extreme ultraviolet images, *J. Geophys. Res.*, *113*, A09216, doi:10.1029/2007JA013013.

Galvan, D. A., M. B. Moldwin, B. R. Sandel, and G. Crowley (2010), On the causes of plasmaspheric rotation variability: IMAGE EUV observations, *J. Geophys. Res.*, *115*, A01214, doi:10.1029/2009JA014321.

Gold, T. (1959), Motions in the magnetosphere of the Earth, *J. Geophys. Res.*, *64*, 1219.

Goldstein, J., and B. R. Sandel (2005), The global pattern of evolution of plasmaspheric drainage plumes, in *Inner Magnetospheric Interactions: New Perspectives from Imaging*, ed. by J. L. Burch, M. Schulz, H. Spence. Geophysical Monograph Series, vol. 159 (American Geophysical Union, Washington, 2005), 1-22.

Goldstein, J., M. Spasojević, P. H. Reiff, B. R. Sandel, W. T. Forrester, S. L. Gallagher, and B. W. Reinisch (2003a), Identifying the plasmapause in IMAGE EUV data using IMAGE RPI in situ steep density gradients, *J. Geophys. Res.*, *108*(A4), 1147, doi:10.1029/2002JA009475.

Goldstein, J., B. R. Sandel, W. T. Forrester, and P. H. Reiff (2003b), IMF-driven plasmasphere erosion of 10 July 2000, *Geophys. Res. Lett.*, *30*(3), 1146, doi:10.1029/2002GL016478.

Goldstein, J., R. A. Wolf, B. R. Sandel, and P. H. Reiff (2004), Electric fields deduced from plasmapause motion in IMAGE EUV images, *Geophys. Res. Lett.*, 31(1), L01801, doi:10.1029/2003GL018797.

Goldstein, J., B. R. Sandel, W. T. Forrester, M. F. Thomsen, and M. R. Hairston (2005), Global plasmasphere evolution 22–23 April 2001, *J. Geophys. Res.*, *110*, A12218, doi:10.1029/2005JA011282.

Horwitz, J. L., R. H. Comfort, and C. R. Chappell (1990), A statistical characterization of plasmasphere density structure and boundary locations, *J. Geophys. Res.*, *95*, 2333-2343.

Hotta, Y., M. Furudate, M. Yamamoto, and M. Watanabe (2002), Design and fabrication of multilayer mirrors for He-II radiation, *Surf. Rev. Lett.*, *9*, 571-576.

Johnson, C. Y., J. M. Young, and J. C. Holmes (1971), Magnetoglow-A new geophysical resource, *Science*, *171*, 379.

Joseph, C. L., V. Argabright, J. Abraham, D. Dieball, S. Franka, M. Styonavich, C. Van Houten, T. Danks, and B. Woodgate (1994), Test and evaluation of the space telescope imaging spectrograph (STIS) engineering model units of the MAMA detectors, *Proc. SPIE*, *2282*, 116-125.

Kagitani, M., M. Taguchi, A. Yamazaki, I. Yoshikawa, G. Murakami, K. Yoshioka, S. Kameda, F. Ezawa, T. Toyota, and S. Okano (2009), First optical observation of the Moon's sodium exosphere from the lunar orbiter SELENE (Kaguya), *Earth Planets Space*, *61*, 1025-1029.

Kato, M., S. Sasaki, K. Tanaka, Y. Iijima, and Y. Takizawa (2008), The Japanese lunar mission SELENE: Science goals and present status, *Adv. Space Res.*, *42*, 294-300.

Kunieda, H., K. Yamashita, T. Yamazaki, K. Ikeda, K. Misaki, Y. Takizawa, M. Nakamura, I. Yoshikawa, and A. Yamaguchi (1996), EUV Observation with Normal Incidence Multilayer Telescopes, in *Astrophysics in the extreme ultraviolet. Proc. of colloquium no. 152 of the International Astromical Union* (S. Bowyer and R. F. Malina Eds.), Kluwer Academic Publ., 21.

Lemaire, J. (1974), The 'Roche-limit' of ionospheric plasma and the formation of the plasmapause, *Planet. Space Sci.*, *22*, 757.

Lemaire, J. (1985), Frontiers of the Plasmasphere (Theoretical Aspects), Universite´ Catholique de Louvain, Faculte´ des Sciences, Louvain-la-Neuve, ISBN 2-87077-310-2.

Lemaire, J. (2001), The formation of the light-ion trough and peeling off the plasmasphere, *J. Atmos. Sol. Terr. Phys.*, *63*, 1285-1291.

Lemaire, J. F., and L. Kowalkowski (1981), The role of plasma interchange motion for the formation of a plasmapause, *Planet. Space Sci.*, *29*(4), 469-478.

Lemaire, J. F., and K. I. Gringauz (1998), The Earth's plasmasphere, Cambridge Univ.

Press, New York.

Lemaire, J. F., and V. Pierrard (2008), Comparison between two theoretical mechanisms for the formation of the plasmapause and relevant observations, *Geomagn. Aeron.*, *48*(5), 553-570.

Meier, R. R., A. C. Nicholas, J. M. Picone, D. J. Melenez-Alvira, G. I. Ganguli, M. A. Reynolds, and E. C. Roelof (1998), Inversion of plasmaspheric EUV remote sensing data from the STP 72-1 satellite, *J. Geophys. Res.*, *103*, 17,505.

Menk, F. W., D. Orr, M. A. Clilverd, A. J. Smith, C. L. Waters, D. K. Milling, and B. J. Fraser (1999), Monitoring spatial and temporal variations in the dayside plasmasphere using geomagnetic field line resonances, *J. Geophys. Res.*, *104*(A9), 19955-19969.

Moldwin, M. B., L. Downward, H. K. Rassoul, R. Amin, and R. R. Anderson (2002), A new model of the location of the plasmapause: CRRES results, *J. Geophys. Res.*, *107*(A11), 1339, doi:10.1029/2001JA009211.

Murakami, G., M. Hirai, and I. Yoshikawa (2007), The plasmapause response to the southward turning of the IMF derived from sequential EUV images, *J. Geophys. Res.*, *112*, A06217, doi:10.1029/2006JA012174.

Nakamura, M., I. Yoshikawa, A. Yamazaki, K. Shiomi, Y. Takizawa, M. Hirahara, K. Yamashita, Y. Saito, and W. Miyake (2000), Terrestrial plasmaspheric imaging by an extreme ultraviolet scanner on Planet-B, *Geophys. Res. Lett.*, *27*(2), 141.

Newcomb, W. A. (1961), Convective instability induced by gravity in a plasma with a frozen-in magnetic field, *Phys. Fluids*, *4*, 391-396.

Nishida, A. (1966), Formation of plasmapause, or magnetospheric plasma knee, by the combined action of magnetospheric convection and plasma escape from the tail, *J. Geophys. Res.*, *71*, 5,669.

Obana, Y., G. Murakami, I. Yoshikawa, I. R. Mann, P. J. Chi, and M. B. Moldwin (2010), Conjunction study of plasmapause location using ground-based magnetometers, IMAGE-EUV, and KAGUYA-TEX data, *J. Geophys. Res.*, *115*, A06208, doi:10.1029/2009JA014704.

Obayashi, T., and J. A. Jacobs (1958), Geomagnetic pulsations and the Earth's outer

atmosphere, *Geophys. J. R. Astron. Soc., 1*(1), 53-63.

Ogawa, T., and T. Tohmatsu (1971), Sounding rocket observation of helium 304- and 584-Å glow, *J. Geophys. Res.*, *76*, 6136.

Oya, H. (1997), Dynamical variation of plasmasphere revealed by PWS data onboard the Akebono (EXOS-D) satellite, *J. Geomagn. Geoelectr*, *49*, S159-S178.

Park. J., C. Stolle, H. Lühr, M. Rother, S. Y. Su, K. W. Min, and J. J. Lee (2008), Magnetic signatures and conjugate features of low-altitude plasma blobs as observed by the CHAMP satellite, *J. Geophys. Res.*, *113*, A09313, doi:10.1029/2008JA013211.

Paresce, F., C. S. Bowyer, and S. Kumar (1974), On the distribution of He^+ in the plasmasphere from observations of resonantly scattered He II 304 Å radiation, *J. Geophys. Res.*, *79*, 174.

Pierrard, V., and J. F. Lemaire (2001), Exospheric model of the plasmasphere, *J. Atmos. Sol. Terr. Phys.*, *63*, 1261-1265.

Pierrard, V., and J. F. Lemaire (2004), Development of shoulders and plumes in the frame of the interchange instability mechanism for plasmapause formation, *Geophys. Res. Lett.*, *31*, L05809.

Pierrard, V., and J. Cabrera (2005), Comparisons between EUV/IMAGE observations and numerical simulations of the plasmapause formation, *Ann. Geophys.*, *23*(7), 2635-2646.

Pierrard, V., and J. Cabrera (2006), Dynamical simulations of plasmapause deformations, *Space Sci. Rev.*, *122*, 119-126.

Pierrard, V., and L. Stegan (2008), A three-dimensional dynamic kinetic model of the plasmasphere, *J. Geophys. Res.*, *113*, A10209, doi:10.1029/2008JA013060.

Pierrard, V., G. V. Khazanov, J. Cabrera, and J. F. Lemaire (2008), Influence of the convection electric field models on predicted plasmapause positions during magnetic storms, *J. Geophys. Res.*, *113*, A08212, doi:10.1029/2007JA012612.

Pierrard, V., J. Goldstein, N. André, V. K. Jordanova, G. A. Kotova, J. F. Lemaire, M. W. Liemohn, and H. Matsui (2009), Recent progress in physics-based models of the plasmasphere, *Space Sci. Rev.*, *145*, 193-229.

Pimenta, A. A., Y. Sahai, J. A. Bittencourt, and F. J. Rich (2007), Ionospheric plasma blobs observed by OI 630 nm all-sky imaging in the Brazilian tropical sector during the major geomagnetic storm of April 6-7, 2000, *Geophys. Res. Lett.*, *34*, L02820, doi:10.1029/2006GL028529.

Sandel, B. R., A. L. Broadfoot, C. C. Curtis, R. A. King, T. C. Stone, R. H. Hill, J. Chen, O. H. W. Siegmund, R. Raffanti, D. D. Allred, R. S. Turley, and D. L. Gallagher (2000), The Extreme Ultraviolet Imager investigation for the IMAGE mission, *Space Sci. Rev.*, *91*, 197.

Sandel, B. R., R. A. King, W. T. Forrester, D. L. Gallagher, A. L. Broadfoot, and C. C. Curtis (2001), Initial results from the IMAGE Extreme Ultraviolet Imager, *Geophys. Res. Lett.*, *28*, 1,439.

Sandel, B. R., J. Goldstein, D. L. Gallagher, and M. Spasojević (2003), Extreme Ultraviolet Imager observations of the structure and dynamics of the plasmasphere, *Space Sci. Rev.*, *109*, 25.

Sasaki, S., Y. Iijima, K. Tanaka, M. Kato, M. Hashimoto, H. Mizutani, and Y. Takizawa (2003), The SELENE mission: Goals and status, *Adv. Space Res.*, *31*, 2335-2340.

Soufli, R., D. L. Windt, J. C. Robinson, S. L. Baker, E. Spiller, F. J. Dollar, A. L. Aquila, E. M. Gullikson, B. Kjornrattanawanich, J. F. Seely, and L. Golub (2005), Development and testing of EUV multilayer coatings for the atmospheric imaging assembly instrument aboard the Solar Dynamics Observatory, *Proc. SPIE*, *5901*, 173-183.

Spasojević, M., J. Goldstein, D. L. Carpenter, U. S. Inan, B. R. Sandel, M. B. Moldwin, and B. W. Reinisch (2003), Global response of the plasmasphere to a geomagnetic disturbance, *J. Geophys. Res.*, *108*(A9), 1340, doi:10.1029/2003JA009987.

Taguchi, M., T. Sakanoi, S. Okano, M. Kagitani, M. Kikuchi, M. Ejiri, I. Yoshikawa, A. Yamazaki, G. Murakami, K. Yoshioka, S. Kameda, W. Miyake, M. Nakamura, and K. Shiokawa (2009), The Upper Atmosphere and Plasma Imager/the Telescope of Visible Light (UPI/TVIS) onboard the Kaguya spacecraft, *Earth Planets Space*, *61*, xvii-xxiii.

Tu, J., P. Song, B. W. Reinisch, and J. L. Green (2007), Smooth electron density transition from plasmasphere to the sub-auroral region, *J. Geophys. Res.*, *112*, A05227.

Weller, C. S., and R. R. Meier (1974), First satellite observations of the He^+ 304-Å radiation and its interpretation, *J. Geophys. Res.*, *79*, 1,572.

Williams, D. J., E. C. Roelof, and D. G. Mitchell (1992), Global magnetospheric imaging, *Rev. Geophys.*, *30*, 183.

Windt, D. L. (1998), IMD – software for modeling the optical properties of multilayer films, *Comput. Phys.*, *12*, 360-370.

Yamazaki, A., I. Yoshikawa, K. Shiomi, Y. Takizawa, W. Miyake, and M. Nakamura (2006), Latitudinal variation of the solar He I 58.4 nm irradiance from the optical observation of the interplanetary He I emission, *J. Geophys. Res.*, *111*(A6), CiteID A06106.

Yamashita, K., S. Takahashi, D. Kitamoto, S. Takahama, K. Tamura, I. Hatsukade, M. Sakurai, M. Watanabe, A. Yamaguchi, H. Nagata, and M. Ohtani (1992), Characterization of multilayer reflectors and position sensitive detectors in 45-300 Å region, *Rev. Sci. Instrum.*, *63*, 1513-1515.

Yokoyama, T., S. Y. Su, and S. Fukao (2007), Plasma blobs and irregularities concurrently observed by ROCSAT-1 and Equatorial Atmosphere Rader, *J. Geophys. Res.*, *112*, A05311, doi:10.1029/2006JA012044.

Yoshikawa, I., M. Nakamura, M. Hirahara, Y. Takizawa, K. Yamashita, H. Kunieda, T. Yamazaki, K. Misaki, and A. Yamaguchi (1997), Observation of He II emission from the plasmasphere by a newly developed EUV telescope on board sounding rocket S-520-19, *J. Geophys. Res.*, *76*, 19,897.

Yoshikawa, I., A. Yamazaki, K. Shiomi, M. Nakamura, K. Yamashita, and Y. Takizawa (2000a), Evolution of the outer plasmasphere during low geomagnetic activity observed by the EUV scanner onboard Planet-B, *J. Geophys. Res.*, *105*(A12), 27,777.

Yoshikawa, I., A. Yamazaki, K. Shiomi, K. Yamashita, Y. Takizawa, and M. Nakamura (2000b), Photometric measurement of cold helium ions in the magnetotail by an

EUV scanner onboard Planet-B: Evidence of the existence of cold plasmas in the near-Earth plasma sheet, *Geophys. Res. Lett.*, *27*(21), 3657.

Yoshikawa, I., A. Yamazaki, K. Shiomi, K. Yamashita, Y. Takizawa, and M. Nakamura (2001), Interpretation of the He II (304 Å) EUV image of the inner magnetosphere by using empirical models, *J. Geophys. Res.*, *106*(A11), 25,745.

Yoshikawa, I., T. Murachi, H. Takenaka, and S. Ichimaru (2005), Multilayer coating for 30.4 nm, *Rev. Sci. Instrum.*, *76*, Issue 6, 066109.

Yoshikawa, I., A. Yamazaki, G. Murakami, K. Yoshioka, S. Kameda, F. Ezawa, T. Toyota, W. Miyake, M. Taguchi, M. Kikuchi, and M. Nakamura (2008), Telescope of extreme ultraviolet (TEX) onboard SELENE: science from the Moon, *Earth Planets Space*, *60*, 407-416.